Surface-bounded Growth Modeling Applied to Human Mandibles

Per Rønsholt Andresen

Lyngby 1999

IMM-PHD-1999-65

IMM

ISSN 0909-3192

Printed by IMM, Technical University of Denmark

Parts of the work presented in this thesis have previously been published in:

P. R. Andresen, F. L. Bookstein, K. Conradsen, B. K. Ersbøll, J. Marsh, and S. Kreiborg. Surface-bounded Growth Modeling Applied to Human Mandibles. *IEEE Transactions on Medical Imaging*, 1999. Accepted for publication on March 10th, 2000.

P. R. Andresen and M. Nielsen. Non-rigid registration by geometry-constrained diffusion. In *Medical Image Computing and Computer-Assisted Intervention - MICCAI'99*, volume 1679 of *Lecture Notes in Computer Science*, pages 533–543, 1999.

P. R. Andresen, M. Nielsen, and S. Kreiborg. 4D shape-preserving modelling of bone growth. In *Medical Image Computing and Computer-Assisted Intervention - MICCAI'98*, volume 1496 of *Lecture Notes in Computer Science*, pages 710–719, 1998.

M. Nielsen and P. R. Andresen. Feature displacement interpolation. In *IEEE 1998 International Conference on Image Processing (ICIP'98)*, pages 208–212, 1998.

Preface

This thesis has been prepared at the Department of Mathematical Modelling (IMM), Technical University of Denmark and 3D-Lab, School of Dentistry, University of Copenhagen. It is a partial fulfillment of the requirements for the degree of Ph.D. in engineering.

The subject of the present thesis is surface-bounded growth simulation/modeling applied to human mandibles. The use of shape features and morphometrics are combined in order to preserve the characteristics of the mandible when modeled.

It is assumed that the reader is familiar with the field of medical image analysis.

Lyngby, July 31st, 1999

Per Rønsholt Andresen

Acknowledgments

My thanks go to the faculty and students of the Section for Image Analysis and 3D-Lab for their help and companionship during the last three years. Especially MSc.Eng Per Larsen and Cand.Scient Tron Darvann deserves a lot of credit. Tron Darvann took care of the transportation/transmission of the CT scans made available by M.D. Jeffrey L. Marsh. Thanks, Tron!

A lot of people helped me through newsgroups and mailing-lists. Thanks a lot!

Thanks to Librarian Finn Kuno Christensen for his enormous help.

Thanks to *Kitware* (www.kitware.com) for making The Visualization Toolkit (VTK) public. It is a great visualization tool.

I also want to thank Dr. Gérard Subsol and Dr. Jean-Philippe Thirion for helping me understand the computation of the extremal mesh.

Thanks to Dr. Andy B. Dobrzeniecki for valuable comments to my manuscripts.

Also thanks to Dr. Bjarne K. Ersbøll for his interest and comments on the project.

I owe enormous gratitude to Dr. Mads Nielsen for his undying enthusiasm about the topic.

I am also indebted to M.D. Jeffrey L. Marsh for the longitudinal CT datasets. He generously put the data to my disposal. Without these data, many of the results would have been speculations.

I am also indebted to Dr. Fred L. Bookstein who shared his ideas on morphometrics with me.

I owe enormous gratitude to my academic advisors Dr. Sven Kreiborg and M.S. Knut Conradsen who played a crucial role making this project possible.

Finally, I express my heartfelt thanks to my family especially Dorthe for consistent support and encouragement.

This thesis is supported by the Danish Technical Research Council grant number 9600452.

For typesetting the LaTeX 2_ε package has been used.

Summary

This thesis presents mathematical and computational techniques for three dimensional growth modeling applied to human mandibles. The longitudinal shape changes make the mandible a complex bone. The teeth erupt and the condylar processes change direction, from pointing predominantly backward to pointing more upward. The full dataset consists of 31 mandibles from six patients. Each patient is longitudinally CT scanned between three and seven times. Age range is 1 month to 12 years old for the scans.

Growth modeling consists of three overall steps: 1) extraction of features. 2) registration of the common features. 3) model the process that moves the matched points (growth modeling).

A local shape feature called *crest line* has shown itself to be structurally stable on mandibles. Registration of crest lines (from different mandibles) results in a sparse deformation field, which must be interpolated to yield a spatially dense field. Different methods for constructing the sparse field are compared. *Adaptive Gaussian smoothing* is the preferred method since it is parameter free and yields good results in practice.

A new method, *geometry-constrained diffusion*, is used to simplify the deformation field. It is shown how the method significantly improves the growth model.

The most successful growth model is linear and based on results from *shape analysis* and *principal component analysis*. The growth model is tested in a cross validation study with good results.

The worst case mean modeling error in the cross validation study is 3.7 mm. It occurs when modeling the shape and size of a 12 years old mandible based on the 3 month old scan. When using successively more recent scans as basis for the model the error drops to 2.0 mm for the 11 years old scan. Thus, it seems reasonable to assume that the mandibular growth is linear.

Keywords: adaptive Gaussian smoothing, aperture-problem, automatic landmark detection, crest lines, CT scans, extremal mesh, geometry-constrained diffusion, homologous points, linear growth modeling, mandible, morphometrics, non-rigid shape-preserving registration, principal component analysis, semi-landmarks, shape analysis, simplest deformation field

Resumé

Denne afhandling anvender matematiske og datamatiske teknikker til tre-dimensional vækstmodellering af underkæber fra mennesker. Den tidsmæssige formændring af kæben, gør den til en kompleks knogle. Tænderne bryder frem og processus condylaris ændrer retning fra at pege overvejende bagud til at pege mere opad. Det fulde datasæt består af 31 underkæber fra seks patienter. Hver patient er CT-skannet over tid mellem tre og syv gange. Kæberne er mellem 1 måned og 12 år gamle.

Vækstmodellering består af 3 overordnede skridt: 1) bestemmelse af *features*; 2) registrering af fælles features 3) modellering af processen, der flytter de sammenhørende features (vækstmodellering).

En lokal form feature, som kaldes *crest line*, har vist sig at være strukturel stabil på kæberne. Registrering af crest lines (fra forskellige kæber) resulterer i et sparsomt deformationsfelt, som skal interpoleres for at skabe et kompakt felt. Forskellige metoder til at konstruere et kompakt felt er sammenlignet. *Adaptiv gaussisk glatning* er den foretrukne, da den er parameterfri og giver gode resultater i praksis.

En ny metode, *geometry-constrained diffusion*, benyttes til at simplificere deformationsfeltet. Det vises, at vækstmodellen herved forbedres signifikant.

Den mest succesfulde vækstmodel er lineær og baseret på resultater fra *formanalyse* og *principal*

komponent analyse. Vækstmodellen er blevet testet med gode resultater i et krydsvalideringsforsøg. *Worst case* middel-modelleringsfejlen i krydsvalideringsforsøget er 3,7 mm. Fejlen optræder, når formen og størrelsen af en 12 årig underkæbe modelleres, baseret på en skanning fra 3 måneders alderen. Ved successivt at anvendte skanninger af nyere dato som basis for modellen, falder fejlen til 2,0 mm for 11-års skanningen. Det synes derfor rimeligt at antage, at underkæben vokser lineært.

Nøgleord: Adaptiv Gaussisk glatning, apertur problem, automatisk landmark detektion, crest linier, CT skanning, elastisk form-bevarende registrering, extremal mesh, form analyse, geometrisk begrænset diffusion, homologe punkter, lineær vækstmodellering, morfometri, principale komponenter, semi-landmarks, simpelst deformationsfelt, underkæbe

Contents

List of Figures

List of Tables

Chapter 1

Introduction

This thesis describes results obtained through a three-year Ph.D. project starting August, 1996 and published in four papers [ABC$^+$99, AN99, ANK98, NA98]. The main purpose of the project was to develop a computerized three dimensional (3D) growth model describing the craniofacial growth of humans.

Especially, when performing pediatric craniofacial surgery a 3D growth model is useful. The model would also be useful for basic understanding and teaching.

Earlier longitudinal growth studies on man have only been based on 2D images (cephalograms) except for [Sub95] and [BNGK97] (See Section 7.2 on page 86 for a short review). Both studies are based on patient 6 (cf. Table 7.1 on page 90). Even though two dimensional images can be combined, 3D spatial interpretation is very hard to achieve.

Recently, there has been an explosive development in the area of medical imaging enabling us to study the anatomy *in vivo* with very high precision using digital imaging modalities such as Magnetic Resonance (MR) and Computed Tomography (CT).

Since, the beginning of the 1980's CT scannings of children with Apert syndrome have been performed at St. Louis Children's Hospital, USA (Dr. Jeffrey L. Marsh) and in the late 1980's at The University Hospital of Copenhagen, Denmark.

The six Apert patients used in the present thesis were scanned between three and seven times, age range between 1 month and 12 years old (Table 7.1 on page 90). All scannings were performed for diagnostic and treatment planning purposes. The full dataset was used in Chapters 6 & 7. A single patient (patient 6 - Table 7.1 on page 90) was used in Chapters 4 & 5. The reason being that the scannings from St. Louis Children's Hospital (patients 1-5 (Table 7.1 on page 90)) first became available for this study in July, 1998.

The study has been limited to the mandible for three reasons: 1) the development of the mandible is unaffected by the primary anomaly [KAC99]. Thus, it is assumed that the mandibular growth in the six subjects in the present study closely resembles normal mandibular development. 2) the longitudinal shape change makes the mandible a complex bone. The teeth erupt and the condylar process changes direction, from predominantly pointing backward to pointing more upward (Figure 5.6 on page 56). It is therefore a challenging bone to model. 3) non of the mandibles underwent surgery in the observation period. A paper by Dean et al. [DHBS99] indicates that the growth model presented in Chapter 7 should generalize to the rest of the craniofacial region, thereby making the results of this project applicable to the rest of the craniofacial region.

Making a growth model consist of the three general steps:

1. extraction of features.
2. registration of the common features.
3. model the process that moves the matched points (growth modeling).

When making a "pure" registration (e.g. superimposing two volumes), the process in between the acquisitions is irrelevant. Only the starting and ending "points" are relevant. This is opposite to growth modeling where the path between the "points" *is* the growth. Further, the "points" also have to correspond across the cases i.e. be semi-landmarks (see page 86 for a definition of landmarks and semi-landmarks). Thus, the two first steps above must provide the semi-landmarks and the third makes the temporal interpolation/extraction of them.

Looking at the temporal change on the mandible, it is seen that the topology does not change a lot. For automatic registration we search for features reflecting the fixed topology of the mandible. *Crest lines* seem to be a good choice. Crest lines are lines where the surface bend most (Chapter 3).

The use of crest lines have been very much inspired by Subsol et al. [STA95] (also published in an international journal [STA98]).

Chapter 5 presents our first attempt to make a growth model following the three steps above. On the mandible it is not enough to use the crest lines, therefore lines maximally in k_2 (here called k_2-max lines) in the extremal mesh (Chapter 3) are included. Besides the inclusion of the k_2-max lines, the extraction and registration of the lines closely follow the ideas of [STA98].

Crest lines and k_2-max lines only define a sparse deformation field. A dense field is needed in order to deform the surface of the mandible. The dense field is obtained by interpolating the sparse field as described in Chapter 4. In that chapter different methods are investigated, like Gaussian interpolation with renormalization, thin-plate splines, kriging and adaptive Gaussian smoothing. Even though adaptive Gaussian smoothing does not satisfy all the desired properties for the interpolation schemes (Chapter 4), it is the preferred interpolation method. Mainly since it yields very good results in practice and it is parameter free.

Having the dense deformation field that links points on the mandible together, a second order polynomial is used to model the growth (Chapter 5). The coefficients of the polynomial depend on the placement of the mandibles in space. Therefore, the mandibles are initially registered with respect to biological "fix points" like the nerve canal (Section 5.6). Choices of initial registration will be discussed shortly. The deformation field contained folds, which are seen on Figure 6.4 on page 77. The folds arise from an imperfect registration e.g. wrong pairings of lines,- especially the k_2-max lines. See Figure 3.3 on page 24 for k_2-max lines on the mandible. Chapter 5 solves this by deforming volumes instead of surfaces. Generating an iso-surface from a deformed volume always result in a surface without folds due to the definition of the iso-surface. The only demand is that links inside (outside) the source object also link to the inside (outside) of the target object, which is satisfied when using the adaptive Gaussian smoothing.

When having folds in the deformation field, we do not have semi-landmarks. It is assumed that homologous points do not "change" place i.e. the ordering of the anatomical structures are preserved. It also seems reasonable to assume, that the deformation not tear apart the object: it should be a homeomorphism (at least). Chapter 6 presents a new iterative algorithm, *geometric-constrained diffusion*, that removes the folds. Table 7.2 on page 101 shows that the algorithm significantly improves the growth model.

Discussion with Dr. Fred L. Bookstein and the article by Dean et al. [DHBS99] (I received a draft thanks to Dr. Fred L. Bookstein) inspired me to use the same methods as in [DHBS99] (see page 88 for a short review), which are presented in Chapter 7. Chapter 7 describes how *shape analysis* and *principal component analysis* are used to make a linear growth model based on the full dataset, which precisely model the longitudinal shape change of the mandible.

Shape analysis uses a *metric* that actually make up a Riemannian manifold, called the *Kendall Shape manifold* with Procrustes distance[1] as metric [Boo97].

[1] Procrustes distance between the shapes is the minimal sum of squares of the residual distances between landmarks [Boo97].

The use of Kendall Shape manifold as "registration" instead of the biological registration discussed above is no more right or wrong,- but certainly improves the growth model. This is also topic for discussion in the next chapter.

To summarize:

- Chapter 2 collects the results obtained throughout the project.
- Chapter 3 defines the extremal mesh and the subset called crest lines.
- Chapter 4 compares different interpolation methods used to make a dense deformations field from a sparse one.
- Chapter 5 presents our first attempt to make a growth model.

The next two chapters improve the registration and the growth model, respectively.

- Chapter 6 presents a new iterative algorithm, geometric-constrained diffusion, which simplifies a deformation field.
- Chapter 7 uses shape analysis and principal component analysis to make a linear growth model that predicts the shape and size changes of the mandible with high precision.

1.1 Comments on the last four chapters

The Chapters 4-7 are published papers. They have only been changed from its originals for typographic layout. Spelling errors and other typos have been removed (as much as possible). The bibliographies have been updated and the entries are changed to make cross referencing easier

Chapter 4. The Paper [NA98] was accepted as a poster at the *IEEE Signal Processing Society 1998 International Conference on Image Processing* (ICIP'98) held in Chicago, Illinois, USA. The review process is unknown.

Chapter 5. The article [ANK98] was accepted as a poster at the *First International Conference on Medical Image Computing and Computer-Assisted Intervention* (MICCAI'98) held in Massachusetts Institute of Technology, Cambridge MA, USA. There were four reviewers on the paper. 243 papers were received, 48 was selected as oral presentations and 85 as posters.

Chapter 6. The article [AN99] is accepted for oral presentation at the *Second International Conference on Medical Image Computing and Computer-Assisted Intervention* (MICCAI'99) to be hold in Cambridge, England (September, 1999). There were three reviewers on the paper. 212 submissions was received of which 49 have been accepted for oral presentations and 84 as posters.

Chapter 7. The manuscript [ABC+99] was submitted to *IEEE Transactions on Medical Imaging* July, 1999 and accepted for publication on March 10th, 2000.

Bibliography

[ABC$^+$99] P. R. Andresen, F. L. Bookstein, K. Conradsen, B. K. Ersbøll, J. Marsh, and S. Kreiborg. Surface-bounded growth modeling applied to human mandibles. *IEEE Transactions on Medical Imaging*, 1999. Accepted for publication on March 10th, 2000.

[AN99] P. R. Andresen and M. Nielsen. Non-rigid registration by geometry-constrained diffusion. In *Medical Image Computing and Computer-Assisted Intervention - MICCAI'99*, volume 1679 of *Lecture Notes in Computer Science*, pages 533–543, 1999.

[ANK98] P. R. Andresen, M. Nielsen, and S. Kreiborg. 4D shape-preserving modelling of bone growth. In *Medical Image Computing and Computer-Assisted Intervention - MICCAI'98*, volume 1496 of *Lecture Notes in Computer Science*, pages 710–719, 1998.

[Boo97] F. L. Bookstein. Shape and the information in medical images: a decade of the morphometric synthesis. *Computer Vision and Image Understanding*, 66(2):97–118, 1997.

[BNGK97] M. Bro-Nielsen, C. Gramkow, and S. Kreiborg. Non-rigid image registration using bone growth model. In *CVRMed-MRCAS'97*, Lecture Notes in Computer Science, pages 3–12. Springer, 1997.

[DHBS99] D. Dean, M. G. Hans, F. L. Bookstein, and K. Subramanyan. Three dimensional Bolton-Brush growth study landmark data: Ontogeny and sexual dimorphism of the bolton standards cohort. *Cleft Palate - Craniofacial Journal*, 1999. in press.

[KAC99] S. Kreiborg, H. Aduss, and M. M. Cohen Jr. Cephalometric study of the Apert syndrome in adolescence and adulthood. *Journal of Craniofacial Genetics Developmental Biology*, 19:1–11, 1999.

[NA98] M. Nielsen and P. R. Andresen. Feature displacement interpolation. In *IEEE 1998 International Conference on Image Processing (ICIP'98)*, pages 208–212, 1998.

[Sub95] G. Subsol. *Construction automatique d'atlas anatomiques morphométriques à partir d'images médicales tridimensionnelles*. PhD thesis, École Centrale Paris, 1995.

[STA95] G. Subsol, J.-P. Thirion, and N. Ayache. A general scheme for automatically building 3D morphometric anatomical atlases: Application to a skull atlas. Technical Report 2586, INRIA, France, 1995.

[STA98] G. Subsol, J.-P. Thirion, and N. Ayache. A general scheme for automatically building 3D morphometric anatomical atlases: Application to a skull atlas. *Medical Image Analysis*, 2(1):37–60, 1998.

Chapter 2

Conclusion

Growth is a very interesting and fascinating area in its own. Characterization of the growth process has many important practical application. This thesis contains a contribution to this attempt.

The remaining of this chapter consists of one main conclusion and five sub-conclusions.

The main conclusion is that

- we have constructed a growth model which accurately models the temporal shape and size changes of the mandible using a linear growth model, a mandibular surface of the patient to be modeled and a future size of the modeled mandible.

Based on the main conclusion and the methods used, we have the following sub-conclusions.

- It is surprising that the growth of the mandible is modeled very well with a *linear* growth model. Previous studies assume/show the growth to be non-linear [BS83]. These two statements (linear versus non-linear) do not have to be contradictions. Based on a biological coordinate system (e.g. using metal implants in the mandible as basis for the coordinate system) it is very plausible that the growth is non-linear [BS83]. Hopefully, we will see a combination of the two frames in the future. The linear system used for growth prediction, and the biological space used to make inference concerning the growth process.

- It is remarkable that two different growth processes, the growth of the mandible itself and tooth eruption, are both well modeled using the same linear growth model.

- *Geometric-constrained diffusion* is a new method which simplifies a 3D deformation field based on a simple iterative scheme. A deformation field often contains folds or other structures making it a "non-homeomorphic" mapping. It is our belief (we have not been able to prove it), that the method changes the deformation field towards a homeomorphism/diffeomorphism. Geometric-constrained diffusion significantly improves the growth model.

- Crest lines have shown themselves to be very good shape features on the mandible, although some topology changes do occur. Generally, two crest lines are found on top of the teeth for a young patient. Later, there is only one crest line. Similar changes occur at other places on the mandible.

- Different methods for interpolating sparse deformation fields have been investigated. *Adaptive Gaussian smoothing* is the preferred method as it is parameter free and yields good results in practice.

At present, we can only obtain the closely spaced CT scans that allow this kind of analysis from clinical cases with various types of craniofacial growth disturbances. It will be interesting when longitudinal scans become common for larger populations.

Bibliography

[BS83] A. Björk and V. Skieller. Normal and abnormal growth of the mandible. A synthesis of longitudinal cephalometric implant studies over a period of 25 years. *European Journal of Orthodontics*, 5:1–46, 1983.

Chapter 3

The Extremal Mesh and Crest Lines

The following sections explain the definition and extraction of the extremal mesh, and, crest lines which is a subset of the extremal mesh.

A short summary of the main results from two research reports [TG93, Thi93] (the later is also published in [Thi96]) is given below. No new results are presented. Appendix 3.7 is a minor extension, deriving the expression for the curvature of a curve.

3.1 Introduction

Extremal lines are lines where one of the two principal surface curvatures is locally extremal. Extremal points are points where the two principal surface curvatures are both extremal. The *extremal mesh* is the graph of the surface whose vertices are the extremal points and whose edges are the extremal lines. It is invariant with respect to rigid transformations. Good topological properties of the graph are ensured with a local geometric invariant of 2D surfaces called the Gaussian extremality, which allows one to overcome orientation problems encountered with the "direct" definition of the extremal lines and points.

Mathematically the calculation is simple: first, a surface patch is locally fitted to the data, with a known parameterization in a local coordinate system (u, v), and then rely on the traditional results from differential geometry. The major problem of those methods is how to fit (or deform) the surface patch in a reliable way, which is independent from the topology of the surface.

It has been shown that it is possible to compute locally the principal curvature and principal direction, without fitting a surface patch [MBF92]. The major difference between [MBF92] and the present is, that we do not consider a parametric representation of the surface, but its *implicit* definition. The final formula only use the differentials of the image function $f(x, y, z)$ in the three axes, and are symmetric with respect to those axes.

First we need some definitions.

3.2 Definitions

For any continuous function $f(x, y, z)$ in $\mathcal{R}^3$, any value I of $\mathcal{R}$ (called the *iso-value*), f defines a continuous, not self intersecting surface, without hole, which is called the *iso-intensity surface* of f, or simply *iso-surface* by the separation of the regions $f \geq I$ and $f < I$ (or the regions $f > I$ and $f \leq I$). The surface cannot simply be defined by the implicit equation $f(x, y, z) = I$, as some regions of $\mathcal{R}^3$ may have a constant intensity I. In that case, $f = I$ does not define a surface but a volume.

Let us now see some properties of the two times differentiable surfaces (Figure 3.1). At each point P of those surfaces, there is an infinite number of curvatures, but for each direction $\vec{t}$ in the tangent plane at P, there is only on associated curvature $k_{\vec{t}}$. There are two privileged directions of the surface, called the *principal directions* ($\vec{t}_1$ and $\vec{t}_2$), which correspond to the two extremal values of the curvature: k_1 and k_2 (except for the umbilic points where the curvature is constant for all

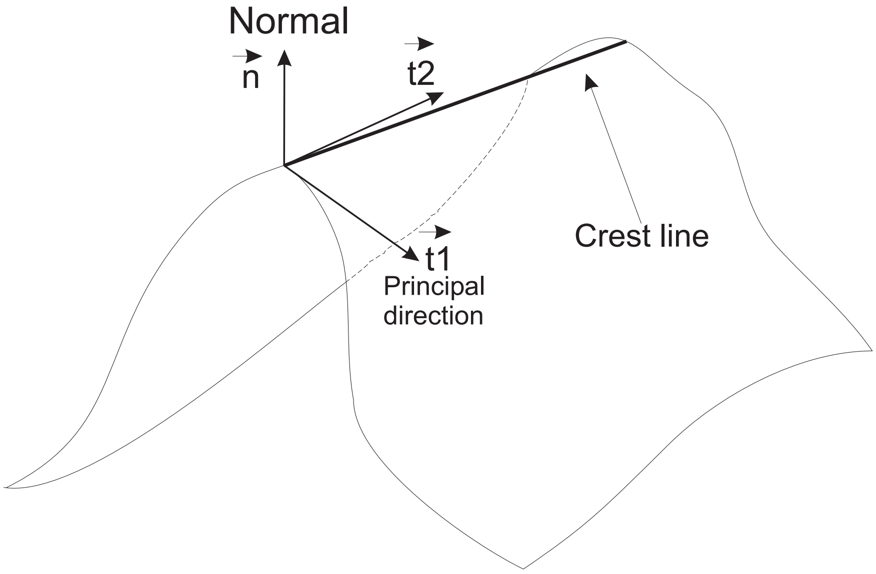

Figure 3.1: *Differential characteristics of surfaces.*

directions). One of these two principal curvatures is maximal in absolute value (let say k_1), and is called the *maximal curvature.*

The product of the two principal curvatures is called the *Gaussian curvature* K, and the half sum is called the *average curvature* S. To those values we can add the *extremality criterion* e which is the directional derivative of the maximal curvature (here k_1), in the corresponding principal direction ($\vec{t_1}$). In fact, the same extremality criterion can also be defined for the other principal direction, and we have therefore two "extremalities" e_1 and e_2. The successive loci of the zero-crossing of the *Gaussian extremality* $E_g = e_1 e_2$ defines the *extremal mesh.*

There are some orientational problems, which comes from the fact that $\vec{t_1}$ and $\vec{t_2}$ are not defined as vectors, but as directions. I will refer to [Thi93, TG93] for a solution.

We will use the following notations for the partial derivatives: f_x for $\partial f(u, \phi(u))/\partial x$, f_{xy} for $\partial^2 f(u, \phi(u))/\partial x \partial y$ etc., and ϕ' for $d\phi/du$. $\vec{\nabla}$ is the gradient operator.

3.3 Curvature and corner points in 2D images

I this section, we present the description of the method in the 2D case, which will help to understand the computations of the next section.

For a 2D function $f(x, y)$ of $\mathcal{R}^2$, we call *iso-boundary* (or *iso-contour*) the restriction of the iso-surface to 2D. The iso-boundary is the lines which separate the regions $f \geq I$ from the regions $f < I$. We show now how to compute the curvature of this iso-contour, and how to derive a 2D extremality criterion e whose zero-crossings are the points of maximal curvature along the iso-boundary.

It is assumed that $f(x, y)$ is the continuous function. This is obtained by convolving the image with the Gaussian function. f is then continuous and infinitely differentiable. The iso-contour defined with the iso-value I is also infinitely differentiable, and its equation is $f(x, y) = I$, if $\|\vec{\nabla} f\| \neq 0$. This equation is the implicit equation of a curve in the plane. Using the implicit functions theorem, there exits locally a function ϕ such that $(x = u, y = \phi(u))$ and $f(u, \phi(u)) = I$. The derivatives of ϕ satisfies

$$\phi' = -f_x/f_y \tag{3.1}$$

since

$$f(u, \phi(u)) = I$$

$$\Downarrow$$

$$\frac{d}{du} f(u, \phi(u)) = \frac{d}{du} I$$

$$\Downarrow$$

$$f_x + f_y \phi_u = 0 \tag{3.2}$$

$$\Downarrow$$

$$\phi' = \phi_u = -f_x/f_y \tag{3.3}$$

Differentiation of Equation 3.2 by u gives:

$$\phi'' = \frac{2f_x f_y f_{xy} - f_x^2 f_{yy} - f_y^2 f_{xx}}{f_y^3} \tag{3.4}$$

The curvature c of the curve is given by $c(u) = \phi''(u)/(1+\phi'^2(u))^{3/2})$ (Appendix 3.7), thus:

$$c(x,y) = \frac{2f_x f_y f_{xy} - f_x^2 f_{yy} - f_y^2 f_{xx}}{(f_x^2 + f_y^2)^{3/2}} \tag{3.5}$$

Equation 3.5 gives the curvature at any point on the image, and which depends only on the differentials of the image up to order 2.

The points of maximum curvature along the iso-contour are now calculated. Those points satisfy the equation $dc(u)/du = 0$. A strictly equivalent equation is to state that the derivative of the curvature in the direction of the tangent is zero, that is $\vec{\nabla} c(x,y) \cdot \vec{t} = 0$, where $\vec{t}$ is the tangent $(-f_y, f_x)$ to the iso-contour, and $\vec{\nabla} c(x,y)$ is the gradient of c with respect to x and y: (c_x, c_y). With this notation $\vec{\nabla} c(x,y) \cdot \vec{t}$ equals

$$c_x f_y - c_y f_x = 0 \tag{3.6}$$

This equation is of the form $e(x,y) = 0$, and defines a new implicit curve in the 2D image, whose intersections with the iso-contour $f(x,y) = I$ are the points of maximal or minimal curvatures. The curve $e(x,y) = 0$ is called *the maximal (respective minimal) curvature curve.*

It is remarkable, that the maximum curvature curve does not depend on the choice of any iso-value threshold I, but is intrinsically defined with the values of the image $f(x,y)$. Of course, the extremality is only really significant in the neighborhood of a "true" contour, that is, when the gradient norm is high.

3.4 Differential characteristics of iso-surfaces

As seen in the last section, the determination of the corner points was reduced to the computation of the intersection of two planar curves $f(x,y) = I$ and $e(x,y) = 0$. In the 3D-case, it is shown that the computation of the extremal mesh on an iso-surface is reduced to the intersection of two iso-surfaces. One being the the well-known iso-surface $f(x,y,z) = I$, and the other one being the zero-crossing of the Gaussian extremality function $E_g(x,y,z) = 0$.

As for the 2D case, the implicit functions theorem is used in order to transform the implicit equation of the iso-surface $f(x,y,z) = I$ into the parametric equation of the surface: $(x = u, y = v, z = \phi(u,v))$. Then the first and second Fundamental Forms of differential geometry [Lip69] are used to compute the principal curvatures and directions. These formulae are generally written for the parametric formulation. In the present chapter, the idea is to find equivalent results with the implicit equation of the surface. The principal curvatures and principal directions correspond respectively to the eigenvalues and eigenvectors of the matrix, called the Weingarten endomorphism:

$$\begin{pmatrix} E & F \\ F & G \end{pmatrix}^{-1} \begin{pmatrix} L & M \\ M & N \end{pmatrix} = \begin{pmatrix} \frac{GL-FM}{H} & \frac{GM-FN}{H} \\ \frac{EM-FL}{H} & \frac{EN-FM}{H} \end{pmatrix} = \begin{pmatrix} a & b \\ c & d \end{pmatrix} \tag{3.7}$$

Let S be the parametric surface defined as $S(u,v) = (u, v, \phi(u,v))$. For a point $S(u,v)$ on the surface, we have

$$E = \|\vec{S}_u\|^2 \quad F = \vec{S}_u \cdot \vec{S}_v \quad G = \|\vec{S}_v\|^2 \tag{3.8}$$

$$L = \frac{\vec{S}_{uu} \cdot \vec{n}}{H^{1/2}} \;\; M = \frac{\vec{S}_{uv} \cdot \vec{n}}{H^{1/2}} \;\; N = \frac{\vec{S}_{vv} \cdot \vec{n}}{H^{1/2}} \;\; H = EG - F^2 \tag{3.9}$$

Here $\vec{n}(u,v)$ is defined as $\vec{S}_u \times \vec{S}_v$, and is a vector lying normal to the surface at $\vec{S}(u,v)$. Using the implicit functions theorem, and substitution of the derivatives of f for the derivatives of $\vec{S}$, as in the 2D case:

$$\begin{array}{lll} E = \frac{f_x^2+f_z^2}{f_z^2} & L = -\frac{f_z(-2f_x f_{xz}+f_{xx}f_z)+f_x^2 f_{zz}}{f_z^3} & \\ F = \frac{f_x f_y}{f_z^2} & M = \frac{f_z(f_{xz}f_y+f_x f_{yz}-f_{xy}f_z)-f_x f_y f_{zz}}{f_z^3} & H = \frac{f_x^2+f_y^2+f_z^2}{f_z^2} \\ G = \frac{f_y^2+f_z^2}{f_z^2} & N = -\frac{f_z(-2f_y f_{yz}+f_{yy}f_z)+f_y^2 f_{zz}}{f_z^3} & \end{array} \tag{3.10}$$

The formulae are not symmetric with respect to the three axes $\vec{x}, \vec{y}$ and $\vec{z}$, as $\vec{z}$ is given a special role, when using the implicit functions theorem.

We now seek for symmetric equations for the curvatures and principal directions.

$\vec{k_1}, \vec{k_2}$ are the two principal curvatures, and $\vec{t_1}, \vec{t_2}$ are the associated principal directions. $K = k_1 k_2$ is the Gaussian curvature, and $S = (k_1 + k_2)/2$ is the average curvature of the iso-surface. K and S are also respectively the determinant and half the trace of the matrix given in Equation 3.7, that is:

$$K = (LN - M^2)/H \quad \text{and} \quad 2S = (EN - 2FM + GL)/H \tag{3.11}$$

Using Equation 3.10:

$$\begin{aligned} K = \frac{1}{(f_x^2+f_y^2+f_z^2)^2} & [\\ & -\left(f_{xz}^2 f_y^2\right) - f_x^2 f_{yz}^2 + 2 f_{xy} f_{xz} f_y f_z \\ & -2 f_x f_{xz} f_{yy} f_z - f_{xy}^2 f_z^2 + f_{xx} f_{yy} f_z^2 \\ & +2 f_{yz}\left(f_x f_{xy} f_z + f_y\left(f_x f_{xz} - f_{xx} f_z\right)\right) \\ & +\left(-2 f_x f_{xy} f_y + f_{xx} f_y^2 + f_x^2 f_{yy}\right) f_{zz} \,] \end{aligned} \tag{3.12}$$

$$\begin{aligned} S = \frac{-1}{2(f_x^2+f_y^2+f_z^2)^{3/2}} & [\\ & -2 f_x f_{xy} f_y + f_{xx} f_y^2 + f_x^2 f_{yy} \\ & -2\left(f_x f_{xz} + f_y f_{yz}\right) f_z \\ & +\left(f_{xx} + f_{yy}\right) f_z^2 + \left(f_x^2 + f_y^2\right) f_{zz} \,] \end{aligned} \tag{3.13}$$

Once having K and S, k_1 and k_2 are the solutions of a second order equation ($i \in \{1,2\}$):

$$k_i = S \pm \sqrt{\Delta} \quad \text{with} \quad \Delta = S^2 - K \tag{3.14}$$

The computation of the principal directions is a bit more complicated. Using the notations of Equation 3.7, the principal directions $\vec{t_i}$, which are the two eigenvectors of the matrix in Equation 3.7, may be represented in the basis $\vec{S_u}, \vec{S_v}$ in the form $u_i\vec{S_u} + v_i\vec{S_v}$, and satisfy the equations

$$\begin{array}{cccc} (a-k_i)u_i & + & bv_i & = & 0 \\ cu_i & + & (d-k_i)v_i & = & 0 \end{array} \tag{3.15}$$

For each $i \in \{1,2\}$ the two equations are dependent, and thus the solution set for (u_i, v_i) will lie along a line colinear with $\vec{t_i}$. $\vec{t_i}$ can be computed by either of the two equations in Equation 3.15, which gives us two vectors $\vec{t_{i1}}$ and $\vec{t_{i2}}$ colinear to $\vec{t_i}$.

Since $\vec{S_u} = (1, 0, -f_x/f_z)$ and $\vec{S_v} = (0, 1, -f_y/f_z)$ (remember that $S(u,v) = (u, v, \phi(u,v))$ and $\phi_u = -f_x/f_z$, $\phi_v = -f_y/f_z$) one solution is:

$$\begin{array}{l} \vec{t_{i1}} = u_i\vec{S_u} + v_i\vec{S_v} \\ \Big\Downarrow \quad (a-k_i)u_i + bv_i = 0 \;\Rightarrow \\ \Big\Downarrow \quad u_i = b \wedge v_i = k_i - a \\ \vec{t_{i1}} = b\vec{S_u} + (k_i - a)\vec{S_v} \\ \\ \Downarrow \text{The vectors } \vec{S_u} \text{ and } \vec{S_v} \text{ are multiplied with } f_z \\ \vec{t_{i1}} = \begin{pmatrix} f_z b \\ f_z(k_i - a) \\ -f_x b - f_y(k_i - a) \end{pmatrix} \end{array} \tag{3.16}$$

and

$$\begin{aligned}
&\vec{t}_{i2} = u_i\vec{S}_u + v_i\vec{S}_v \\
&\Big\Downarrow \quad cu_i + (d - k_i)v_i = 0 \quad \Rightarrow \\
&\quad\;\; u_i = k_i - d \;\wedge\; v_i = c \\
&\vec{t}_{i2} = (k_i - d)\vec{S}_u + c\vec{S}_v
\end{aligned}$$

$\Downarrow$ The vectors $\vec{S}_u$ and $\vec{S}_v$ are multiplied with f_z

$$\vec{t}_{i2} = \begin{pmatrix} f_z(k_i - d) \\ f_z c \\ -f_x(k_i - d) - f_y c \end{pmatrix} \tag{3.17}$$

Some simplifications are possible, as:

$$(k_i - a) = \frac{EN - GL}{2H} \pm \sqrt{\Delta} \quad , \quad (k_i - d) = \frac{GL - EN}{2H} \pm \sqrt{\Delta} \tag{3.18}$$

We seek for symmetric equations in x, y, z. Thirion and Gourdon ([TG93]) found a solution, which uses a given linear combination of $\vec{t}_{i1}$ and $\vec{t}_{i2}$. Making the substitutions for E, N, G, L, and then using the linear combination $\vec{t}_i = \frac{f_x - f_z}{f_z}\vec{t}_{i1} + \frac{f_z - f_y}{f_z}\vec{t}_{i2}$ restores the symmetry between the three coordinates. We obtain

$$\vec{t}_i = \vec{\alpha} \pm \sqrt{\Delta}\vec{\beta} \quad \text{with} \quad \vec{\beta} = (f_z - f_y, f_x - f_z, f_y - f_x) \tag{3.19}$$

$\vec{\alpha}$ is complicated. Like $\vec{\beta}$, it is symmetric with respect to the three coordinates. Equation 3.20 gives the x-component of $\vec{\alpha}$. The y and z components are obtained by circular permutations of x, y and z. Despite the symmetry between the three axis, there is still a privileged direction, which is $\vec{\omega} = (1, 1, 1)$, because, if $\vec{\nabla} f$ is colinear to $\vec{\omega}$, then $\vec{\alpha} = \vec{\beta} = 0$, which means that we fails to find $\vec{t}_1, \vec{t}_2$. There are locations where the principal directions are not obtained be means of the symmetric formula:

- Umbilic points ($\Delta = 0$)
- The gradient vanishes ($\vec{\nabla} f = 0$)
- and rather unexpected a privileged direction when $\vec{\nabla} f$ and $\vec{\omega}$ are colinear ($\vec{\nabla} f \times \vec{\omega} = 0$)

$$\begin{aligned}
\vec{\alpha} \cdot \vec{x} = & \frac{1}{2(f_x^2 + f_y^2 + f_z^2)^{3/2}} [\\
& -2 f_x f_{xy} f_y^2 + 2 f_x f_{xz} f_y^2 + f_{xx} f_y^3 - 2 f_{xz} f_y^3 + f_x^2 f_y f_{yy} \\
& -2 f_x^2 f_y f_{yz} + 2 f_x f_y^2 f_{yz} - f_{xx} f_y^2 f_z + 2 f_{xy} f_y^2 f_z + f_x^2 f_{yy} f_z \\
& -2 f_x f_y f_{yy} f_z + 2 f_x^2 f_{yz} f_z + 2 f_y^2 f_{yz} f_z - 2 f_x f_{xy} f_z^2 + 2 f_x f_{xz} f_z^2 \\
& + f_{xx} f_y f_z^2 - 2 f_{xz} f_y f_z^2 - f_y f_{yy} f_z^2 - 2 f_x f_{yz} f_z^2 - 2 f_y f_{yz} f_z^2 \\
& - f_{xx} f_z^3 + 2 f_{xy} f_z^3 + f_{yy} f_z^3 - f_x^2 f_y f_{zz} - f_y^3 f_{zz} - f_x^2 f_z f_{zz} \\
& + 2 f_x f_y f_z f_{zz} + f_y^2 f_z f_{zz}]
\end{aligned} \tag{3.20}$$

3.5 Gaussian extremality

The Gaussian extremality (which defines a surface) is defined as:

$$E_g = e_1 e_2 = 0 \tag{3.21}$$

where

$$e_i = \vec{\nabla} k_i \cdot \vec{t_i}\,,\ i \in \{1, 2\} \tag{3.22}$$

The extremal mesh is the intersection of the Gaussian extremality and the iso-surface. Extremal points are the simultaneous zero crossings of the two extremalities, $e_1 = 0$ and $e_2 = 0$. For extremal lines either $e_1 = 0$ or $e_2 = 0$, not both.

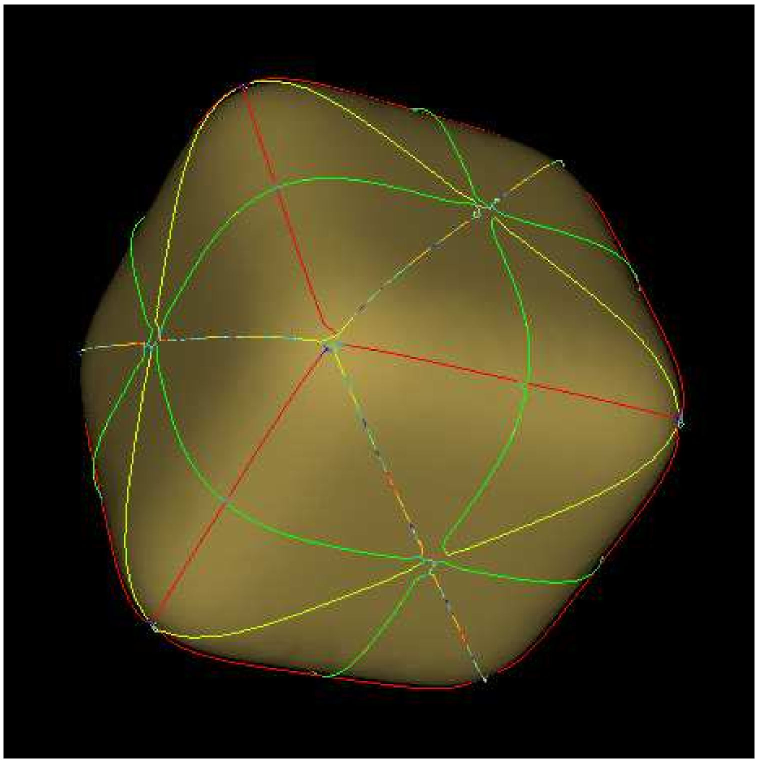

Figure 3.2: *The extremal mesh on a rounded cube. The crest lines, maximal second curvature, and minimal second curvature are red, yellow, and green, respectively. There is no curve with minimal largest curvature. The orientation problem (Section 3.6) is seen on one of the diagonals,- the color changes in an unpredictable way.*

3.6 Extraction of the extremal mesh and crest lines

The extremal mesh can be classified into 4 types, depending of the type of extremality of the extremality zero-crossing, $E_g = 0$:

- lines of maximum largest curvature (this is called *crest lines*)
- lines of minimum largest curvature
- lines of maximum second curvature
- lines of minimum second curvature

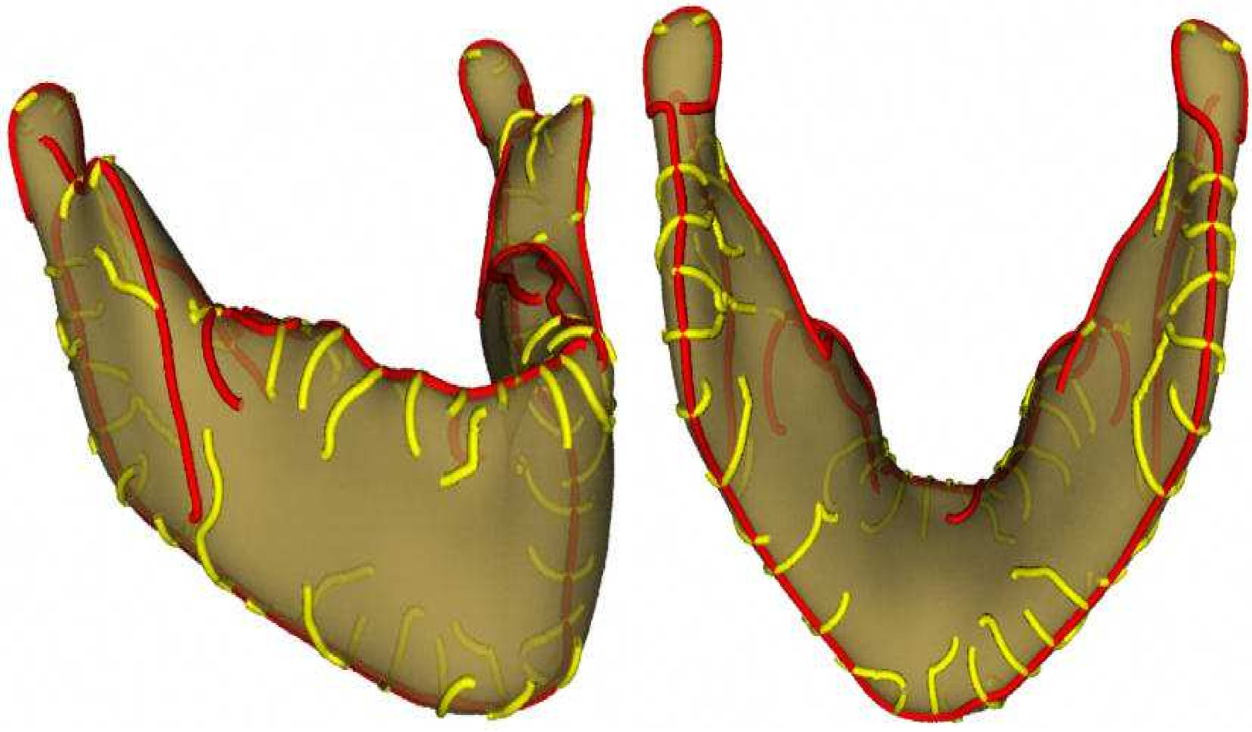

Figure 3.3: *Crest lines (red) and maximal second curvature lines, k_2-max lines (yellow) on a Gaussian smoothed mandible seen from two different viewpoints. Some lines have been removed. Only crest lines and k_2-max lines longer than 20 and 10 points, respectively, are shown. The surface is translucent.*

So, the crest lines are calculated as being the the zero-crossing of $e_1 = \vec{\nabla} k_1 \cdot \vec{t_1}$ (remember that $|k_1| \geq |k_2|$ by definition). But unfortunately this does not work. $e_i = \vec{\nabla} k_i \cdot \vec{t_i}$ is only a correct definition when $\vec{t_i}$ is an oriented direction! If the orientation of $\vec{t_i}$ chnages into $-\vec{t_i}$ (this is still a valid eigenvector), e_i turns into $-e_i$. What is then the meaning of the zero crossing of a value whose sign is meaningless?

This is why, the more complicated expression $E_g = e_1 e_2$ is used and demands that $(\vec{t_1}, \vec{t_2}, \vec{n},)$ is a direct orthonormal basis. When $(\vec{t_1}, \vec{t_2}, \vec{n},)$ being direct, there are only two acceptable choices for the principal direction orientations, which are either $\vec{t_1}, \vec{t_2}$ or $-\vec{t_1}, -\vec{t_2}$. In both cases the product $e_1 e_2$ is the same. E_g is also invariant to a change of the surface orientation, k_1, k_2 just change sign. However a negative isometry (a symmetry with a respect to a plane) inverts the Gaussian extremality values, because of the convention $(\vec{t_1}, \vec{t_2}, \vec{n},)$ direct. Refer to [Thi93] for details about the orientation problem.

Figure 3.2 shows the extremal mesh on a rounded cube. The lines on the rounded edges are the crest lines. Figure 3.3 shows Crest lines and maximal second curvature lines on a mandible. The maximal second curvature lines are "orthogonal" to the crest lines. Together they give a good outline of the mandible.

3.7 Appendix: curvature of the curve $(u, \phi(u))$

In this appendix the curvature for a line l in 2D is calculated given by the parameterization

$$l : \begin{pmatrix} u \\ \phi(u) \end{pmatrix}$$

Section 3.3 for a definition of the notation. Remember that $x = u$, $y = \phi(u)$.

It will be shown that the curvature is given by

$$c(u) = \frac{\phi''}{(1 + \phi'^2)^{3/2}}$$

Let s be the arc length of the curve l, then:

$$ds^2 = dx^2 + dy^2$$

$$\Downarrow$$

$$\frac{ds^2}{dx^2} = 1 + \frac{dy^2}{dx^2} = 1 + \phi'^2$$

$$\Downarrow$$

$$\frac{ds}{dx} = \sqrt{1 + \phi'^2}$$

$$\Downarrow$$

$$\frac{ds}{du} = \sqrt{1 + \phi'^2} \tag{3.23}$$

thus

$$\frac{dl}{ds} = \frac{dl}{dx}\frac{dx}{ds} = \frac{dl}{du}/\frac{ds}{du} = \begin{pmatrix} 1 \\ \phi' \end{pmatrix} (1 + \phi'^2)^{-1/2}$$

$$\Downarrow$$

$$\frac{d}{du}\frac{dl}{ds} = -\frac{1}{2}(1 + \phi'^2)^{-3/2} 2\phi'\phi'' \begin{pmatrix} 1 \\ \phi' \end{pmatrix} + (1 + \phi'^2)^{-1/2} \begin{pmatrix} 0 \\ \phi'' \end{pmatrix}$$

$$\Downarrow$$

$$\frac{d}{du}\frac{dl}{ds} = \begin{pmatrix} -\phi'\phi''(1 + \phi'^2)^{-3/2} \\ \phi''(1 + \phi'^2)^{-1/2} - \phi'^2\phi''(1 + \phi'^2)^{-3/2} \end{pmatrix} \tag{3.24}$$

By definition, the curvature $c(u)$ is given by

$$c(u) = \left\| \frac{d^2 l}{ds^2} \right\| = \left\| \frac{d^2 l}{ds du} \right\| / \frac{ds}{du}$$

From Equations 3.23 and 3.24 we get:

$$c(u) = \frac{\phi''}{(1 + \phi'^2)} / (1 + \phi'^2)^{1/2}$$

$$\Downarrow$$

$$c(u) = \frac{\phi''}{(1 + \phi'^2)^{3/2}} \tag{3.25}$$

The last equation is the desired result.

Bibliography

[Lip69] M. Lipschutz. *Theory and Problems of Differential Geometry.* Schaum's outline series. McGraw-Hill, 1969.

[MBF92] O. Monga, S. Benayoun, and O. D. Faugeras. From partial derivatives of 3D density images to ridge lines. In *CVPR*, pages 354–359, 1992. IEEE Computer Society Conference on Computer Vision and Pattern Recognition.

[Thi93] J.-P. Thirion. The extremal mesh and the understanding of 3D surfaces. Technical Report 2149, INRIA, France, 1993.

[Thi96] J.-P. Thirion. The extremal mesh and the understanding of 3D surfaces. *International Journal of Computer Vision*, 19(2):115–128, 1996.

[TG93] J.-P. Thirion and A. Gourdon. The marching lines algorithm: new results and proofs: part 1 & 2. Technical Report 1881, INRIA, France, 1993.

Chapter 4

Feature Displacement Interpolation

Feature Displacement Interpolation[1]

Mads Nielsen and Per R. Andresen

Abstract

Given a sparse set of feature matches, we want to compute an interpolated dense displacement map. The application may be stereo disparity computation, flow computation, or non-rigid medical registration. Also estimation of missing image data, may be phrased in this framework. Since the features often are very sparse, the interpolation model becomes crucial. We show that a maximum likelihood estimation based on the covariance properties (Kriging) show properties more expedient than methods such as Gaussian interpolation or Tikhonov regularizations, also including scale-selection. The computational complexities are identical. We apply the maximum likelihood interpolation to growth analysis of the mandibular bone. Here, the features used are the crest lines of the object surface.

4.1 Introduction

Given images of an object and a deformed version of the object we wish to compute the displacement field. The overall strategy is to extract features [Mar82], match these, and then interpolate the displacement field. Since feature extraction and matching is not ideal operations, only a very sparse set of reliable features may be extracted and matched. In our current application to 3D human bone-growth analysis, we use the crest lines of the surface as features [TG95]. In this paper, we assume the features and matches are given, and examine the interpolation problem. Since the images are very large 3D images, we only consider direct methods, and not more computational heavy methods such as those based on functional minimization [BZ87, MS85].

In the following we describe methods such as Gaussian interpolation [KW93], Tikhonov regularizations [TA77, Gri81], kriging [Cla79], and an adaptive scheme, and describe their different properties. Finally, we apply the kriging to the growth analysis on synthetic 3D images of cubes, and the mandibular bone obtained from 3D CT scans of the same patient at different time instances [ANK98].

4.2 Displacement interpolation

The values of a displacement field $f : \mathbb{R}^D \mapsto \mathbb{R}^D$ is provided by feature matches in a sparse set of points $\vec{x} = [x_1, x_2, \ldots, x_n]$ as $g(\vec{x})$. In the following, we keep $D = 1$ for notational simplicity, whereas $D = 3$ in the final computational examples. We want the following properties of the interpolation scheme:

- **(i) Approximation criterion**. f must approximate the data values well since localization of the features are assumed relatively precise.
- **(ii) Regularity criterion**. In regions of missing features a regular solution must be created. In general, we will require smoothness (C^∞), but only C^1 and visual regularity (no extra structure introduced).
- **(iii) Asymptotic behavior**. The data must be able of shadowing each other. That is, in a given direction only the nearest data must be weighted.
- **(iv) Maximum principle**. The solution must not extent the solution to values larger than the largest data value or smaller that the smallest data value.

Among the above mentioned interpolation methods, we analyze for these criteria.

4.2.1 Tikhonov regularization or thin-plate splines

A displacement field can be reconstructed as a Maximum A Posteriori (MAP) estimate given noise estimates and a prior of displacement fields. Especially, when the prior is an uncorrelated Gaussian in the displacement gradient magnitude, we obtain Tikhonov regularization [Nie95]:

$$f = \arg\ \min E[f],$$

where

$$E[f] = \sum_i (g(x_i) - f(x_i))^2 + \lambda \int_{\mathbb{R}} (\partial_x f)^2 dx$$

The solution may be obtained as [NFD95]:

$$f(x) = \frac{w(x, \vec{x}) \cdot g(\vec{x})}{w(x, \vec{x}) \cdot \vec{1}}$$

where $g(\vec{x})$ is a vector containing the data values in the data points x arranged in the vector $\vec{x}$, $\vec{1}$ is a vector containing 1's, and $w(x, \vec{x})$ is a vector containing values $w_i(x) = e^{-\frac{|x-x_i|}{\lambda}}$. This is also known as the unbiased estimation of Thin-plate splines [Boo91]. The essential part here is the shape of the filter ($e^{-|x|}$) and that this may be perceived as a standard filtering of the unevenly distributed data points with a re-normalization so that the total filter weight becomes unity. This method does not comply with the approximation criterion and the asymptotic behavior, but does fulfill the maximum principle. The solutions are not in a mathematical sense smooth, but only C^1, which is sufficient for our applications..

4.2.2 Gaussian interpolation

Knutson and Westin [KW93] proposed a similar filtering, but based on Gaussian filters: $w_i(x) = e^{-\frac{(x-x_i)^2}{2\lambda^2}}$. This filter shows different properties than the Tikhonov filter, especially far from data points, which is interesting in the case of very sparse data. It has the required asymptotic behavior. A theoretical difference is that Tikhonov regularizations yields C^1 functions while the Gaussian filter yields C^∞ functions.

The parameter λ yields in both methods a trade off between over-smoothing in regions where many data are given (violation of (i)) and making smooth solutions in areas where only few data are given (property (ii)).

4.2.3 Adaptive Gaussian filtering

A solution to the violations in the normalized filterings may be a local adaption of the scale parameter to the distance of the nearest features: $\lambda(x) = \sqrt{\text{Distance}}$. This, however, has the inexpedient property that data points cannot "shadow" each other. That is, far from a step edge, the solution will take an intermediate value, thus we have violated property (iii). Furthermore, in vast regions, structure may be introduced (violation of (ii)). Other principles of selecting the scale may exhibit different properties.

4.2.4 Kriging or Gaussian regression

The basic problem of the normalized filtering method is that the belief in the smoothness of the solution and the belief in the accuracy of the data values are merged into one smoothness parameter λ. We can phrase the statistical inference problem a little differently and then separate these two parameters, thus yielding *kriging* [Cla79]:

Assume, instead of a prior on the derivative, that the covariance function $C(x, x')$ is known. The covariance function expresses the covariance of the data values in two points x and x'. Typically the closer points are, the more correlated their data values are assumed to be. An interesting aspect is that if this covariance defines a distribution of functions, and if $C(x,x') = e^{-\left(\frac{|x-x'|}{\lambda}\right)^\alpha}$, some well-known function classes appear with probability 1, for different choices of α: $\alpha = 0$ yields white noise, $\alpha \in]0;2[$ yields fractional Brownian motions with $\alpha = 1$ as the classical Brownian motion [MN68], while $\alpha = 2$ (the Gaussian) yields C^∞ functions.

Given the covariance function $C(x,x')$ and an expression of the belief in data as the assumed variance of data values r^2, we can make a maximum likelihood estimation of $f(x)$ as [WR96]

$$f(x) = \frac{w(x,\vec{x})Q^{-1}g(\vec{x})}{w(x,\vec{x})Q^{-1}\vec{1}}$$

where $w(x,\vec{x})$ is a vector containing $w_i = C(x,x_i)$, and Q is a matrix containing $Q_{ij} = C(x_1,x_2) + r^2\delta_{ij}$. The intuitive interpretation of the introduction of Q^{-1} is that, prior to the regularizations based on the covariance function, an inverse filtering is performed to make the samples uncorrelated. In terms of scale-space we might say that we have data given at some scale λ. To interpolate we first perform a deblurring to scale zero, interpolate, and then blur back to the current scale. The solution has the same regularity properties as the corresponding normalized filtering ($\alpha = 1$, thin-plate splines are C^1 and $\alpha = 2$, normalized Gaussian filtering is C^∞). Varying the parameter r yields different properties of the solutions, and in the limit $r \mapsto \infty$, we are back to normalized filtering.

4.3 Interpolation properties

The properties of the different interpolation models are noted in the figure captions below. Below we give a table indicating properties. Notice that all methods except the adaptive scale method may be formulated as Kriging. If $\alpha = 1$ and $r^2 = \infty$ Kriging yields Tikhonov regularization, while $\alpha = 2$ and $r^2 = \infty$ yields Gaussian interpolation.

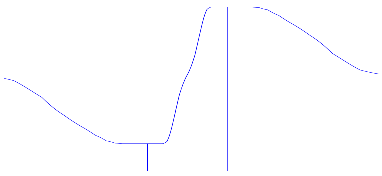

Figure 4.1: *Adaptive filtering, $\alpha = 2$. This violates the principle of asymptotic behavior, only the closest value should be used. Furthermore notice the bump in the middle; extra structure is introduced thus violating the regularity criterion.*

Method	(i)	(ii)	(iii)	(iv)
$\alpha = 1, r^2 = 0$	+	C^1	+	+
$\alpha = 1, r^2 = 1$	-	C^1	-	+
$\alpha = 1, r^2 = \infty$	-	C^1	-	+
$\alpha = 2, r^2 = 0$	+	C^∞	-	-
$\alpha = 2, r^2 = 1$	-	C^∞	-	-
$\alpha = 2, r^2 = \infty$	-	C^∞	+	+
Adaptive scale	+	C^1	-	+

4.4 Summary

We are given very reliable, but also very sparse feature matches. Based upon this situation we have formulated 4 criteria for a displacement interpolation. Among standard regularization schemes they cannot be fulfilled simultaneously. Using a formulation of the interpolation problem normally applied in geo-statistics, Kriging, we may fulfill all criteria simultaneously, having only one free scale parameter. This has been applied to 3D growth analysis based upon crest line matches.

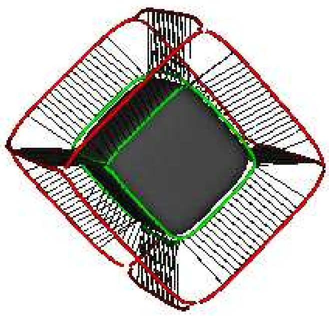

Figure 4.2: *Crest lines and their matchings on two cubes of same orientation and position, but with a relative size change of 1/3. Results are obtained automatically. Notice the erroneous matching so that only the central part of the crest lines at the larger cube is used. This is made deliberately so as to expose the interpolation properties.*

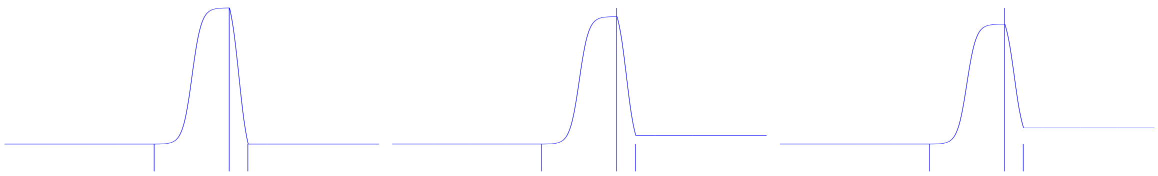

Figure 4.3: *Kriging, $\alpha = 1$, $\lambda = 50$, from left to right $r^2 = 0$, $r^2 = 1$, $r^2 \approx \infty$. The vertical lines corresponds to data points with values corresponding to the height of the lines. The left figure is the only of all the interpolation techniques in this paper that satisfy all 4 criteria. When $r^2 > 0$ the approximation and asymptotic behavior are violated.*

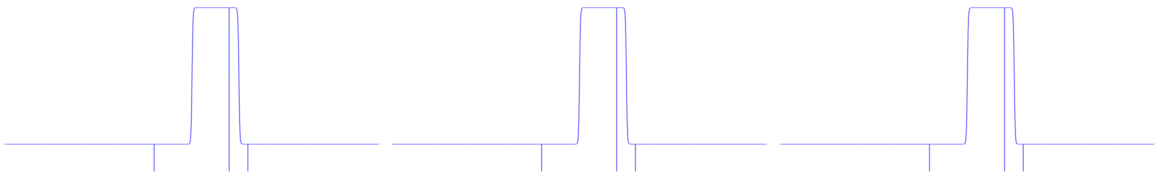

Figure 4.4: *Kriging, $\alpha = 1$, $\lambda = 5$, from left to right $r^2 = 0$, $r^2 = 1$, $r^2 \approx \infty$. This figure is identical to the above with the exception of a smaller scale, which makes the solution go towards a step function.*

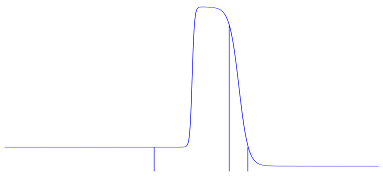

Figure 4.5: *Kriging, $\alpha = 2$, $\lambda = 50$, from left to right $r^2 = 0$, $r^2 = 1$, $r^2 \approx \infty$. Here, the left violates the maximum principle and the asymptotic criterion, while the right violates the approximation principle. The middle violates all three, but to a smaller extent.*

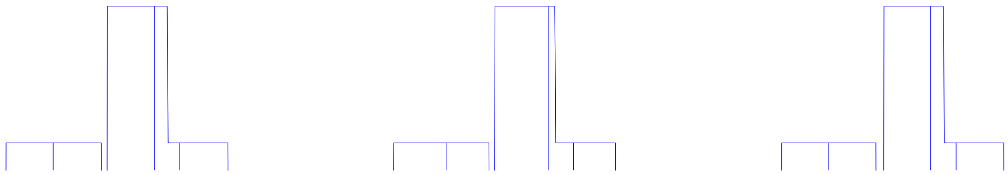

Figure 4.6: *Kriging, $\alpha = 2$, $\lambda = 5$, from left to right $r^2 = 0$, $r^2 = 1$, $r^2 \approx \infty$. The same as the above, but width smaller scale. Here we run into numerical problems and in some points no solution is given. Furthermore, the solutions are closer to a step function, making the above criteria violations smaller.*

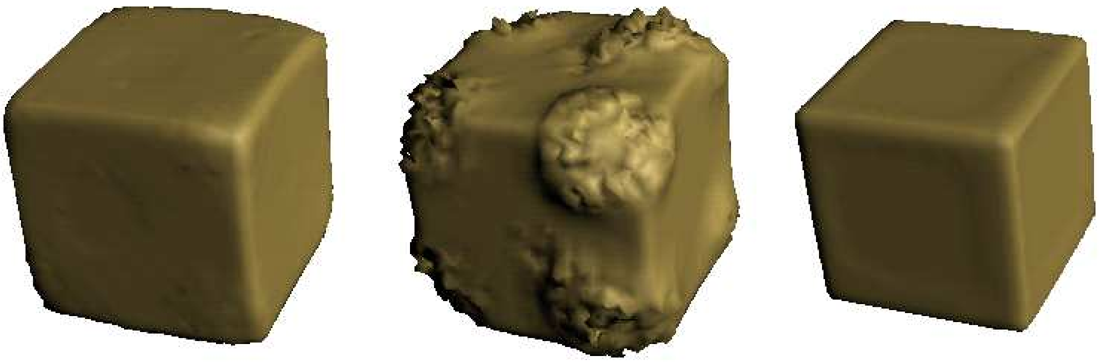

Figure 4.7: *Reconstruction of the smaller cube at the size of the larger cube. Displacements are computed on the basis of crest lines on the two cubes, matching and interpolation using* $\alpha = 1$, $\sigma = 2$, $r^2 = 10^{-3}$ *(left),* $\alpha = 2$, $\sigma = 2$, $r^2 = 10^{-3}$ *(middle),* $\alpha = 1$, $\sigma = 2$, $r^2 \approx \infty$ *(right). The leftmost corresponds to the only interpolation not violating any criteria. The central does not satisfy the maximum principle, and the asymptotic behavior, while the rightmost does not satisfy approximation criterion, hence the resulting cube is too small.*

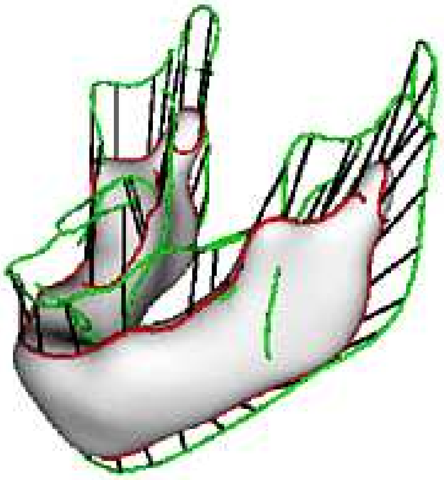

Figure 4.8: *Crest line matches on the mandibular bone of the same patient scanned at age 21 month and 7 years.*

Figure 4.9: *Interpolated growth of the mandible based on 3 CT scans at age 9 month, 21 month, and 7 years. Spatial interpolation based on the parameter free adaptive scale method, temporal interpolation based upon a second order polynomial model.*

Bibliography

[ANK98] P. R. Andresen, M. Nielsen, S. Kreiborg. 4D shape-preserving modelling of bone growth. In *Medical Image Computing and Computer-Assisted Intervention - MICCAI'98*, volume 1496 of *Lecture Notes in Computer Science*, pages 710–719. Springer, 1998.

[BZ87] A. Blake and A. Zisserman. *Visual Reconstruction.* MIT Press, Cambridge, Mass., 1987.

[Boo91] F. L. Bookstein. *Morphometric Tools for Landmark Data.* Cambridge University Press, 1991.

[Cla79] I. Clark. *Practical Geostatistics.* Elsevier Applied Science, 1979.

[Gri81] W. E. L. Grimson. *From Images to Surfaces.* MIT Press, Cambridge MA, 1981.

[KW93] H. Knutsson and C. F. Westin. Normalized and differential convolution. In *CVPR93*, pages 515–523, 1993.

[MN68] B. B. Mandelbrot and J. W. van Ness. Fractional Brownian motions, fractional noises, and applications. *SIAM Review*, 10(4):422–437, 1968.

[Mar82] D. Marr. *Vision.* W. H. Freeman & Co., 1882.

[MS85] D. Mumford and J. Shah. Boundary detection by minimizing functionals. In *Proc. IEEE Conf. on Computer Vision and Pattern Recognition*, 1985.

[Nie95] M. Nielsen. *From Paradigm to Algorithms in Computer Vision.* PhD thesis, DIKU, Datalogisk Institut ved Københavns Universitet, Copenhagen, Denmark, 1995. DIKU-95-8.

[NFD95] M. Nielsen, L. Florack, and R. Deriche. Regularization, scale space, and edge detection filters. *Journal on Mathematical Imaging and Vision*, 7:291–307, 1997.

[TG95] J.-P. Thirion and A. Gourdon. Computing the differential characteristics of iso-density surfaces. *Computer Vision, Graphics, and Image Processing: Image Understanding*, 61(2):109–202, 1995.

[TA77] A. N. Tikhonov and V. Y. Arsenin. *Solution of Ill-Posed Problems.* Winston and Wiley, Washington DC, 1977.

[WR96] C. K. I. Williams and C. E. Rasmussen. Gaussian processes for regression. *Advances in Neural Information Processing Systems*, 8, 1996.

Chapter 5

4D Shape-Preserving Modelling of Bone Growth

4D Shape-Preserving Modelling of Bone Growth[1][2]

Per Rønsholt Andresen, Mads Nielsen, and Sven Kreiborg

Abstract

From a set of temporally separated scannings of the same anatomical structure we wish to identify and analyze the growth in terms of a metamorphosis. That is, we study the temporal change of shape which may provide an understanding of the biological processes which govern the growth process. We subdivide the growth analysis into growth simulation, growth modelling, and finally the growth analysis. In this paper, we present results of growth simulation of the mandible from 3 scannings of the same patient in the age of 9 month, 21 month, and 7 years. We also present the first growth models and growth analyzes. The ultimate goal is to predict/simulate human growth which would be extremely useful in many surgical procedures.

5.1 Introduction

This paper presents a non-linear growth model which to a very good approximation interpolates the growth as seen on the human mandible (the lower jaw). The results comply with the existing 2D theory on mandibular growth [BS83]. These experiments use a unique 4D data set containing three Computerized Tomography (CT) scans[3] of the same patient with Apert syndrome, but with

[1]This work is partly supported by the Danish Technical Research Council, registration number 9600452.

[3]The scans were performed for diagnostic and treatment planning purposes.

normal mandibular development, taken at three ages (9 month, 21 month, and 7 years old). In many situations, surgeons need information about the growth of the jaws, particularly when performing pediatric craniofacial surgery. After surgery, the bones continue to grow, and therefore in order to optimize the intervention, there is a need to predict/simulate growth. Also for basic understanding and teaching, we have a need for these models. We subdivide the growth study into growth simulation, growth modelling, and finally the growth analysis. Growth simulation is the data driven analysis, where we try to fit an (almost) arbitrary model to the data. In growth modelling, we have a model and wish to evaluate if the data fits the model. When we are doing growth analysis, the process is reversed, and we try to extract information from the models, such as active areas, spatial correlations, predicted changes, etc. In contrast to normal biological tissue growth, bone grows only on the surface. The interior is rigid and does not change shape [BS83]. The growth of a bone can be subdivided into *deposition* (adding bone) and *resorption* (removal of bone). Because the deposition and resorption happen all over the surface of the bone at different speeds, this results in non-linear growth [BS83]. For the mandible the condyles are the most active areas, and are therefore important to be followed over time. Homologous[4] points followed over time, define a spatio-temporal vector field (the *growth vector field* or just *vector field* or *flow field*). The goal of *growth simulation* is the identification of the spatio-temporal vector field. Many different vector fields will satisfy the constraints given by the data and the definitions of homologous points. Thus a *growth model* (or interpolation model) must be used for the determination of a unique vector field.

We distinguish between models having the same number of degrees of freedom as the data and over-constrained models. We will use the first in the process of growth simulations, while over-constrained models are used for growth modelling. The simulation is a mere data interpolation,

[4]Homologous = having the same relative position, value, or structure.

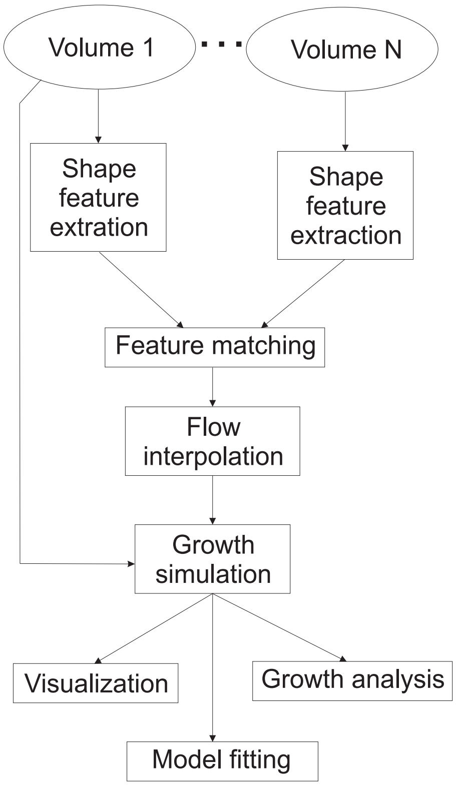

Figure 5.1: *Flow chart of the algorithms involved in the growth analysis.*

whereas the modelling will test whether data comply to a given model. In Figure 5.1 the information flow is shown.

Finally, in the *growth analysis*, we will extract information from the simulated or modeled vector field in order to identify local biological processes and/or physical conditions that govern the remodeling of the bone. In this paper, we estimate the resorption and deposition on the surface of the mandibular bone.

In earlier work on simulating the growth of the mandibular bone [BNGK97] the interpolation has been performed directly on the surface position. But the time steps are large, and a direct surface position interpolation as carried out in that work will not preserve the overall shape. Thus, intermediate steps will not necessarily look like mandibles. See figure 5.2.

In Section 5.2, we will give one definition of homologous points in terms of the extremal mesh

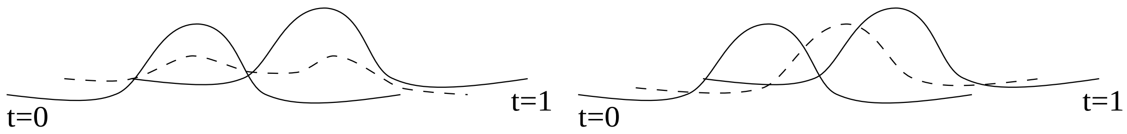

Figure 5.2: *Surface interpolation illustration to the left is a linear interpolation in position of closest point. The top at $t = 0$ will disappear and at the same time a new top will appear. To the right is a linear interpolation of shape feature positions such as maximally curved points on the surface. Here, the top moves to the right over time.*

[Thi96] (which are lines) and the different types of ridge lines. These homologous equivalent lines are matched, as described in Section 5.3. Since this yields a very sparse vector field the interpolation becomes crucial and is described in Section 5.4. In Section 5.5, we describe existing 2D models of the growth of the mandible, and use these models for a 3D growth modelling. In Section 5.6, we extract properties of the modeled flow fields such as the local amount of resorption and deposition. Section 5.7 discusses our results and describes future work.

5.2 Local shape features

The growth vector field links homologous points, or points of *equivalent morphology*. In this section, we define equivalence classes of points on a surface. The local shape of a surface is totally characterized by the principal curvatures k_1, k_2 ($k_1 > k_2$) and their derivatives in the coordinate system defined by the principal directions (t_1, t_2) [dC76]. Since the bone topology is not changing in our studies, we may model the growth process by a 3D diffeomorphism (a one-to-one differential mapping). This corresponds to D'Arcy Thompson classical methods of transformations [Tho17]. The principal curvatures and directions will in general change when exposed to this non-linear diffeomorphism, and cannot directly be used for registration. However, certain *shape singularities* are stable in the sense that they cannot be removed by an infinitesimal perturbation [BG84]. Here,

Figure 5.3: *The crest lines on the three smoothed mandibles at 9 month (left), 21 month (middle), and 7 years old (right). The surfaces are translucent.*

we give a list of some stable shape features.

Shape feature	Definition	Dimensionality
Umbilic point	$k_1 = k_2$	0
Critical curvedness [Koe90]	$\partial_{t_1} C = 0 \wedge \partial_{t_2} C = 0$, def: $C = k_1^2 + k_2^2$	0
Extremal points	$\partial_{t_1} k_1 = 0 \wedge \partial_{t_2} k_2 = 0$	0
Parabolic line	$k_1 = 0 \vee k_2 = 0$	1
Ridge line (or extremal mesh)	$\partial_{t_1} k_1 = 0 \vee \partial_{t_2} k_2 = 0$	1
Crest line	$\partial_{t_1} k_1 = 0 \wedge \partial_{t_1^2} k_1 < 0$, def: $\lvert k_1\rvert > \lvert k_2\rvert$	1
Sub-parabolic line [BG84]	$\partial_{t_2} k_1 = 0 \vee \partial_{t_1} k_2 = 0$	1

Shape features with dimension ≥ 2 will not be discussed in this paper.

The ridge lines (or extremal mesh) can be partitioned into four types corresponding to respectively maximum or minimum in k_1 and k_2. We use the maxima in (the absolute value of) both k_1 and k_2.

The above mentioned shape features are all *structurally stable*, but even though they can not be removed by infinitesimal perturbations, they will in general change topology under finite perturbations.

We work with the extraction and matching of ridge lines in a scale-space setting [Koe84] (see the following section). Also the scale-space evolution of ridge lines is not totally understood even though some aspects are covered in the literature [Dam93, EGM$^+$94, Fid97]. Thus, theoretical issues are still to be clarified. However, by making a matching which only accepts good matches (see the following section), we obtain satisfying results. The crest lines of the mandibles can be seen in Figure 5.3.

5.3 Feature matching

As features we will only consider the lines with maximally k_1 (crest lines) and maximally k_2 (here, called k_2-max lines) in the extremal mesh. The overall framework follows the ideas of [STA98]. First we extract the crest lines and k_2-max lines for each dataset at scale 3.0 (matching scale) and 1.0 (localization scale). The crest lines at scale 3.0 are registered pairwise (here, it means only the temporally neighboring data-volumes), and initial vector fields are calculated. The k_2-max lines are then deformed according the initial vector fields and registered. From the two sets of matches (one from the crest lines, the other from the k_2-max lines) final vector fields are calculated. This procedure is repeated for scale 1.0, but the lines are initially deformed according to the the final vector fields for scale 3.0.

The steps in the registration are always the same. First moment-registration, then two first order polynomial deformations, followed by two second order polynomial deformations. Lastly a totally non-rigid deformation is applied (all points on the lines move freely). For all the registration methods (including the non-rigid) they must satisfy the restriction that the deformation must be a 3D diffeomorphism. See Figure 5.6 for an example of matches between two set of crest lines at scale 3.0.

5.4 Flow interpolation

The matching provides us with a very sparse set of vectors. This vector field must be interpolated such as to yield a differentiable spatially dense field of spatio-temporal deformation vectors: a diffeomorphism (that its, spatial the Jacobian is nowhere vanishing).

We wish the interpolation to satisfy the following constraints: (i) approximation, (ii) regularity, (iii) shadowing, (iv) maximum principle. (i) The interpolated vector field must approximate the data values well since localization of the features are assumed relatively precise. (ii) In regions of missing features a smooth solution must be created. We do assume a regular growth. (iii) The data must be able of shadowing each other. That is, in a given direction only the nearest data must be weighted. In this way, we avoid that features from the "other side" of a thin structure influence the local solution. (iv) The solution must not extend the solution to values larger than the largest data value or smaller than the smallest data value. We assume that the ridge lines also correspond to lines of extreme growth.

We address this as a statistical inference problem. Assume that the covariance function $C(x, x')$ is known. The covariance function expresses the covariance of the vector field values in two points x and x'. Typically, the closer the points are, the more correlated their data values are assumed to be. An interesting aspect is that if this covariance defines a distribution of functions, and if $C(x, x') = exp(-(|x - x'|/\lambda)^{\alpha})$, some well-known function classes appear with probability 1, for different choices of α: $\alpha = 0$ yields white noise, $\alpha \in]0; 2[$ yields fractional Brownian motions with $\alpha = 1$ as the classical Brownian motion [MN68], while $\alpha = 2$ (the Gaussian) yields C^{∞} functions. Given the covariance function $C(x, x')$ and an expression of the belief in data as the assumed variance of data values r^2, we can make a maximum likelihood estimation of $f(x)$ as [WR96]

$$f(x) = \frac{w(x,\vec{x})Q^{-1}g(\vec{x})}{w(x,\vec{x})Q^{-1}\vec{1}} \tag{5.1}$$

where $w(x,\vec{x})$ is a vector containing $w_i = C(x, x_i)$, and Q is a matrix containing $Q_{ij} = C(x_1, x_2) + r^2\delta_{ij}$. The intuitive interpretation of the introduction of Q^{-1} is that, prior to the regularizations based on the covariance function, an inverse filtering is performed to make the samples uncorrelated. In terms of scale-space, we might say that we have data given at some scale λ. To interpolate, we first perform a de-blurring to scale zero, then interpolate and then blur back to the current scale.

This method satisfies all criteria when $\alpha = 1$ and $r = 0$ [NA98]. λ can be chosen freely, so as to adjust the smoothness of the interpolated vector field. In Figure 5.4, the deformation of the mandible is shown as it is transported along the deformation vector field.

5.5 Growth modelling

We have the general model $\vec{g}(\vec{\theta}(x,y,z),t)$, $\vec{g} : \mathcal{R}^3 \mapsto \mathcal{R}^3$ (for fixed t), and the 3D volumes $v_i(x,y,z)$, where $\vec{\theta}(x,y,z)$ is the parameters for $\vec{g}$, and (x,y,z) defines a point in $\mathcal{R}^3$. t is the time. $i = \{1,\dots,n\}$. n is the total number of volumes. t_i is the time at the ith scan. We need to pick a reference volume, let's say v_n. All deformations will then be applied to this set, i.e. a simulated volume at time t is given by $\tilde{v}_n(\vec{g}(\vec{\theta}(x,y,z),t), v_n(x,y,z))$ or $\tilde{v}_n(x,y,z,t)$ for short. We want to solve the problem

$$\hat{\theta} = \arg\min_{\theta} \sum_{i=1}^{n} \left[\sum_{x,y,z} \{\tilde{v}_n(x,y,z,t_i) - v_i(x,y,z,t_i)\}^2 \right] \tag{5.2}$$

Note, when having $\vec{g}(\vec{\theta}(x,y,z),t)$, the actual deformation on the volume v_n from time t_n to t, can always be made by a linear deformation (we just pick the straight line between two homologous points in $\tilde{v}_n(x,y,z,t)$ and $v_n(x,y,z)$). In general, this leads to a non-linear optimization problem,

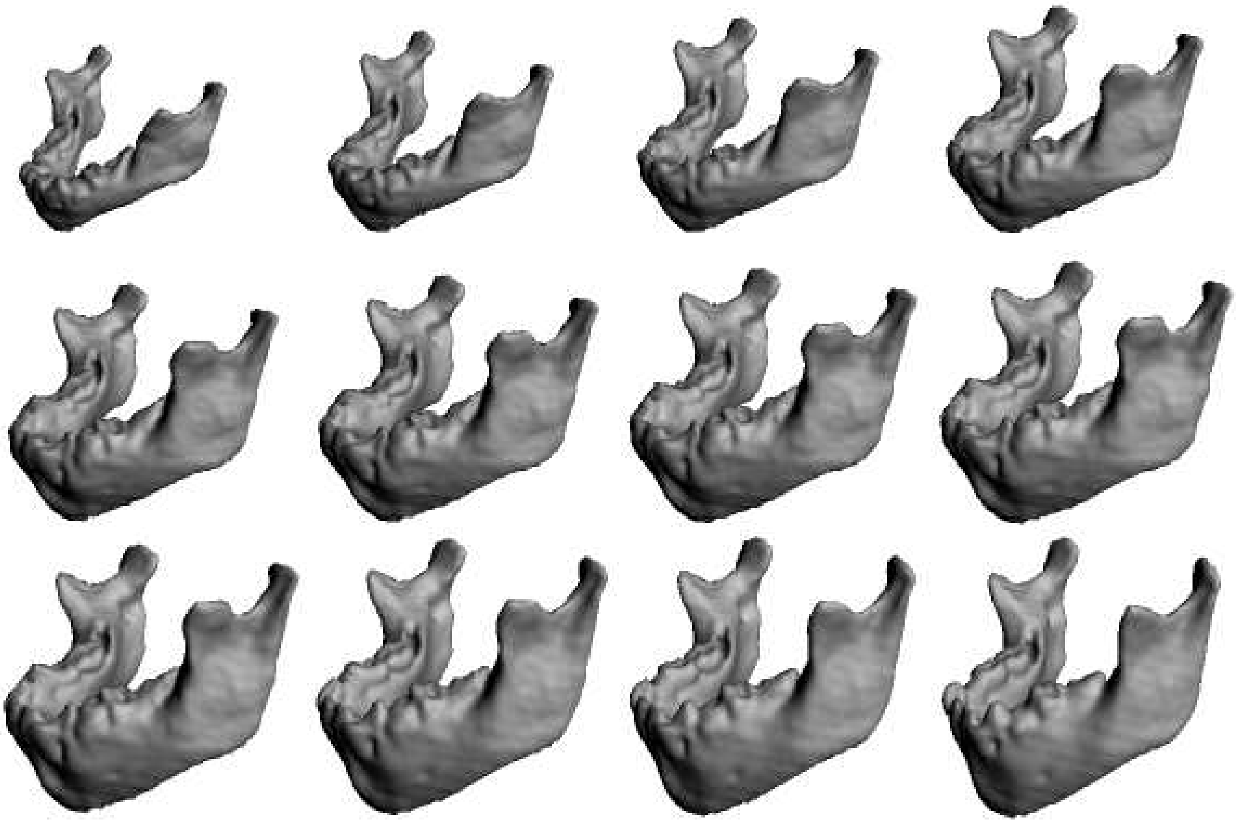

Figure 5.4: *Result of deformations on the 7 years old mandible using a second order polynomial model (see section 5.5). The top left and right images are the deformation at 9 month and 21 month, respectively. The bottom right image is the original 7 years old mandible.*

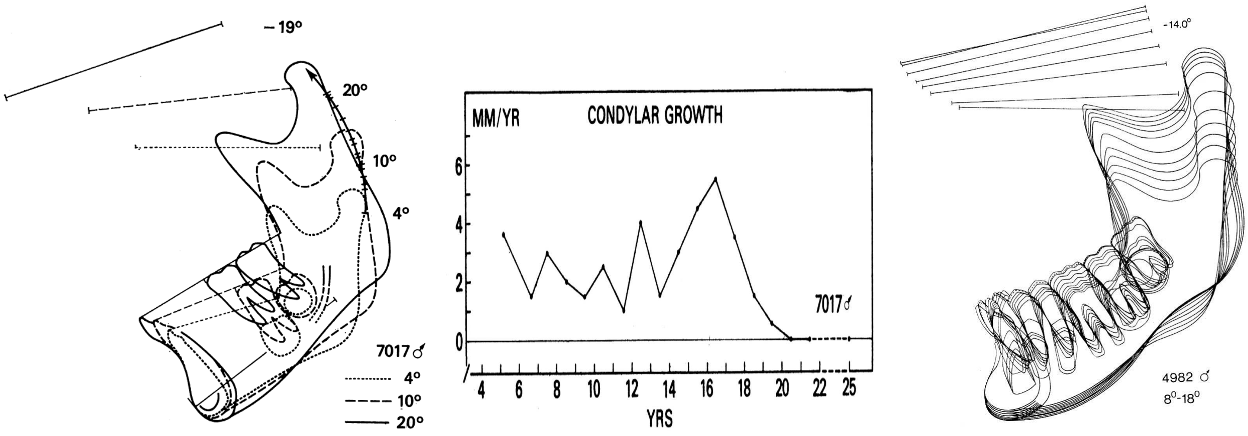

Figure 5.5: *Left: mandibular tracing at three age stages (this is not the same patient as for the CT scans) superimposed in a reference line in the corpus with reference to natural structures. Middle: curve for yearly rate of condylar growth. Both plots are data from the same patient with a normal mandibular growth. Right: mandibular growth tracing superimposed by means of metallic implants, illustrating the yearly growth and remodeling of the mandible and the eruption if the teeth, as seen in profile view. From [BS83].*

but if we pick models, linear in the parameters, regression analysis [KPK90] can be used. Linear models

$$\vec{g}(\vec{\theta}(x, y, z), t) = \vec{\theta}(x, y, z) * t \tag{5.3}$$

have been used in previous work [BNGK97]. This model has the drawback that a point, $\vec{p}$, can only grow in the direction of the vector $\vec{\theta}(\vec{p})$. From Figure 5.5, it is obvious that the growth of the mandible is not linear. The simplest non-linear model is a polynomial model (with $k \leq 2$)

$$\vec{g}(\vec{\theta}(x, y, z), t) = t^k \vec{\theta}_k + \cdots + t^2 \vec{\theta}_2 + t\vec{\theta}_1 + \vec{\theta}_0,\ \vec{\theta} = \left[\vec{\theta}_k \cdots \vec{\theta}_2\ \vec{\theta}_1\ \vec{\theta}_0\right] \tag{5.4}$$

As seen from Figure 5.5, the growth speed is not constant, but this can be handled by the model by re-parameterizing the time variable, t.

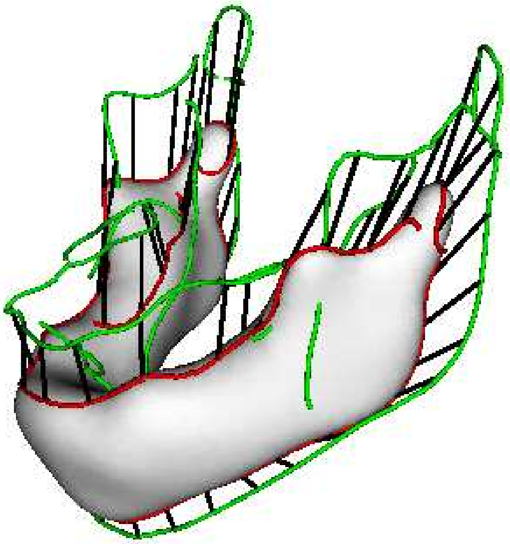

Figure 5.6: *The final matches (lines in black) between two sets of crest lines. The crest lines on the 21 month and 7 years old mandible are red and green, respectively. It is seen that the condyles on the two mandibles are matched together. For visual clarity only every eighth match is shown.*

Because we only have three scans of the same patient, we can not go above the second order model[5] (k=2). A second order polynomial model is estimated using the matches between scan one and two, and scan two and three. Interpolation of the volumes is carried out by deforming the last scan (see Figure 5.4). Because the calculation of the deformation field from one scan to the next scan is not perfect, we have some model errors (even though the model itself doesn't have any error) which are seen in Figure 5.7. Other possible models include logarithmic spirals and power functions, known from the theory of growth [Tho17] or spatially constrained models.

5.6 Growth analysis

The growth modelling is on its own also a growth analysis since residuals to an over-constrained model may be used for validating the model. The growth simulations, as we obtain it in Figure 5.4,

[5]This leads to a model error equal zero, because the number of parameters equals the number of volumes.

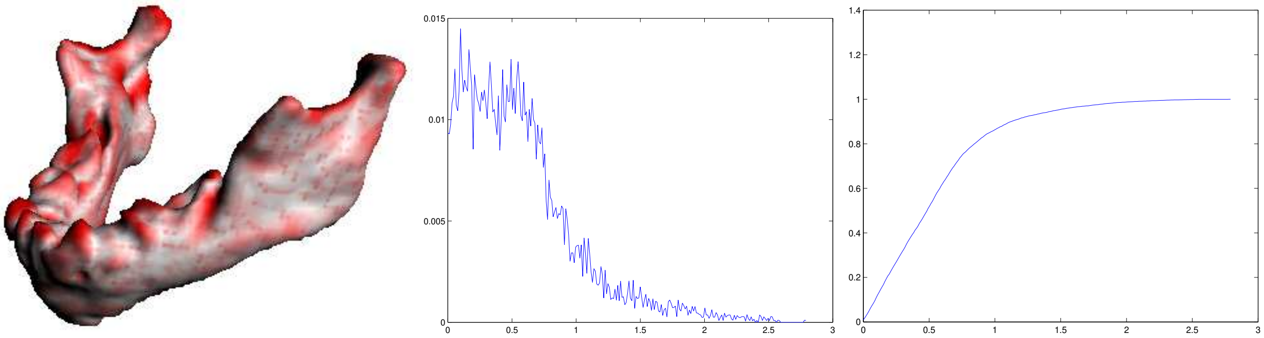

Figure 5.7: *The plots in the middle and right shows the frequency and accumulated distribution of the distance errors (the distance errors are measured as the minimal distances from the deformed surface to the original surface) between the 9 month old mandible and the 7 years old mandible deformed to 9 month. The mean error is 0.57mm, and 95% of the errors are less than 1.46mm. The maximal error is 2.79mm. This should be compared to the size of the 7 years old mandible which is approximately* $(X, Y, Z) = (80mm, 100mm, 40mm)$. *The left surface is colored red when the error* $> 1.46mm$, *else white. When the surface changes a lot the matching algorithm does not match with lines in the "holes" of the surface, but are more likely to match with a line on the "top", therefore we see the errors located at places with a lot of changes in the shape. If we applied a surface to surface registration afterwards, the errors would be minimal.*

can be used for a local characterization of the growth. The model errors at 9 month are shown in Figure 5.7. Using anatomical structures which are also spatially stable, a rigid registration of the different time instances of the bone can be obtained. In the mandible, the nerve canal is known to be spatially stable, and can serve as an anchor for a rigid registration. In this coordinate system, the spatio-temporal growth simulation vector field can be used directly for estimation of the amount of surface resorption and deposition. In Figure 5.8 we show the surface remodeling in terms of a color coding of the mandible as respectively the remodeling (the local velocity vector projected to the surface normal) and the speed of the homologous points. The remodeling is consistent with earlier

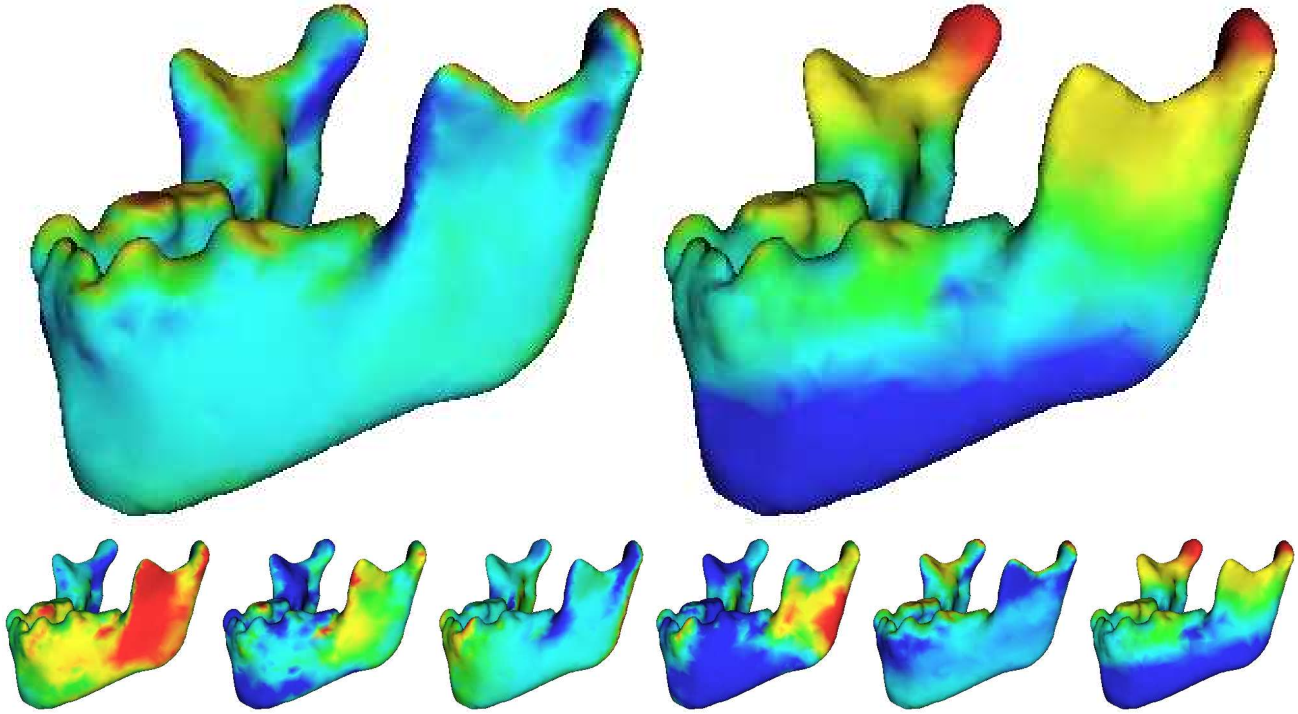

Figure 5.8: *First row: the 7 years old mandible colored with the local velocity vector projected to the surface normal (left) and the length of the velocity vector (right). The next row shows X (first two images), Y (next two images), and Z (last two images) components of the velocity vector (projection and length, respectively). Read text in "Growth Analysis" for further explanation.*

2D studies on larger statistical material [BS83]. Especially we see the expected large movement of the condyle.

5.7 Summary

We have simulated the growth of the mandible from 3 CT scans of the same patient at ages 9 month, 21 month, and 7 years. The intermediate interpolated time instances also exhibit shapes that clearly are "mandible shaped". This is due to the strategy of interpolating in shape feature position instead of a simple surface position interpolation [BNGK97]. The major errors in the simulations are found in the region where teeth are appearing. In principle, they should a priori have been removed from the mandible surfaces, as they are not part of the mandible but separate objects, and the shape change can not be contributed to a surface remodeling. The shape modelling in this paper has used simple second order polynomial temporal models. They exhibit some inexpedient features inherent for polynomial approximations. An example is a tendency to a contraction of the two condyles towards each other if a time extrapolation is attempted. Since the ultimate goal of a growth analysis and modelling is a prediction of the shape of the craniofacial complex. Future work will be devoted to examination of superior temporal models and validation on more datasets. Extension of the feature matching from ridge lines to iso-surfaces, as mentioned in Figure 5.7, may reduce errors. Also development of a skeletal growth atlas, which contains growth models for all bones would be interesting.

Bibliography

[BG84] J. W. Bruce and P. J. Giblin. *Curves and Singularities.* Cambridge University Press, Cambridge, 1984.

[BNGK97] M. Bro-Nielsen, C. Gramkow, and S. Kreiborg. Non-rigid image registration using bone growth model. In *CVRMed-MRCAS'97*, Lecture Notes in Computer Science, pages 3–12. Springer, 1997.

[BS83] A. Björk and V. Skieller. Normal and abnormal growth of the mandible. A synthesis of longitudinal cephalometric implant studies over a period of 25 years. *European Journal of Orthodontics*, 5:1–46, 1983.

[Dam93] J. Damon. Local Morse theory for solutions to the heat equation and Gaussian blurring. *Journal of Differential Equations*, 1993.

[dC76] M. P. do Carmo. *Differential Geometry of Curves and Surfaces.* Prentice-Hall, 1976.

[EGM+94] D. Eberly, R. Gardner, B. Morse, S. Pizer, and C. Scharlach. Ridges for image analysis. *Journal of Mathematical Imaging and Vision*, 4(4):353–373, 1994.

[Fid97] M. Fidrich. Following feature lines across scale. In *ScaleSpace97*, 1997.

[KPK90] D. Kazakos and P. Papantoni-Kazakos. *Detection and Estimation.* Computer Science Press, 1990.

[Koe84] J. J. Koenderink. The structure of images. *Biological Cybernetics*, 50:363–370, 1984.

[Koe90] J. J. Koenderink. *Solid Shape.* MIT Press, Cambridge, Massachusetts, 1990.

[MN68] B. B. Mandelbrot and J. W. V. Ness. Fractional brownian motions, fractional noises, and applications. *SIAM Rev*, 1968.

[NA98] M. Nielsen and P. R. Andresen. Feature displacement interpolation. In *IEEE 1998 International Conference on Image Processing (ICIP'98)*, pages 208–212, 1998.

[STA98] G. Subsol, J.-P. Thirion, and N. Ayache. A general scheme for automatically building 3D morphometric anatomical atlases: application to a skull atlas. *Medical Image Analysis*, 2(1):37–60, 1998.

[Thi96] J.-P. Thirion. The extremal mesh and the understanding of 3D surfaces. *International Journal of Computer Vision*, 19(2):115–128, 1996.

[Tho17] D. W. Thompson *On Growth and Form.* Cambridge University Press, 1917.

[WR96] C. K. I. Williams and C. E. Rasmussen. Gaussian processes for regression. In *Advances in Neural Information Processing Systems 8. Proceedings of the 1995 conferences*, pages 514–520, 1996.

Chapter 6

Non-rigid Registration by Geometry-Constrained Diffusion

Non-rigid Registration by Geometry-Constrained Diffusion[1]

Per Rønsholt Andresen and Mads Nielsen

Abstract

Assume that only partial knowledge about a non-rigid registration is given so that certain points, curves, or surfaces in one 3D image map to certain certain points, curves, or surfaces in another 3D image. We are facing the aperture problem because along the curves and surfaces, point correspondences are not given. We will advocate the viewpoint that the aperture and the 3D interpolation problem may be solved *simultaneously* by finding the *simplest* displacement field. This is obtained by a geometry-constrained diffusion which yields the simplest displacement field in a precise sense. The point registration obtained may be used for growth modeling, shape statistics, or kinematic interpolation. The algorithm applies to geometrical objects of any dimensionality. We may thus keep any number of fiducial points, curves, and/or surfaces fixed while finding the simplest registration. Examples of inferred point correspondences in a longitudinal growth study of the mandible are given.

Keywords: aperture-problem, automatic landmark detection, diffusion, kD-tree, non-rigid registration, simplest displacement field, homology.

6.1 Introduction

In a registration, we wish to establish the spatial correspondence of points in two images. Correspondence is defined through the concept of homology except in pathological cases. In general, homologous points will, dependent on the medical task, reflect similar anatomy, functionality, or geometry, etc. In this paper, we assume that homologous *objects* have been defined *a priori*. Therefore, we seek an automatic method for establishing *point* correspondences based on *object* correspondences. Pursuing this, we presume that: 1) the optimal registration is a mapping between homologous points, 2) the underlying biological process is smooth and homologous points do not “change place” i.e., the ordering of the anatomical structures is preserved. Formally: the registration field must not fold or be torn apart. It is then a homeomorphism.

In other words, within the objects, a solution to the generalized *aperture problem* must be chosen. In this paper, we introduce the concept of *geometry-constrained diffusion* for solving the interpolation and aperture problems simultaneously.

When performing shape statistics or analyzing (longitudinal) shape development, the tools from shape statistics (see e.g., [Boo97]) require point matches. That is, to perform a statistical analysis of the variation of shapes we must identify homologous *points* on the shape samples. When having only a few landmarks the registration may be performed manually, but for thousands of points it becomes tedious and practically impossible. In many cases punctual landmarks are hard to establish in images, and the process requires considerable prior anatomical knowledge.

Automated methods using geometrical features such as crest lines [Thi96] are powerful, but do not provide a *dense* field, and may give problems in regions where shape features change topology so that correct matching is not possible. We propose using *geometry-constrained diffusion* for inferring the locally simplest non-rigid object registration.

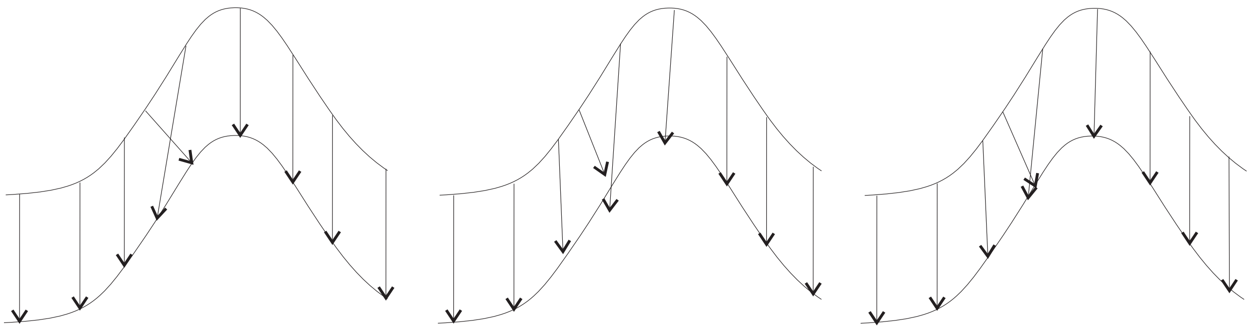

Figure 6.1: *The images show schematically how the diffusion algorithm works on the deformation field. The Cartesian components of the initial deformation field (arrows in the left image) are Gaussian smoothed. Some of the links have now diverged from the surface (middle image) and must be projected back on to the surface (right image). The fold (the two crossing arrows) is removed by repeating the steps until the field does not change.*

The result of *geometry-constrained diffusion* is a dense, continuous, invertible displacement field (a homeomorphism). Many fields may fulfill the geometrical constraints given by the objects. The diffusion process gradually simplifies an initial registration field. In general, diffusion is a gradient ascent in entropy. That is, locally it changes the registration field so as to remove its structure as fast as possible. An unconstrained diffusion in this way leads to an affine registration. The geometry-constrained diffusion also simplifies the registration field as fast as possible, but is limited locally so as to preserve the object mappings (see Fig. 6.1).

In section 6.3, the theory of geometry-constrained diffusion is summarized. Section 6.4 describes the implementation. Examples of the simplification of an initial crest line based non-rigid registration are shown in section 6.5.

6.2 Related work

In the literature, many algorithms for non-rigid registration exist. In this paper, we address the equally important problem of measuring the complexity of the geometrical deformation in a non-rigid registration. This measure may be introduced either by having only a finite number of semi-local low parameter registrations, or a viscous fluid or elasticity constraint, or a deformation energy of which the thin-plate spline energy is the canonical example (see [LA99] for a survey). Feldmar and Ayache's approach[FA96] resembles ours the most.

Feldmar and Ayache[FA96] perform a surface registration based on a distance measure including local geometrical properties of the surfaces. The surface registration is a collection of local affine registrations. The parameters of these registrations are spatially blurred so as to construct a smoothly varying registration. A difference to our approach is that we do not make a collection of local affine frames, but a global registration field. Secondly, and most importantly, we do not exploit any metric properties of the surfaces, but look for a globally simple registration field. This also creates a tendency to match points of similar geometry since the field otherwise must be more complex.

In principle, the geometry-constrained diffusion could also have been formulated as a geometry-constrained gradient descent in displacement energy [Boo96]. Hence, we here present a general technique for handling under-determined geometrical constraints in conjunction with variational approaches for non-rigid registration.

6.3 Geometry-constrained diffusion

A registration field may be diffused simply by diffusing the Cartesian components independently. The geometry-constrained diffusion is constructed such that it preserves certain fiducial mappings during the diffusion. Assume that the identification of some fiducial points, curves and/or surfaces is given *a priori*. In order to handle this partial geometrical knowledge in the general non-rigid registration problem, we propose geometry-constrained diffusion which in a precise sense simplifies the displacement field while preserving fiducial points, curves, and/or surfaces.

Given two images $I_1 : \mathbb{R}^3 \mapsto \mathbb{R}$ and $I_2 : \mathbb{R}^3 \mapsto \mathbb{R}$, we define the registration field $R : \mathbb{R}^3 \mapsto \mathbb{R}^3$. Along the same line we define the displacement field $D : \mathbb{R}^3 \mapsto \mathbb{R}^3$ such that $R(x) = x + D(x)$. We may then define:

Definition 1 (Displacement diffusion) *The diffusion of a displacement field $D : \mathbb{R}^3 \mapsto \mathbb{R}^3$ is an independent diffusion in each of its Cartesian components:*

$$\partial_t D = \triangle D$$

where the Laplacian, $\triangle = \frac{\partial^2}{\partial x^2} + \frac{\partial^2}{\partial y^2} + \frac{\partial^2}{\partial z^2}$, is applied independently in the x-, y-, and z-component of D.

The only difference between the registration and displacement field is the addition of a linear term. This term does not influence the diffusion so that registration diffusion is identical to the displacement diffusion.

This vector-valued diffusion has some obvious and important symmetries:

Proposition 1 *The displacement diffusion is invariant with respect to similarity transforms of any of the source or target images.*

Proof. The translational part of the similarity transform only adds a constant to the displacement field, and the diffusion is invariant to this. The displacement $y = D(x) + x$ is (up to a translation) similarly transformed such that $x' = s_1 R_1 x$ and $y' = s_2 R_2 y$ where R_1 and R_2 are 3×3 rotation matrices. Under $s_1 R_1$ the displacement is mapped to $D_1(x') = D(s_1^{-1} R_1^{-1} x') - x' + s_1^{-1} R_1^{-1} x'$. Applying $s_2 R_2$ also we find

$$D'(x') = s_2 R_2 [D(s_1^{-1} R_1^{-1} x') - x' + s_1^{-1} R_1^{-1} x']$$

The latter terms leave the diffusion unaltered since they only add terms of first order, and the diffusion depends only on terms of second order. Since the diffusion is linear, it is invariant to $s_2 R_2$. By re-mapping t the diffusion is known to be independent of similarity transforms of the base manifold. •

Applying the displacement diffusion without further constraints, it reaches a steady state which is an affine registration. This is easily seen since only linear functions are in the null-space of the diffusion equation.

In the case where the same geometrical structures have been identified in both images we wish to make certain that the diffusion of the displacement field reflects these structures. Assume that a surface $S_1 : \mathbb{R}^2 \mapsto \mathbb{R}^3$ in the source image is known to map on to the surface $S_2 : \mathbb{R}^2 \mapsto \mathbb{R}^3$ in the target image. We thus define

Definition 2 (Surface-constrained diffusion) *The surface constrained diffusion of $D : \mathbb{R}^3 \mapsto \mathbb{R}^3$ mapping $S_1 : \mathbb{R}^2 \mapsto \mathbb{R}^3$ onto $S_2 : \mathbb{R}^2 \mapsto \mathbb{R}^3$ is given by*

$$\partial_t D = \begin{cases} \triangle D - n_{S_2} \frac{n_{S_2} \cdot \triangle D}{\|n_{S_2}\|^2} & \text{if} \quad x \in S_1 \\ \triangle D & \text{if} \quad x \notin S_1 \end{cases}$$

where n_{S_2} is the unit surface normal of $S_2(D(x) + x)$.

This corresponds to solving the heat flow equation with certain boundary conditions. In this case, however, we do not keep the solution fixed at the surface, but allow points to travel along the surface. This is a dual approach to the geometry-driven curve and surface diffusion by Olver, Sapiro, and Tannenbaum [OST97] and others. We keep only the tangential part of the diffusion along the surface whereas they diffuse the geometry of the surface maintaining only the normal flow. The surface normal n_{S_2} may simply be obtained as a length normalization of $n_{S_1} + Jn_{S_1}$ where J is the Jacobean of D. In this way the formulation is no longer explicitly dependent on S_2. That is, given an initial (guess of the) displacement field and a surface in this source image to be preserved under diffusion, we may still apply the above equation without explicitly referencing to S_2.

Curve constraints and point constraints can be handled in a similar manner. For the curve problem, we project onto a curve by only taking the part of the diffusion which is along the curve tangent. Point constraints simply disregard the diffusion at these points. The three types of geometry-constrained diffusions may be combined in any fashion as long as the boundary conditions (the matches) do not contradict one another.

We make the following proposition:

Proposition 2 (Similarity Invariance (II)) *The geometry-constrained diffusion is invariant to similarity transforms of the source or target image.*

Proof. We have already shown that the unconstrained diffusion is similarity invariant. Both the surface normal and the curve tangent are also invariant under the similarity transform. •

We will conjecture that the geometry-constrained diffusion removes any fold in the initial displacement. This means that, the steady state solution to the geometry-constrained displacement diffusion creates an invertible mapping.

Conjecture 1 (Invertibility) *A geometry-constrained diffused displacement field induces a one-to-one mapping of* $\mathbb{R}^3$.

The steady state displacement field will be a homeomorphism assuming the above invertibility-conjecture is valid since the constrained diffused displacements are continuous. It will also be smooth except on the constrained objects where it will generally not be differentiable across object boundaries, but will be differentiable along smooth objects.

It is evident that the scheme is not symmetric in the images. This is due to the change in local metric by the non-linear displacement field. This makes the ordering of the two images important. It is, however, not obvious (to us) that the steady states will differ.

The geometry-constrained diffusion can be implemented simply by applying an numerical scheme for solving a space and time discretized version of the diffusion. It is well known that the diffusion equation is solved by Gaussian convolution. That is, an unconstrained diffusion can be updated an arbitrarily long time-step, by applying a Gaussian of appropriate size. The geometry-constrained diffusion cannot be solved directly in this manner due to the constrains. In general, the finite time step diffusion (Gaussian convolution) makes the displaced source surface diverge from the target surface, so that it must be back-projected to the target surface. The back-projection may be performed to the closest point on the target surface (see Fig. 6.1). In this way, the algorithm resembles the iterative closest point algorithm [BM92, Zha94] for rigid registrations.

6.4 Implementation

A time and space discretized solution the the geometry-constrained diffusion may be obtained by iterative Gaussian convolution and back-projecting the constrained surfaces.

The crux of the algorithm then becomes (see Fig. 6.2 for a flow chart):

1. **Initial displacement**. Construct an initial guess of the displacement field.

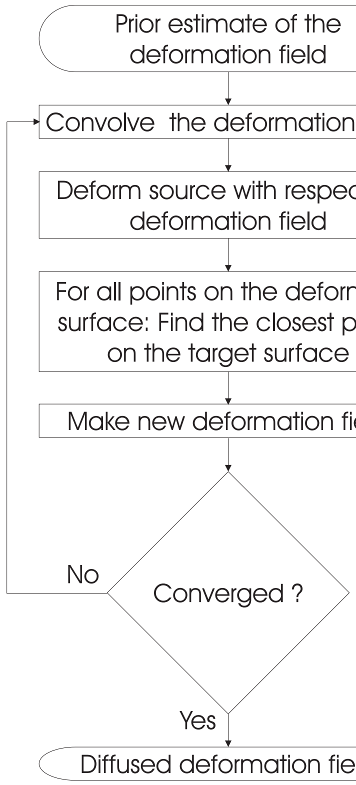

Figure 6.2: *Flow diagram for the diffusion algorithm. See section 6.4 for details.*

2. **Diffusion step**. Convolve the displacement field with a Gaussian kernel.

3. **Deform source**. Deform the source surface with respect to the displacement field.

4. **Matching (Projection onto the target surface)**. For all points on the deformed surface: find the closest point on the target surface.

5. **Update displacement field**. For all points on the deformed surface: change the displacements according to the match.

6. **Convergence**. Is the displacement field stable? If not, go to 2.

Some of the steps are explained in greater detail below.

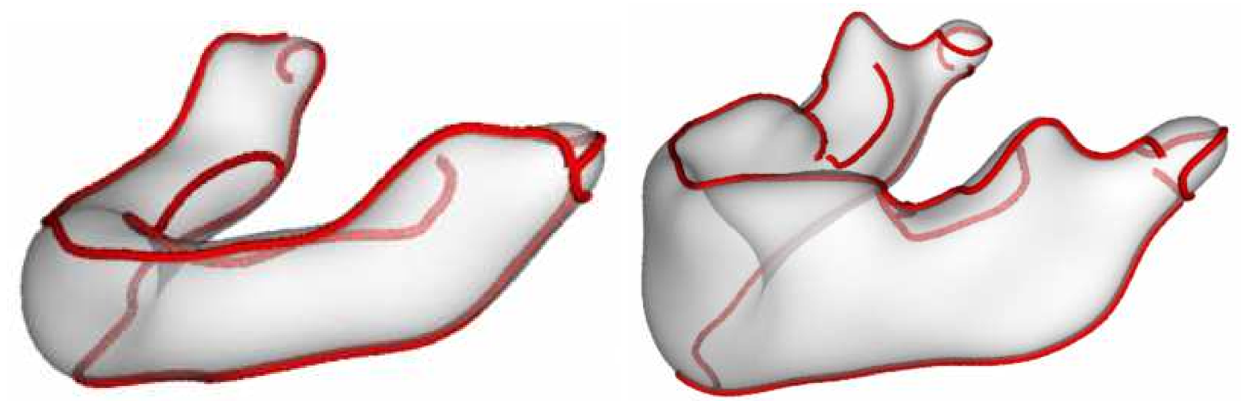

Figure 6.3: *Iso-surface and crest lines for a 3 (left) and 56 (right) month old mandible. The mandibles are Gaussian smoothed ($\sigma = 3mm$) in order to capture the higher scale features. The dimensions of the left and right mandibles are ($H\times W\times L$) $18\times 57\times 53mm$ and $31\times 79\times 79mm$, respectively. Surfaces are translucent.*

6.4.1 Diffusion step

We use the normalized Gaussian convolution [NA98]. For each of the Cartesian components of the displacement field, a Gaussian weighted average is constructed and divided with the sum of the weights. The standard deviation of the Gaussian σ is the only parameter in the numerical scheme (see section 6.4.4).

6.4.2 Matching

As in [Zha94] we use a 3D-tree for finding the closest point on the target surface. As reference points on the triangulated target surface we use the center of mass (CM point) for each triangle. The three corners of the triangles are used for calculating a plane. Using also the surface normals, we construct the following algorithm for finding the closest point: first, find the closest CM point using the kD-tree. Secondly, calculate the closest point on the surface as the intersection of the corresponding triangle-plane and the line given by the deformed point and the normal at the CM point.

6.4.3 Convergence

The diffusion is stopped when

$$\sum_{p_i} \|D_n(p_i) - D_{n-1}(p_i)\|^2 < \epsilon, \tag{6.1}$$

where p_i is the points on the source surface, D_n is the displacement in the nth-iteration, and ϵ is a user-chosen parameter. Alternatively, a fixed number of iterations could be chosen. 5-10 iterations is normally enough.

6.4.4 Choice of time step σ

The Gaussian kernel size, σ, is the only parameter in the diffusion algorithm. It determines the time discretization step. A too large value of σ, may tear apart the surface since we diffuse too far before back-projecting. This problem occurs in regions of high surface curvature. A too small value of σ also gives problems since we have chosen a fast but imprecise back-projection algorithm. The error in the back-projection introduces some artificial "bumps" in the path along which we diffuse. This may be overcome by a more precise back-projection algorithm or in practice by choosing σ sufficiently large (see Fig. 6.4-6.6). Identical solution are obtained for an interval of σ's.

In practice, we choose a small σ and increase it on the fly if folds persist.

6.5 Results

The method has been applied for registration of 31 mandibles from 6 different patient in a longitudinal growth study of the mandible. One mandible is chosen as the reference mandible. In order to propagate the landmarks, all mandibles are registered with the reference mandible and geometry-constrained diffusion is applied. The reference mandible is shown in Fig. 6.3-right. Fig. 6.3-left displays the target surface for all the subsequent figures, except for Fig. 6.6, which shows an example where the diffusion algorithm gives an erroneous result. The prior estimate of the displacement field is obtained by crest line matching [ANK98]. See Fig 6.7 for match between two sets of crest lines.

As seen in Fig. 6.4 (top images) the initial deformation contains folds. Applying the diffusion algorithm removes almost all the folds, but some persist. By increasing σ (see section 6.4.4), these are removed (Fig. 6.5). As seen in Fig. 6.6, too large a value of σ will eventually tear apart the surface.

Very convincingly, Fig. 6.8 shows that the crest lines are useful anatomical landmarks but only in areas where their topology stays fixed. Teeth eruption changes the crest line topology of the mandible. We see two lines before teeth eruption on top of the mandible (Fig. 6.3 - left image) but only one after teeth eruption (Fig. 6.3 - right image). A pure (crest) line matching algorithm is not able to handle such changes. Introducing the diffusion algorithm, the single crest line (the green line on top of the mandible in Fig. 6.8) is able to perform correctly - i.e., be registered in between the two other lines (the two red lines on top of the mandible in the same figure) as seen in Fig. 6.8-right.

The same phenomenon is seen on the bottom of the mandible. A single line on the young mandible is split in two on the older mandible.

6.6 Conclusion

In the present paper we have proposed an algorithm for finding the simplest displacement field, which is conjectured to be a homeomorphism (1-1 continuous mapping).

The geometry-constrained diffusion in this paper serves to simplify the non-rigid registration of surface models. The result is a much smoother displacement field. Volume registration is achieved by having more than one surface. It turns out that the algorithm itself is also very simple.

In theory, the method is parameter free, but implementations include parameters of space- and time-discretization and convergence threshold.

We are currently using the method for registering a longitudinal growth study of the mandible in order to extract more than 14000 homologous points which again are used for inference of the growth. In that study, applying the geometry-constrained diffusion results in a very significant increase in the explained variance by the growth model.

6.7 Acknowledgments

The work was supported by the Danish Technical Research Council, grant number 9600452 to Per Rønsholt Andresen. The authors also thank Sven Kreiborg (School of Dentistry, University of Copenhagen, Denmark) and Jeffrey L. Marsh (Plastic and Reconstructive Department for Pediatric Plastic Surgery, Washington University School of Medicine at St. Louis Children's Hospital, St. Louis, Missouri, USA) for the CT data. Also thanks to Bjarne K. Ersbøll (Technical University of Denmark) and Andy Dobrzeniecki (3D-Lab, Denmark) for comments on the manuscript. The Visualization Toolkit (`http://www.kitware.com`) was used for the visualizations.

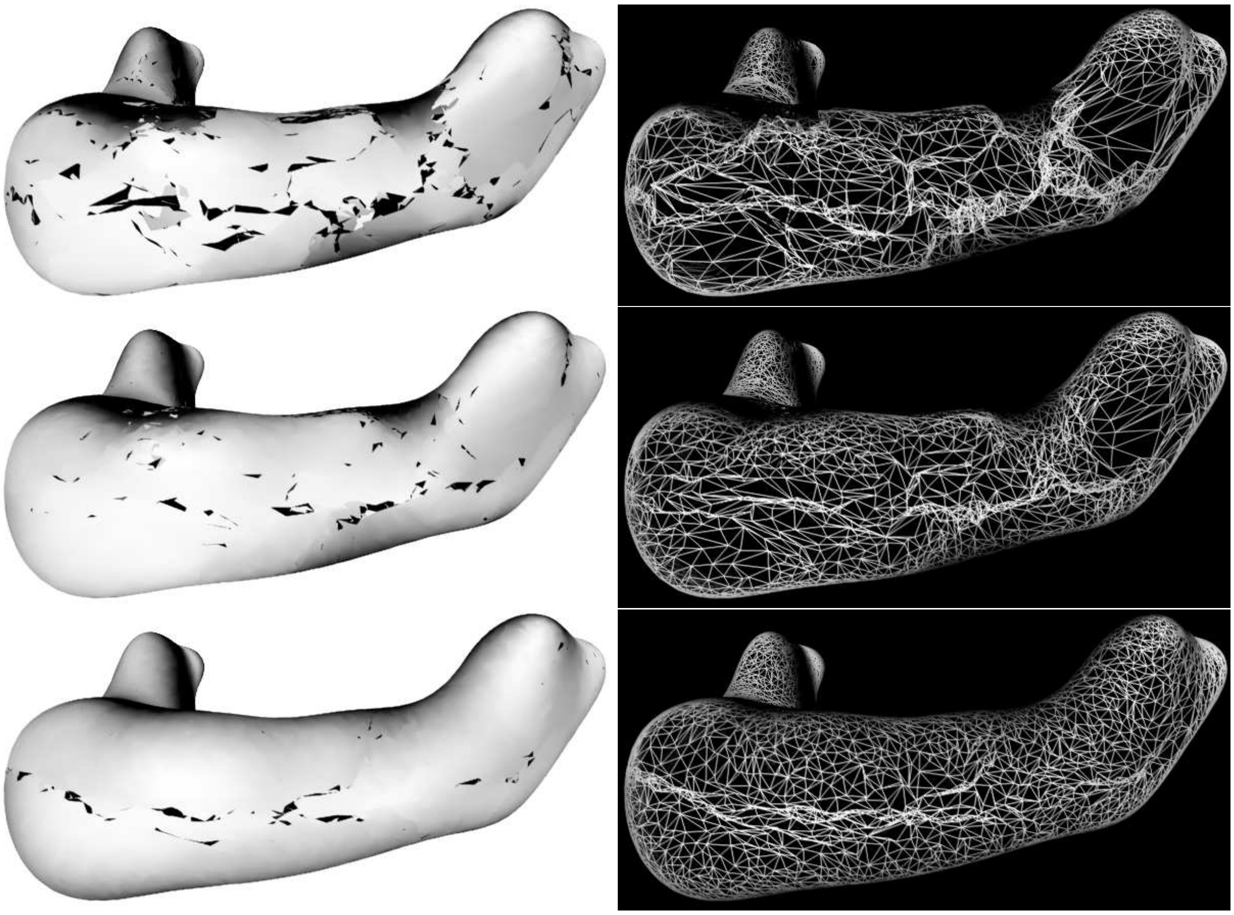

Figure 6.4: *Result of running the diffusion algorithm ($\sigma = 2mm$) on the displacement field. Deformation of the 56 month old mandible to the 3 month old mandible (see Fig. 6.3). The surface and wire-frame of the deformed surface are shown to the left and right respectively. The initial displacement, one iteration with the diffusion algorithm, and the last iteration are shown from top to bottom, respectively. The foldings are a result of the imperfect initial registration (extremal-mesh registration extended to the whole surface by Gaussian regularization as in [ANK98]). The final result is almost perfect, but some folds still exist, owing to the discretization of the surface and displacement field.*

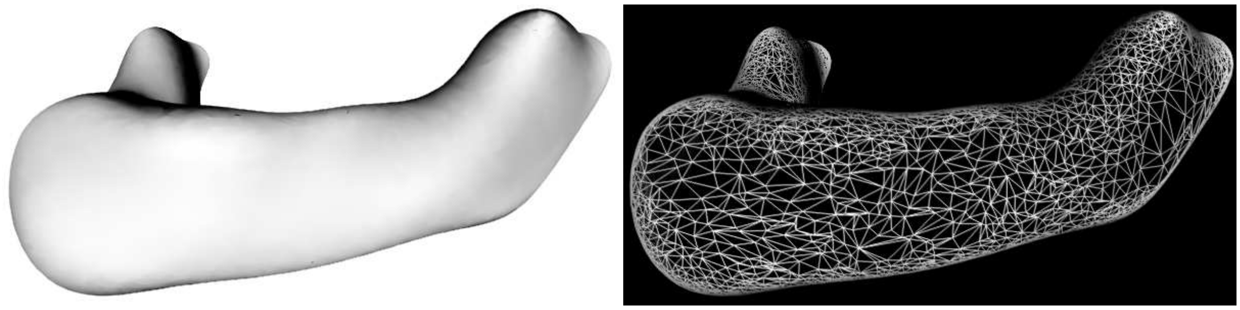

Figure 6.5: *Converged diffusion algorithm with a high value of σ ($\sigma = 10mm$). The surface and wire-frame of the deformed surface are shown to the left and right respectively. We have forced the displacement field to be more smooth, by increasing σ.*

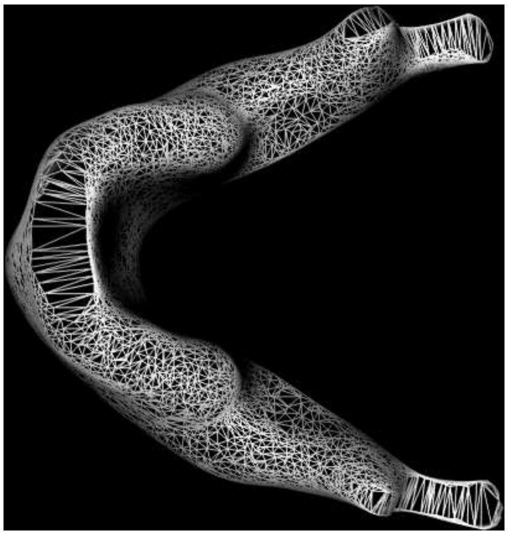

Figure 6.6: *The deformation vectors are moved too far away from the surface (The value of σ is too high) resulting in a wrong projection back onto the surface.*

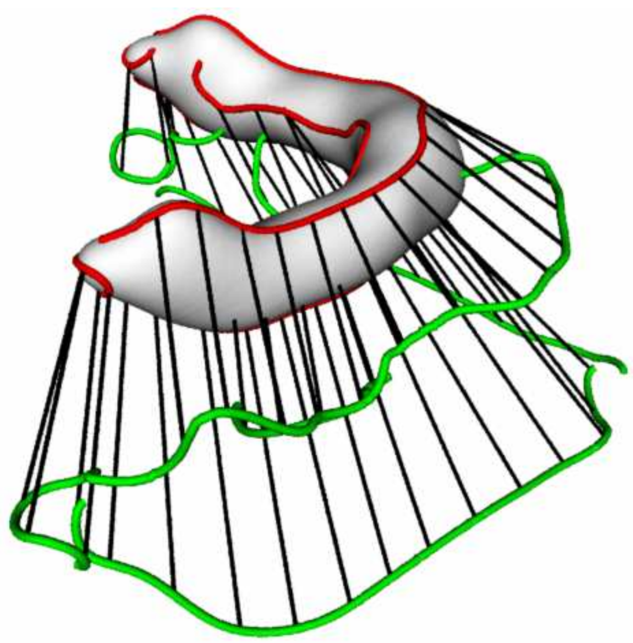

Figure 6.7: *Match (lines in black) between the two sets of crest lines (before applying the diffusion algorithm). The crest lines in red and green are from the mandibles shown in Fig. 6.3. Only every 11th link is shown for visual clarity. We see that the matches to a very good extent connect homologous points.*

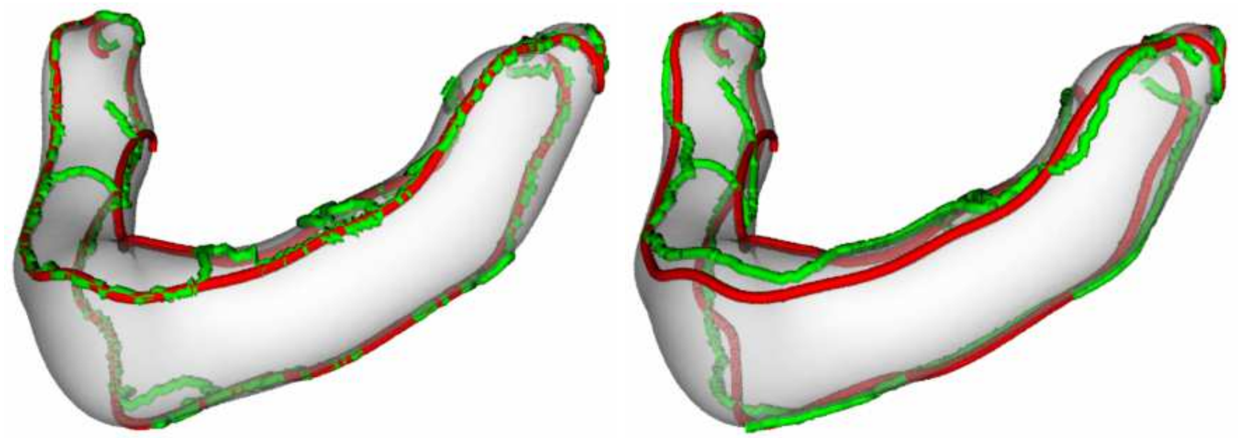

Figure 6.8: *Left and right images show the deformed (in green) and the original (in red) crest lines before and after applying the diffusion algorithm ($\sigma = 2mm$), respectively. In the initial registration crest lines are registered with crest lines. Where the topology does not change and away from umbilic points we see (almost) no movement of the green crest lines. Teeth eruption changes the topology on "top of the surface" (see Fig. 6.3) therefore the green crest lines move.*

Bibliography

[ANK98] P. R. Andresen, M. Nielsen, and S. Kreiborg. 4D shape-preserving modelling of bone growth. In *Medical Image Computing and Computer-Assisted Intervention - MICCAI'98*, volume 1496 of *Lecture Notes in Computer Science*, pages 710–719. Springer, 1998.

[BM92] P. J. Besl and N. D. McKay. A method for registration of 3-D shapes. *IEEE Transactions on Pattern Analysis and Machine Intelligence*, 14(2):239 – 255, 1992.

[Boo96] F. L. Bookstein. Landmark methods for forms without landmarks: localizing group differences in outline shape. In *Proceedings of the IEEE Workshop on Mathematical Methods in Biomedical Image Analysis*, pages 279–289, 1996.

[Boo97] F. L. Bookstein. Shape and the information in medical images: a decade of the morphometric synthesis. *Computer Vision and Image Understanding*, 66(2):97–118, 1997.

[FA96] J. Feldmar and N. Ayache. Rigid, affine and locally affine registration of free-form surfaces. *International Journal of Computer Vision*, 18(2):99–119, 1996.

[LA99] H. Lester and S. R. Arridge. A survey of hierarchical non-linear medical image registration. *Pattern Recognition*, 32:129–149, 1999.

[NA98] M. Nielsen and P. R. Andresen. Feature displacement interpolation. In *IEEE 1998 International Conference on Image Processing (ICIP'98)*, pages 208–212, 1998.

[OST97] P. J. Olver, G. Sapiro, and A. Tannenbaum. Invariant geometric evolutions of surfaces and volumetric smoothing. *SIAM Journal on Applied Mathematics*, 57(1):176–194, 1997.

[Thi96] J.-P. Thirion. The extremal mesh and the understanding of 3D surfaces. *International Journal of Computer Vision*, 19(2):115–128, 1996.

[Zha94] Z. Zhang. Iterative point matching for registration of free-form curves and surfaces. *International Journal of Computer Vision*, 13(2):147–176, 1994.

Chapter 7

Surface-bounded Growth Modeling Applied to Human Mandibles

Surface-bounded Growth Modeling Applied to Human Mandibles[1]

Per Rønsholt Andresen, Fred L. Bookstein, Knut Conradsen,

Bjarne Kjær Ersbøll, Jeffrey L. Marsh, and Sven Kreiborg

Abstract

From a set of longitudinal three dimensional scannings of the same anatomical structure, we have accurately modeled the temporal shape and size changes using a linear shape model. On a total of 31 CT-scans of the mandible from 6 patients, 14851 semi-landmarks are found automatically using shape features and a new algorithm called *geometry-constrained diffusion*. The semi-landmarks are mapped into Procrustes space. Principal component analysis extracts a one dimensional subspace, which is used to construct a linear growth model. The worst case mean modeling error in a cross validation study is 3.7 mm. It occurs when modeling the shape of a 12 years old mandible based on the 3 month old scan. When using successively more recent scans as basis for the model the error drops to 2.0 mm for the 11 years old scan.

Keywords: geometry-constrained diffusion, principal component analysis, non-rigid shape-preserving registration, morphometrics

7.1 Introduction

Pediatric craniofacial surgeons need insights into expected facial growth. This paper is concerned with the mandible, a particularly complex bony structure both in its shape and in its growth process, as two sets of teeth erupt asynchronously while the direction of the condylar process changes by a considerable angle.

Our data set here comprises 31 mandibular surfaces extracted from CT scans of a total of six children diagnosed with Apert syndrome. The analysis falls under two major headings: the representation of the set of mandibular surfaces by one vector of 14851 points that can be considered to be semi-landmarks (to correspond under a reasonable model of diffeomorphism); and the summary of these 31 point sets in linear statistical spaces of surprisingly low dimension, affording the possibility of cross validated growth prediction to an accuracy of 3.7 mm of mean error over intervals of 141 month.

The organization of the remainder of this text is as follows. Section 7.2 sets the stage for our algorithm by reviewing the literature of nonrigid registration by deformable models. Section 7.3 introduces the patients to which we have access, their CT images, and the mechanism by which we produced the 31 mandibular surfaces of the data set. Section 7.4 describes the initialization of our diffeomorphism by detection and matching of crest lines, and Section 7.5 shows how we proceed to a full surface-constrained diffusion. In Sections 7.6 and 7.7, the (31-1)-dimensional sample subspace of the full (3*14851-7)-dimensional space of semi-landmark shape is subjected to certain conventional multivariate biometric analyses that yield powerful predictors of unobserved (future) form. We assess their accuracy using measures of mean and standard deviation surface-to-surface discrepancy. Section 7.8 is a retrospect over all these tactics, emphasizing the surprising power of the diffusion methodology to uncover commonalities in the six independent growth processes of this sample. We close with a plea for corresponding studies of normative samples.

7.2 Related work

The literature treating registration methods is very extensive (e.g. [LA99, MV98] for surveys). This section therefore mainly concentrates on the literature covering both registration and deformable models (for reviews, e.g. [JZDJ98, MT96]) or morphometrics (e.g. [MCL$^+$96, Boo97]). We will accentuate the registration method of Feldmar and Ayache [FA96] as it resembles the geometry-constrained diffusion method [AN99] most. Feldmar and Ayache [FA96] perform a surface registration based on a distance measure which includes the local geometrical properties of the surfaces. The surface registration is a collection of local affine registrations. The parameters of these registrations are spatially blurred so as to construct a smoothly varying registration. Geometry-constrained diffusion (Section 7.5) does not make a collection of local affine frames, but a global registration field. Secondly, and most importantly, we do not exploit any metric properties of the surfaces, but look for a globally simple registration field. This also creates a tendency to match points of similar geometry since the field otherwise must be more complex.

Deformable models have been widely studied [JZDJ98, MT96]. When using landmarks for making the correspondence between objects one main drawback is the manual location of them. A lot of researchers have worked on this. Bookstein has reported a method were the semi-landmarks are placed on contours automatically [Boo96]. Note, a landmark is a point that can be identified by verbal characterization on the single case [Boo91]. Semi-landmarks are points that do not have names. but correspond across all the cases, so one can carry out statistics on them [Boo96].

Fleute and Lavallée [FL98] extrapolate a small number of range data to obtain a complete surface representation. Principal Component Analysis (PCA) is used to reduce the dimensionality. Data sets are registered together using an elastic registration method of Szeliski and Lavallée [SL96] based on octree-splines. Szeliski and Lavallée [SL96] perform a least squares minimization of the distances between a sparse and unorganized set of points and a dense set used to build a 3D octree-spline distance map. The result is a smooth deformation field.

A registration technique based on thin-plate splines that takes landmark errors into account is reported by [Roh98]. The semi-landmarks are located semi-automatic or manually.

The present work has been greatly inspired by the seminal work of Cootes and colleagues ([CT99] for an overview) and Dean et al. [DHBS99] (see below). Previous, manually detected landmarks have been used for Cootes and colleagues' analysis [CT99]. Automatic landmarking for both 2D and 3D is reviewed in [CT99]. Principal components are calculated from the Procrustes analysis and an active shape model is made. The deformation of the active shape model is restricted by the principal components. For segmentation, gray level information near the object boundaries is also modeled.

Kelemen et al. [KSG98] have used the same method as in [CT99], but in order to automate the landmark generation, Fourier-descriptors [SD96, BGK95] are found very powerful. Restrictions on the topology of the surfaces are the main drawback when using Fourier-descriptors.

In the present paper the registration method of Subsol et al. [STA98] gives the object correspondence (Section 7.4). Crest lines [Thi96] are registered together taking into account the constraints inferred by lines and an heuristic algorithm based on the Iterative Closest-Point (ICP) algorithm [BM92].

Grenander and Miller [GM98] have formalized the Brown/Washington University model of anatomy in which anatomies are represented as deformable templates, collections of 0, 1, 2, 3-dimensional manifolds. They have three principal components in computational anatomy: 1) computation of large deformation maps. Joshi [Jos97] have proved that the resulting mapping between given anatomies is a diffeomorphism. 2) computation of empirical probability laws which represent anatomical variation reflected by the observed population. 3) computational inference on population and disease testing and classification.

Dean et al. [DHBS99] analyze plain head x-ray stereo-pairs[2] from 32 individuals (16 males and 16 females) ages 3-18 years old. The objective is to investigate 1) which 3D landmarks could be collected with high precision; 2) to identify ontogenetic trends in landmark configuration shape change; and 3) to detect patterns of sexual dimorphism. The 32 landmarks are transformed in to two Procrustes shape spaces (one for each gender). Relative warps are then used to search for trends in ontogenetic shape change. It is interesting that the result of the analysis is almost identical to the present work even though the 32 landmarks are placed mostly off the mandible.

We are not aware of any other growth studies where longitudinal 3D acquisitions from humans have been used for growth modeling except in [Sub95, BNGK97, ANK98] where the growth was modeled for one patient[3]. Subsol [Sub95] modeled the craniofacial growth using a linear model between a set of the controlling points. Bro-Nielsen et al. [BNGK97] used a non-rigid registration method to model the growth of the mandible. The method was a surface interpolation which did not preserve the mandibular shape, e.g. the condyles disappeared for intermediate interpolated time instances. Andresen et al. [ANK98] used the same object registration technique as in Section 7.4 to register the mandibles. A second order polynomial was used to interpolate the longitudinal displacement. Unfortunately the modeled mandible shrinks when trying to extrapolate. This is due to the chosen polynomial model which is not well suited for modeling the mandibular growth.

[2] frontal and lateral head x-rays.

[3] All three studies used the scannings of patient 6 (Table 7.1).

7.3 Data material

The data consisted of Computerized Tomography (CT) scans of six subjects with Apert syndrome, 3 Danish (patient 6) and 28 American (patient 1-5) scans; four males and two females. All scannings were performed using Siemens scanners and employing the same protocol. The subjects were scanned for diagnostic, treatment planning, and follow-up purposes at the craniofacial clinics. The individual subjects were scanned between three and seven times, and age range is 1 month to 12 years (Table 7.1).

A Previous 2D roentgencephalometric study has shown that the mandible in Apert syndrome has relatively normal morphology except for some adaptive changes [KAC99].

The mandibular data for the two sexes are pooled in the present study, since all scannings were carried out before puberty, and because the total sample size is relative small.

The mandibles are extracted from the CT scans by thresholding and manual segmentation (the areas around the condyles were manually segmented). Holes inside the object are filled and lastly the mandibles are trilinearly resliced to 0.5 mm cubic voxels (originally 2 mm slices and 0.26 - 1.0 mm voxels in the plane).

7.4 Registration: object correspondence

In order to establish object correspondence, we search for features that match areas with equivalent morphology. Since the topology is not changed dramatically for the mandible when growing, features reflecting the "stable" geometry are used. The local shape of a surface is totally characterized by the principal curvatures k_1, k_2 ($k_1 > k_2$) and their derivatives in the coordinate system defined by the principal directions (t_1, t_2) [dC76]. A list of some derived shape features is found in

Patient number	Scan number	Sex	Age in month
1	1	M	3
	2		16
	3		21
	4		23
	5		34
2	1	M	1
	2		7
	3		23
	4		54
	(5)		56
	6		60
	7		72
3	1	M	1
	2		5
	3		17
	4		32
	5		36

Patient number	Mandible number	Sex	Age in month
4	1	F	3
	2		27
	3		46
	4		62
	5		131
	6		132
	7		144
5	1	M	3
	2		4
	3		21
	4		72
6	1	F	9
	2		21
	3		84

Table 7.1: *The table shows the data material used in the present study. Each of the six groups (between the horizontal lines) represents CT scans from a single Apert patient (three to seven scans of each patient). CT scan for patient 2 scan #5 is the reference mandible from which all the semi-landmark points are propagated.*

Figure 7.1: *The crest lines on the three Gaussian smoothed (kernel size, $\sigma = 3mm$) mandibles at 9 month (left), 21 month (middle), and 7 years old (right). Mandibles are from patient 6, scan #1, #2, and #3, respectively). The surfaces are translucent.*

[ANK98].

We work with the extraction and matching of ridge lines [Koe84, Thi96, ANK98]. Satisfactory results are obtained, by making a matching which only accepts good matches. The crest lines on three mandibles are seen in Figure 7.1.

The ridge lines (or extremal mesh) are partitioned into four types corresponding to maximum or minimum in k_1 and k_2, respectively. As features we only consider the lines with maximally k_1 (crest lines) and maximally k_2 (here, called k_2-max lines) in the extremal mesh [Thi96]. The overall framework follows the ideas originally proposed in [STA98] and also used in [ANK98]. First, the crest lines and k_2-max lines for each dataset are extracted at a high scale, in order to get the more global features (Figure 7.1). The crest lines are registered and an initial deformation field is calculated by adaptive Gaussian smoothing [NA98]. The k_2-max lines are then deformed according to the initial deformation field and subsequently registered. From the two sets of matches (one from the crest lines, the other from the k_2-max lines) a combined deformation field is calculated. Another iteration is done at a fine scale, but using the high scale deformation field as initial displacement. The resulting field is used as an initial guess in the point matching algorithm (Section 7.5).

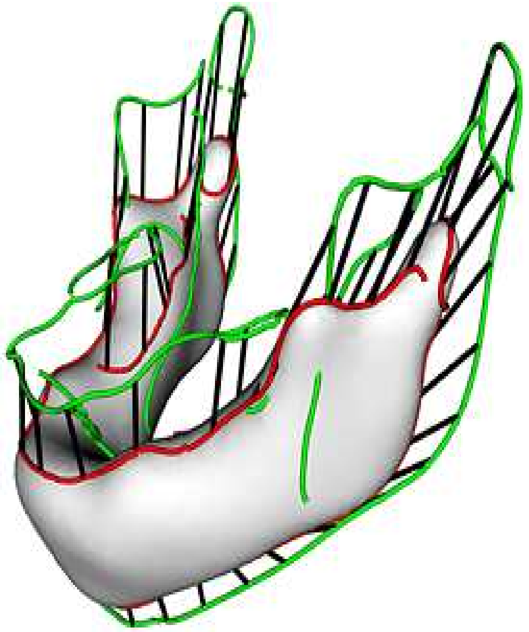

Figure 7.2: *Matches (lines in black) between two sets of crest lines at scale 3. The crest lines on the 21 month and 7 years old mandible (patient 6, scan #2 and #3, respectively) are red and green, respectively. For visual clarity only every eighth match is shown.*

The steps in the registration are always the same. First moment-registration, then two first order polynomial deformations, followed by two second order polynomial deformations. Finally, a totally non-rigid deformation (all points on the lines move freely) is applied (see [STA98] for details).

7.5 Registration: point correspondence

A detailed description of the algorithm used in this section may be found in [AN99]. The main idea of the algorithm is Gaussian smoothing[4] the Cartesian components of the displacement field independently. In general, this means that the links are moved away from the surface (Figure 7.3 - middle image). Then, they are projected back to the closest point on the surface (Figure 7.3 - right image). In this way, our algorithm resembles the iterative closest point algorithm [BM92, Zha94] for

[4] with re-normalization so the filter weights become unity [NA98].

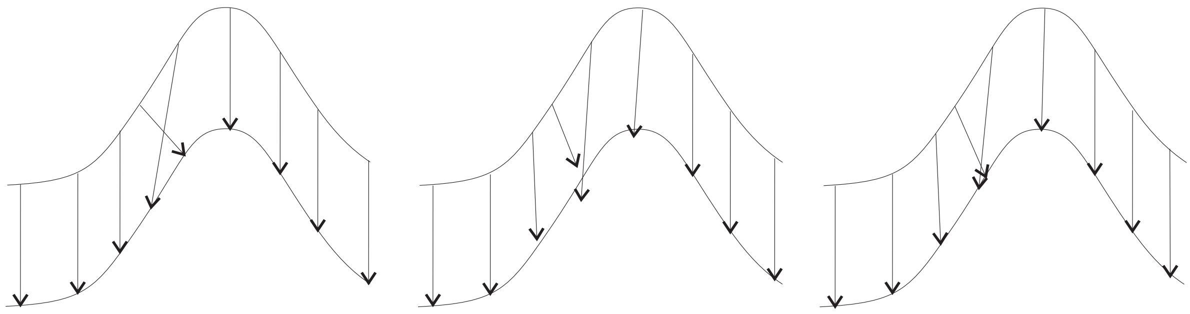

Figure 7.3: *The images show schematically how the diffusion algorithm works on the deformation field. The Cartesian components of the initial deformation field (arrows in the left image) are Gaussian smoothed. Some of the links have now diverged from the surface (middle image) and must be projected back on to the surface (right image). The fold is removed by repeating the steps until the field does not change.*

rigid registrations. The steps are repeated until the field is converged to steady state. Figures 7.6 and 7.7 show how the diffusion algorithm works on the displacement field (see Figure 7.5 for images of the mandibles).

The crux of the algorithm then becomes (see Fig. 7.4 for a flow chart):

1. **Initial displacement**. Construct an initial guess of the displacement field.
2. **Diffusion step**. Convolve the displacement field with a Gaussian kernel of size σ_D.
3. **Deform source**. Deform the source surface with respect to the displacement field.
4. **Matching (Projection onto the target surface)**. For all points on the deformed surface: find the closest point on the target surface.
5. **Update displacement field**. For all points on the deformed surface: change the displacements according to the match.
6. **Convergence**. Is the displacement field stable? If not, go to 2.

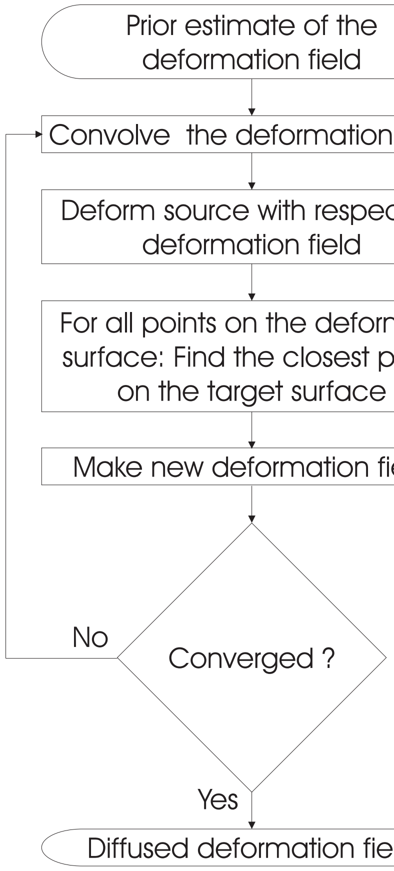

Figure 7.4: *Flow diagram for the diffusion algorithm. See Section 7.5 for details.*

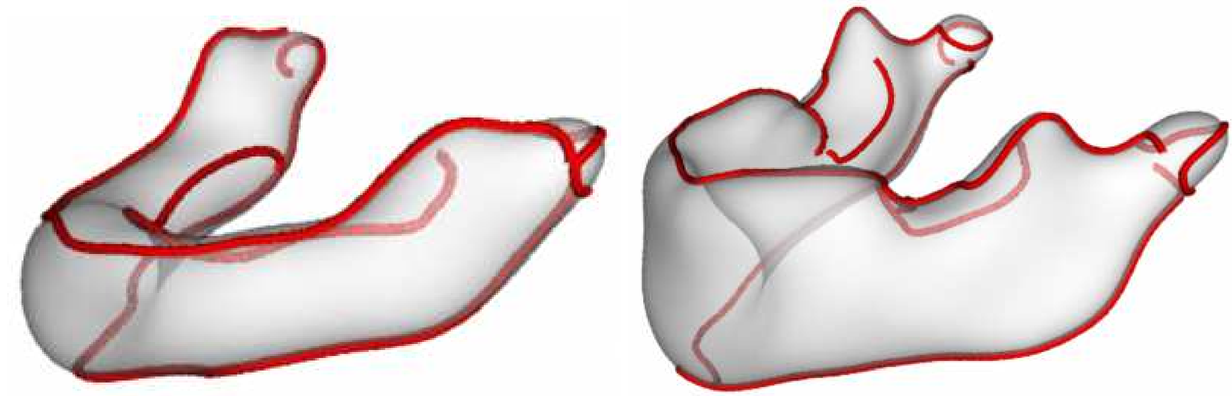

Figure 7.5: *Iso-surface and crest lines for a 3 (left) and 56 (right) month old mandibles (patient 1, scan #1 and patient 2, scan #5), respectively. The mandibles are Gaussian smoothed ($\sigma = 3mm$) in order to capture the higher scale features. The dimensions of the left and right mandibles are ($H\times W\times L$) $18\times 57\times 53$ mm and $31\times 79\times 79$ mm, respectively. Surfaces are translucent.*

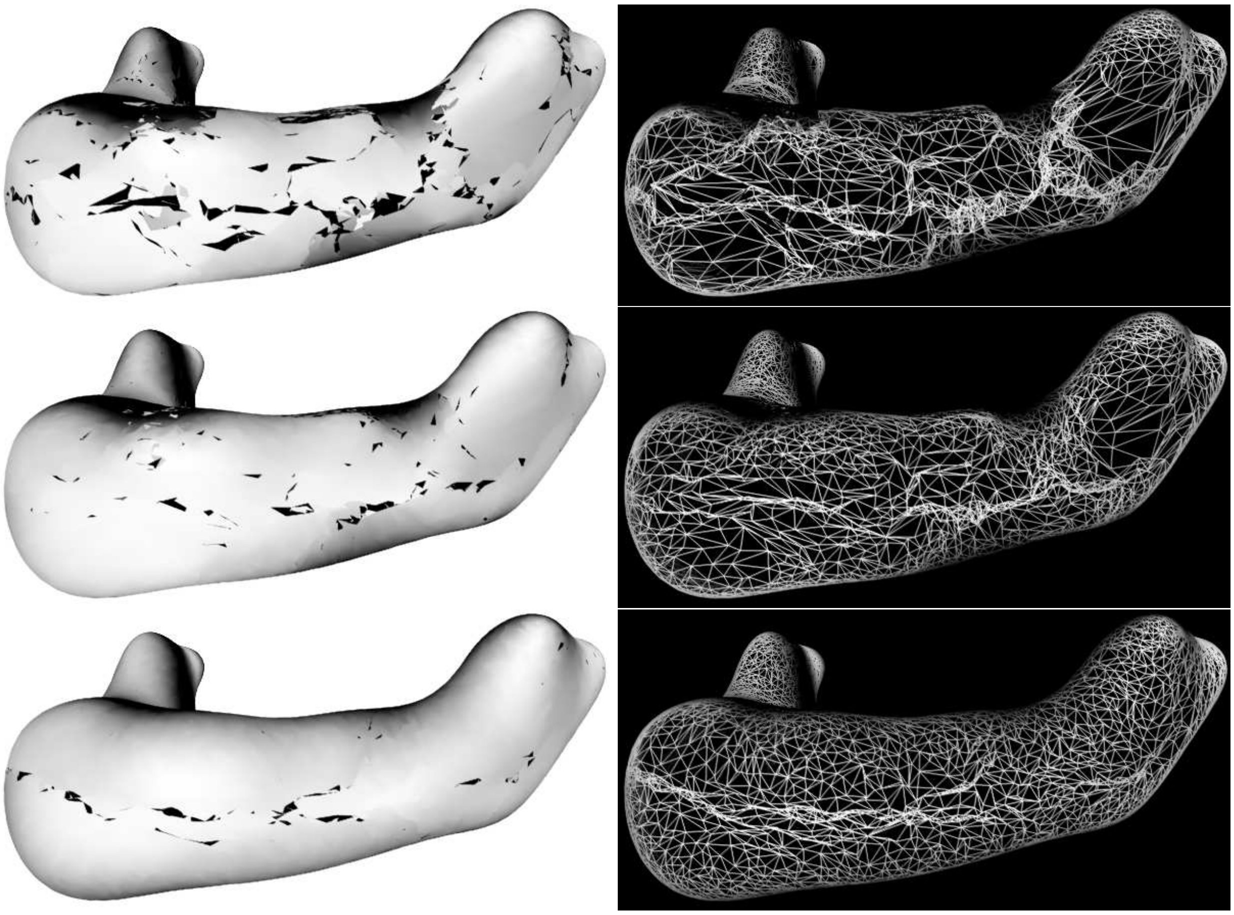

Figure 7.6: *Result of running the diffusion algorithm ($\sigma_D = 2mm$) on the displacement field. The surface shows the deformed 56 month old mandible to the 3 month old mandible (Figure 7.5). The surface and wire-frame of the deformed surface are shown to the left and right, respectively. The initial displacement, one iteration with the diffusion algorithm, and the last iteration are shown from top to bottom, respectively. The foldings are a result of the imperfect initial registration (the extremal-mesh registration is extended to the whole surface by Gaussian regularization [ANK98]). The final result is almost perfect, but some folds still exist, owing to the discretization of the surface and displacement field. The last folds are removed in Figure 7.7 by increasing σ_D.*

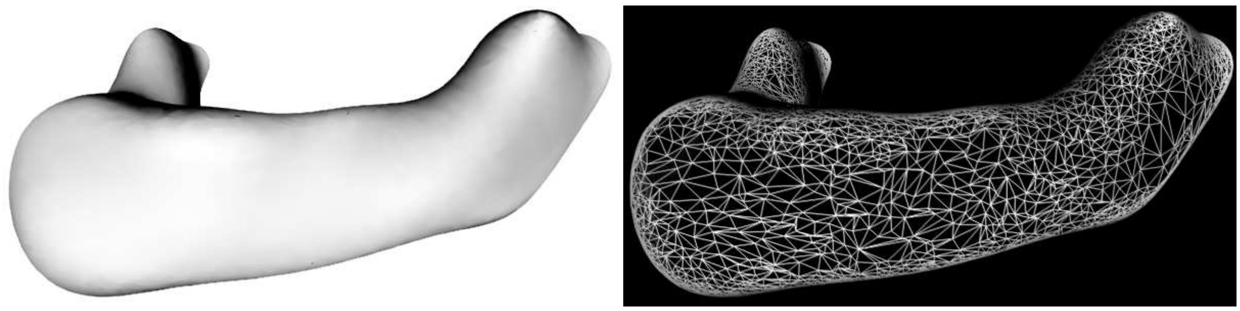

Figure 7.7: *Converged diffusion algorithm with a high value of σ_D ($\sigma_D = 10mm$). The surface and wire-frame of the deformed surface are shown to the left and right respectively. The displacement field is forced to be more smooth, by increasing σ_D.*

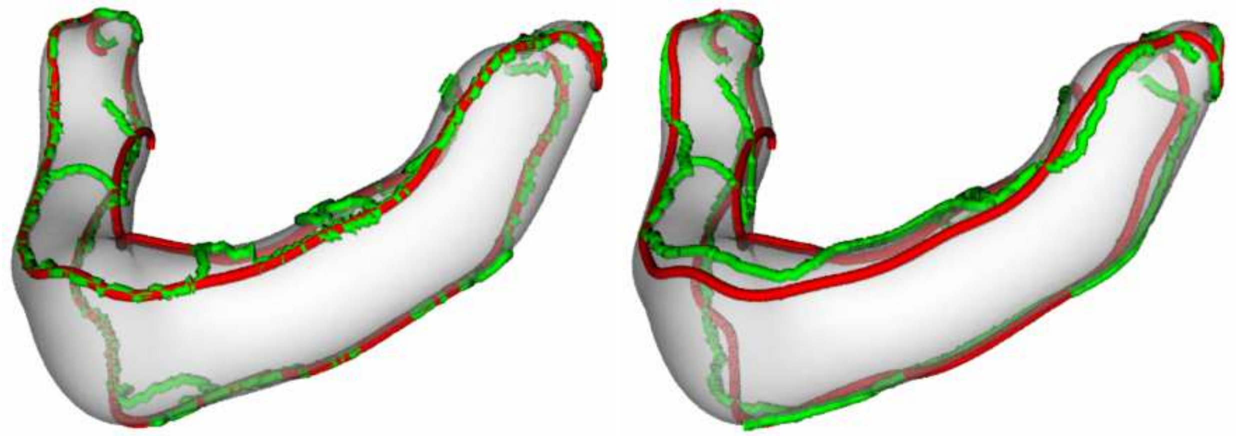

Figure 7.8: *Left and right images show the deformed (in green) and the original (in red) crest lines before and after applying the diffusion algorithm ($\sigma_D = 2mm$), respectively. In the initial registration crest lines are registered with crest lines. Where the topology does not change and away from umbilic points, (almost) no movement of the green crest lines are seen. Erupting teeth change the topology on the "top of the surface" (see Figure 7.5), therefore the green crest lines move in this area.*

Some of the steps are explained in greater detail below.

7.5.1 Regularization

We use the normalized Gaussian convolution [NA98]. For each of the Cartesian components of the displacement field, a Gaussian weighted average is constructed and divided with the sum of the weights. The standard deviation of the Gaussian σ_D is the only parameter in the numerical scheme. It regulates the time steps between projections onto the surface. For simple surfaces it may be large. For surfaces including regions of high curvature σ_D must be smaller in order not to tear the surface apart (see Figures 7.6, 7.7, and 7.9). Theoretically, small values of σ_D should yield the same result as larger values of σ_D (when the surface is not teared apart), because of the additive nature of the Gaussian smoothing, but the discretization of the displacement field and surface means that the algorithm could hang before satisfactory results[5] are obtained. A good approach is:

1. Set σ_D to a small number, say 1.
2. Run the algorithm.
3. If the result is satisfactory then stop.
4. Increase σ_D, say $\sigma_D = \sigma_D + 1$, go to 2.

7.5.2 Matching

As in [Zha94] kD-tree is used for finding the closest point on the target surface. As reference points on the triangulated target surface we use the center of mass (CM point) for each triangle.

[5] in the present study, a satisfactory result is a surface without folds.

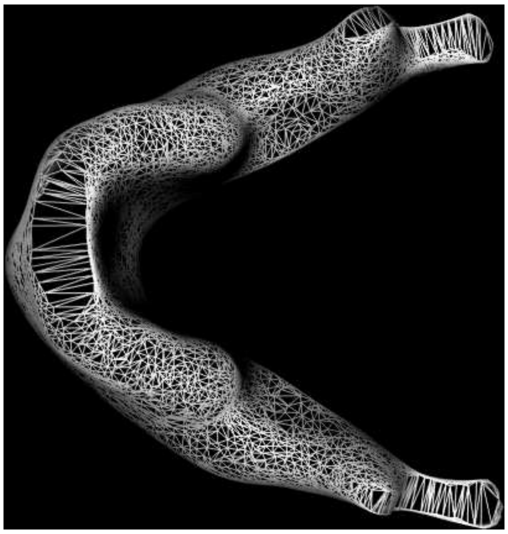

Figure 7.9: *The deformation vectors are moved too far away from the surface (The value of σ_D is too high) resulting in a wrong projection back onto the surface.*

The triangle's three corners are used for calculating a plane. Using also the surface normals, we construct the following algorithm is constructed for finding the closest point: first, find the closest CM point using the kD-tree. Secondly, calculate the closest point on the surface as the intersection of the corresponding triangle-plane and the line given by the deformed point and the normal at the CM point.

7.5.3 Convergence

The diffusion is stopped when

$$\sum_{p_i} \|D_n(p_i) - D_{n-1}(p_i)\|^2 < \epsilon, \tag{7.1}$$

where p_i is the points on the source surface, D_n is the displacement in the nth-iteration, and ϵ is a user-chosen parameter. Alternatively, a fixed number of iterations could be chosen. 5-10 iterations is normally enough.

7.6 Statistical description: geometric morphometric analysis

The shapes (here mandibles) are aligned into a common coordinate frame by Procrustes Analysis [Goo91, Boo97]. A simple iterative approach is as follows ($\mathbf{X}_i$ is the $k \times 3$ matrix for the k 3D-semi-landmarks in shape i. $\bar{\mathbf{X}}$ is the mean shape):

1. The center of mass (the centroid) for each shape is translated to the origin.

2. The *centroid size* for each shape is scaled to 1. When the centroid is $\mathbf{0}$, the centroid size equals the Frobenius norm. The centroid size is also the square root of the summed squared distance between the landmarks and their centroid (here the origin). $\|\mathbf{X}_i\|_{fro} = \sqrt{\text{trace}(\mathbf{X}_i^T \mathbf{X}_i)} = 1$.

3. Use one shape as the initial estimate for the mean shape $\bar{\mathbf{X}}$.

4. Align all shapes with the mean shape. The optimal rotation required to superimpose $\mathbf{X}_i$ on $\bar{\mathbf{X}}$ is VU^T (a 3×3 matrix), where UDV^T is the singular-value decomposition of $\bar{\mathbf{X}}^T \mathbf{X}_i$ with all elements of D positive.

5. Re-estimate the mean shape as the average of the fitted locations landmark by landmark. $\bar{\mathbf{X}} = \frac{1}{n} \sum_{i=1}^{n} \mathbf{X}_i$.

6. Return to 4 until converged. Convergence is reached when the mean shape only changes very little, usually after a few iterations.

We are not using the standard Procrustes space for the growth modeling, but the space where the mean shape for each patient has been subtracted. Having all the patients aligned, the mean shapes are calculated as (for indices cf. Table 7.1):

$$\begin{aligned}\bar{\mathbf{X}}_{\text{patient 1}} &= \frac{1}{5}\sum_{i=1}^{5}\mathbf{X}_{1,i}\\ &\vdots \\ \bar{\mathbf{X}}_{\text{patient 6}} &= \frac{1}{3}\sum_{i=1}^{3}\mathbf{X}_{6,i}\end{aligned} \tag{7.2}$$

Let $\tilde{\mathbf{X}}_{p,i}$ be the mandible where the mean mandible is subtracted:

$$\tilde{\mathbf{X}}_{p,i} = \mathbf{X}_{p,i} - \begin{cases} \bar{\mathbf{X}}_{\text{patient 1}} & p = 1,\ i = 1,\ldots,5 \\ & \vdots \\ \bar{\mathbf{X}}_{\text{patient 6}} & p = 6,\ i = 1,\ldots,3 \end{cases} \tag{7.3}$$

$\tilde{\mathbf{X}}_{p,i}$ is rearranged in to a column vector ($\dim(\tilde{\mathbf{x}}_{p,i}) = 3k \times 1$) called $\tilde{\mathbf{x}}_{p,i}$. Let

$$\mathbf{D} = ((\tilde{\mathbf{x}}_{1,1} - \hat{\tilde{\mathbf{x}}})|\ldots|(\tilde{\mathbf{x}}_{6,3} - \hat{\tilde{\mathbf{x}}})), \tag{7.4}$$

were $\hat{\tilde{\mathbf{x}}}$ is the grand mean

$$\hat{\tilde{\mathbf{x}}} = \frac{1}{n}\sum \tilde{\mathbf{x}}_{p,i},$$

and $n = 31$ is number of data sets.

The covariance matrix can be written ($\mathbf{D}^T$ is the transpose of $\mathbf{D}$) as

$$\mathbf{S} = \frac{1}{n-1}\mathbf{D}\mathbf{D}^T\,,\ \dim(\mathbf{S}) = k \times k \tag{7.5}$$

When $k > n$ (here $k = 14851$ and $n = 31$), it is more feasible to calculate the PC from the matrix

$$\mathbf{T} = \frac{1}{n-1}\mathbf{D}^T\mathbf{D}\,,\ \dim(\mathbf{T}) = n \times n \tag{7.6}$$

Let $\tilde{\mathbf{e}}_j$ be the eigenvector of $\mathbf{T}$ with corresponding eigenvalue λ_j, sorted in descending order. It follows from Eckart-Young's theorem [Joh63] that the n vectors

$$\mathbf{e}_j = \frac{1}{\sqrt{\lambda_j}}\mathbf{D}\tilde{\mathbf{e}}_j \tag{7.7}$$

are all eigenvectors of $\mathbf{S}$ with corresponding eigenvalues λ_j. The last $k-n$ eigenvectors are all zero.

$\sigma = 3, k = 9087$						$\sigma = 1, k = 14851$		
no diffusion			diffusion			diffusion		
$\hat{\lambda}_i * 10^5$	p.var	c.p.var	$\hat{\lambda}_i * 10^5$	p.var	c.p.var	$\hat{\lambda}_i * 10^5$	p.var	c.p.var
0.3134	45.19	45.19	0.3107	67.59	67.59	0.1897	62.18	62.18
0.0496	7.15	52.35	0.0294	6.39	73.98	0.0222	7.27	69.45
0.0415	5.99	58.33	0.0233	5.06	79.04	0.0164	5.33	74.78
0.0373	5.39	63.72	0.0197	4.28	83.33	0.0151	4.95	79.73

Table 7.2: *Principal component analysis of the landmark data (see text for further explanation). The table shows the first four Eigenvalues, $\lambda_i, i = 1, \cdots, 4$.* "p.var" *and* "c.p.var" *are the percentage and cumulated percentage of the total variation. k is the number of semi-landmarks.* "no diffusion" *and* "diffusion" *means before and after applying the diffusion algorithm (Section 7.5). The diffusion algorithm increases the percentage of the total variation in the first eigenvalue by as much as $67.59\% - 45.19\% = 22.40\%$. Decreasing $\sigma = 1$ (size of the Gaussian smoothing) results in a more locally changing topology which is "harder to capture" in a few eigenvalues, hence* "c.p.var" *also decreases as expected.*

7.7 Shape evaluation and prediction

Table 7.2 shows the result of the principal component analysis.

Any summary of an ostensibly homogeneous sample of biological material, in this case observed growth in six children with the same diagnosis of synostosis, is persuasive to the extent that that categorization "explains" the quantifications: the extent to which the extracted measurements are homogeneous over the class. From Figure 7.10 it is clear that the six cases span an angular range of nearly 90 degrees in this projection; after diffusion, the alignment is far tighter. As shown in Table 7.2, there is far less variation around the common direction of these growth trajectories after diffusion than before (68% vs. 45%).

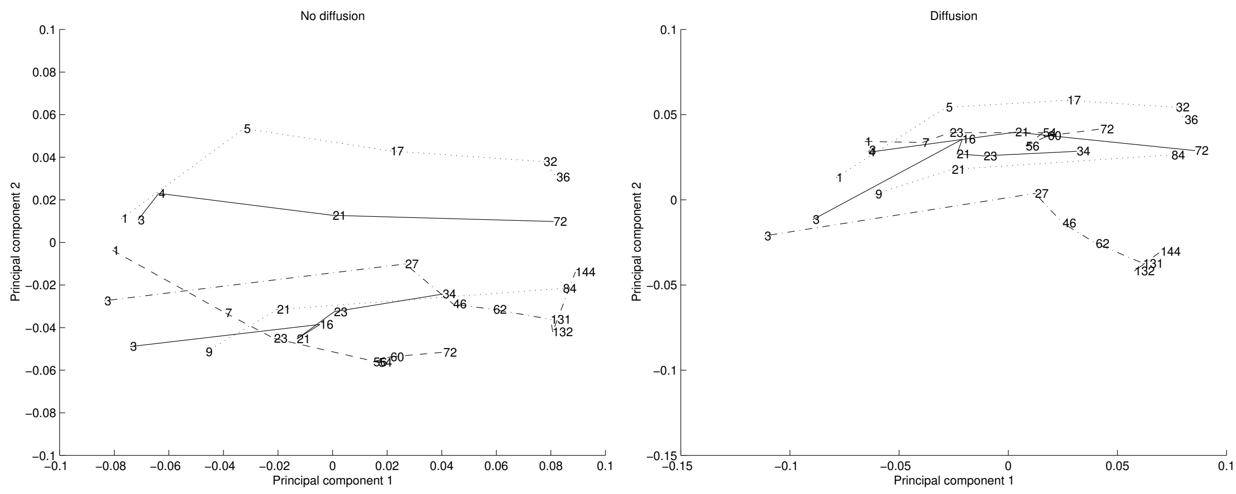

Figure 7.10: *Scatterplots of the first and second principal component for the six cases before (left) and after (right) the geometric-constrained diffusion is applied. For visual clarity, each patient's mean is kept. Numbers are age in month. It is clear that the six cases span an angular range of nearly 90 degrees in this projection (left image - upper dotted line versus dashed line, first pair of age intervals); after diffusion, the alignment is far tighter.*

From this display (Figure 7.10-right image), it appears that the three to seven forms of each case lie reasonably close to a line in Procrustes space. We can thus summarize each by its first principal component [Roh93], and then examine the resulting six vectors to see how they may be ordinated. Figure 7.11 indicates the distribution of these six vectors in the six-dimensional subspace they span. Each principal component is normalized for its actual Procrustes variance explained, and the presentation here preserves that metric. We see a strong central tendency in these six growth vectors, closest to the observed trend for patient 3 or patient 4. The variation around this mean trajectory looks spherical.

A cross validation study is performed in order to evaluate the quality of the growth model.

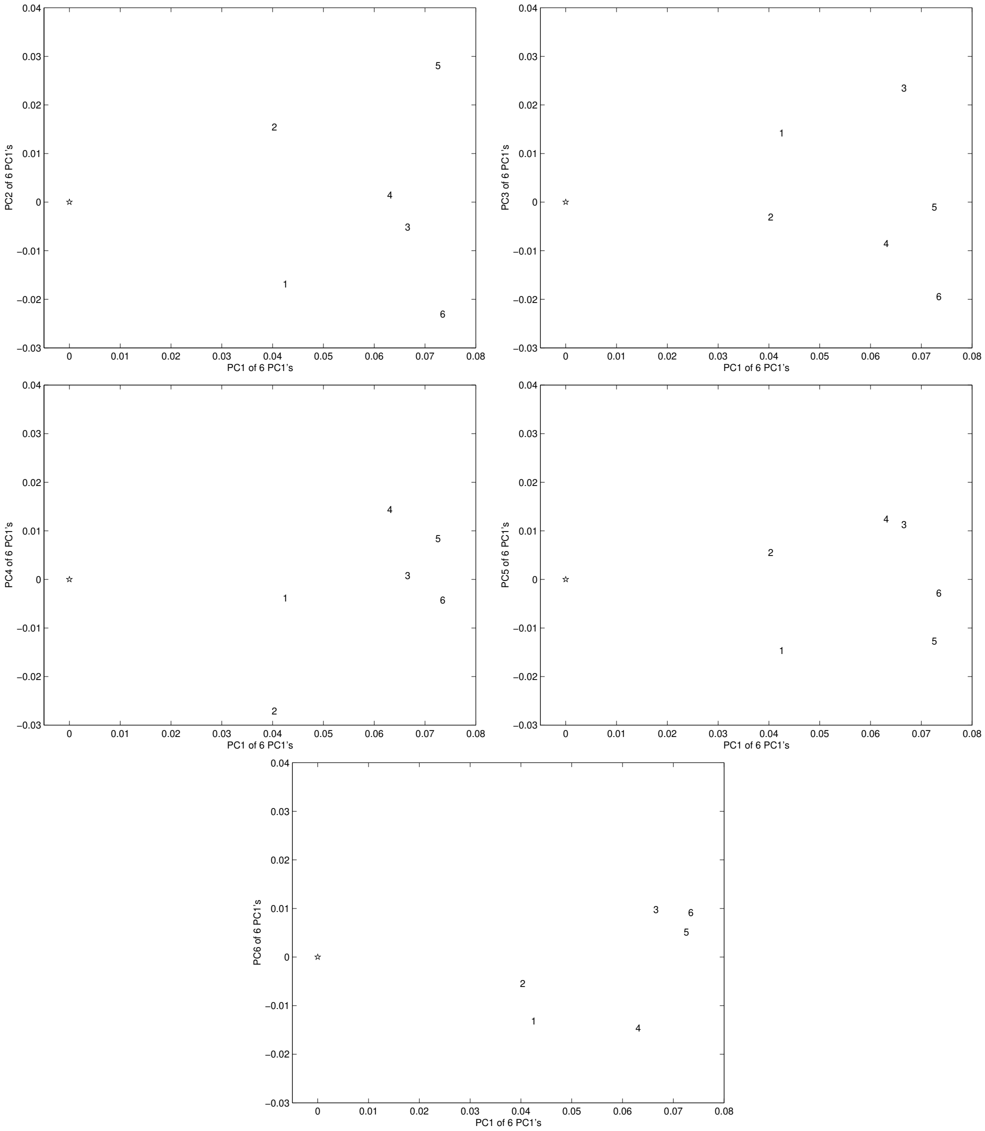

Figure 7.11: *The distribution of the six vectors (first principal component for each patient) in the six-dimensional subspace they span. Each principal component is normalized for its actual Procrustes variance explained, and the presentation here preserves that metric. We see a strong central tendency in these six growth vectors, closest to the observed trend for patient 3 or patient 4. The variation around this mean trajectory looks spherical.*

7.7.1 Cross validation

We demonstrate the power of this procedure by a series of growth predictions that, in all cases, predict the oldest form for each of the six patients by altering each of the earlier forms for that patient according to the regression on Centroid Size and the first principal component given by the *other* five patients.

The model is built as described above except that one patient at a time, $m \in \{1, \ldots, 6\}$, is excluded *totally* from the analysis. Eigenvector $\mathbf{e}_{1,m}$ is found by the PCA. Subscript 1 and m means the first eigenvector where patient m is excluded from the generation of the model. Patient m's scans are then aligned with the grand mean shape (calculated from the scans in the model). Notice, normally the mean shape for given a patient which you wish to model is not known. However, subtracting a constant shape, like the patient's mean shape, is just a pure translation in the Procrustes space, and one scan gives a fix-point in Procrustes space. Hence, we do not have to worry about the patient's mean shape.

A new shape is modeled by

$$\mathbf{x}_{future} = \mathbf{x}_i + t \cdot \mathbf{e}_{1,m} \, , \, t \in \mathcal{R} \tag{7.8}$$

where t is the "time" parameter and $\mathbf{x}_i$ is the initial mandible. For *evaluation*, t is found by minimizing the Euclidian norm

$$\hat{t} = \arg\min_t \|\mathbf{x}_j - (\mathbf{x}_i + t\mathbf{e}_{1,m})\|_2 \tag{7.9}$$

where $\mathbf{x}_j$ is the shape to be approximated.

For *prediction*, extra information is needed in order to estimate t. The high correlation between age, centroid size, or mandibular length and the first principal component (PC1) (see Figure 7.12-7.14) shows that it is possible to estimate t from one of the three variables. Here, we only use centroid

Patient excluded	Percentage Variance explained in model ($= 100\% * \lambda_1/(\sum_i \lambda_i)$)	α
none	62.2	0
1	64.5	4.1
2	65.8	5.8
3	62.1	6.5
4	62.3	8.3
5	60.8	5.9
6	61.1	3.9

Table 7.3: *This table shows the stability of the generated growth models in the cross validation study. The second column (Percentage Variance explained) is very constant (mean=62.69, standard deviation=1.82). α is the angle in degrees between the first eigenvectors in the full model, $\mathbf{e}_1$, and the reduced model where one patient is excluded, $\mathbf{e}_{1,m}$. The two columns (column two and three) shows that none of the patients individually "controls" the variability of the data. It is a bit surprising as the last three scans of patient 4 is much older than any of the other scans (cf. Table 7.1), but it shows the stability of the model. Our analysis have shown that especially the "trick" of Equation 7.3 enhances the stability of the PCA analysis.*

size, CS (Figure 7.13). The slope, α in the model

$$PC1 = \alpha \cdot CS + \beta \tag{7.10}$$

is estimated using linear regression (note, α is found for the reduced model). Then

$$t = (CS_{future} - CS_i) \cdot \alpha \tag{7.11}$$

thus, we have the model

$$\mathbf{x}_{future} = \mathbf{x}_i + (CS_{future} - CS_i) \cdot \alpha \cdot \mathbf{e}_{1,m} \tag{7.12}$$

Patient		Predicted shapes		Optimal shapes	
number	scan	mean	std	mean	std
1	1	2.4196	1.2681	2.3972	1.2827
	2	1.8005	0.7700	1.6775	0.6694
	3	1.7475	0.7186	1.6879	0.7347
	4	1.3569	0.5837	1.3320	0.5512
2	1	3.4783	1.4310	2.8138	1.2819
	2	2.3849	1.1488	2.2581	1.2569
	3	2.2891	1.2738	2.2891	1.2697
	4	1.5070	0.7303	1.4869	0.7241
	5	1.6217	0.7708	1.5092	0.7353
	6	1.3683	0.6278	1.3610	0.6244
3	1	2.7568	1.2746	2.6646	1.2016
	2	2.4617	1.1608	2.3899	1.1456
	3	2.0740	0.9360	2.0734	0.9322
	4	0.9720	0.4141	0.8287	0.4404
4	1	3.6691	1.5971	3.6217	1.6345
	2	3.1307	1.5646	2.8192	1.4632
	3	2.7982	1.4229	2.7007	1.3033
	4	2.8315	1.3991	2.7633	1.2584
	5	2.0300	0.9833	2.0049	1.0257
	6	2.0289	0.9239	1.9238	0.9318
5	1	2.6153	1.0301	2.6152	1.0326
	2	3.0812	1.2174	3.0721	1.2107
	3	2.1441	1.0378	2.0707	1.0054
6	1	2.8292	1.0440	2.5427	0.9922
	2	2.8013	1.2309	2.6239	1.0537

Table 7.4: *Table shows the mean (*"mean"*) and standard deviation (*"std"*) for the prediction errors. Prediction error is calculated as the Euclidian distance between the same semi-landmark in the observed and predicted mandible.* "Predicted shapes" *is the shapes calculated from Equation 7.12. For* "Optimal shapes", t *is calculated using Equation 7.9. The difference between the two shape models show how much the regression model (Equation 7.10) influences the prediction. It is seen that the additional error from the regression model is small.*

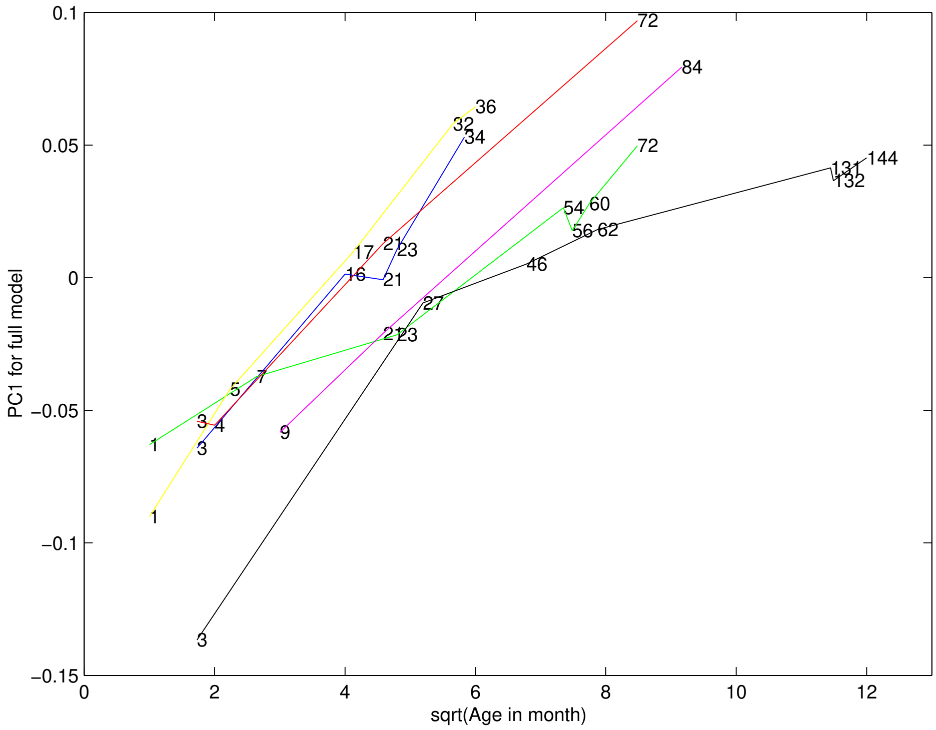

Figure 7.12: *The plot shows* $\sqrt{age}$ *versus the principal component for the full model (all patients are used to construct the model). It is seen that there is a clear relation between shape and age. The colors refer to the individual patients. The numbers on the lines are ages. The correlation coefficient equals 0.80 (for all mandibles). See Section 7.7.1 for further discussion.*

It is seen that only one scan of the patient and the future centroid size is needed to make the prediction.

The explained variance in the model and the angle between $\mathbf{e}_1$ (full model) and $\mathbf{e}_{1.m}$ (reduced model) is almost constant as seen in Table 7.3. This indicates that the model in not controlled by a single patient which could have been the case for patient 4, since the three latest scans all belong to patient 4.

The last scan for each patient is predicted by altering each of the earlier scans for that patient. The results are shown in Table 7.4. A subset of the predicted mandibles are shown in Figures 7.16-

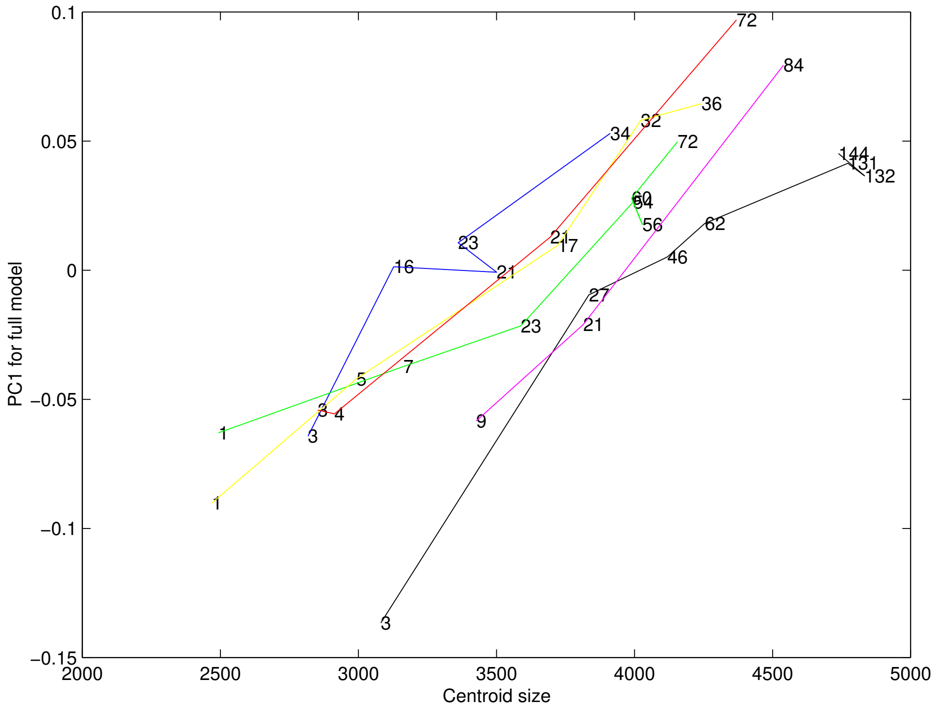

Figure 7.13: *The plot shows centroid size (before rescaling - see Section 7.6) versus the principal component for the full model. It is seen that there is a clear relation between shape and size. The colors refer to the individual patients. The numbers on the lines are ages. The correlation coefficient equals 0.83 (for all mandibles). See Section 7.7.1 for further discussion.*

7.21. The histograms of the errors for the figures are shown in Figure 7.22. The left images in Figures 7.16-7.21 represent the last observed scan for each patient. The right images show the modeled mandibles. The rainbow color coding (from blue to red) shows the errors. The colors are "linear" from blue (0 mm) over green (5 mm) to red (10 mm). The error is calculated as the Euclidian distance between the two same semi-landmarks in the observed and modeled scan. The modeled shape is resized to match the size of the observed scan.

When segmenting the scans at 1-3 month of age, large cavities are erroneously introduced because of the very low x-ray absorption (Figure 7.15). As seen from Figure 7.18, these errors are not removed by the growth model, as expected. For that reason, the largest errors (> 7 mm) are seen

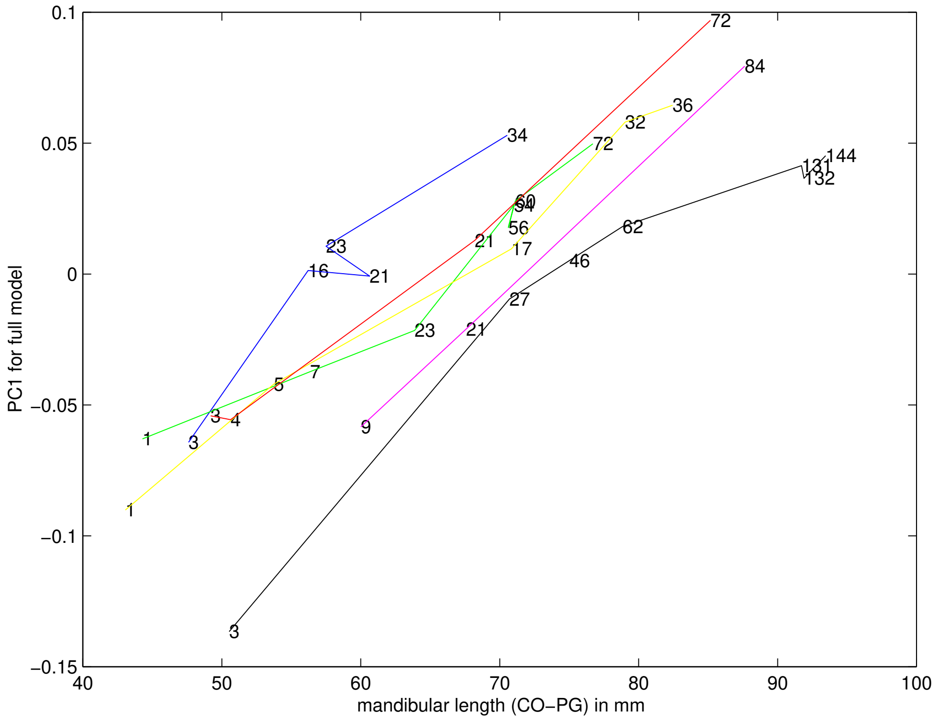

Figure 7.14: *The plot shows the length of the mandible (calculated as the length between the midpoint of the most posterior superior point on the condylar heads and gnathion as done in [RMJH74]-Variable 79) versus the principal component for the full model. It is seen that there is a clear relation between shape and the length. The colors refer to the individual patients. The numbers on the lines are ages. The correlation coefficient equals 0.85 (for all mandibles). See Section 7.7.1 for further discussion.*

at the cavities. Also, removal of a tooth is obviously not modeled, as seen in Figure 7.19. Besides these very specific errors, we do not see errors larger than approximately 5 mm, except for patient 4, scan #7 (Figure 7.19). This patient has a very prominent chin compared to the model, which is not seen on the other patients.

The ability to model patient 4, scan #7 accurately is a bit surprising. None, of the other patients have been scanned at that age, the oldest scan (when patient 4 is excluded) being 7 years old (patient 6, scan #3), but patient 4, scan #7 is 12 years old. This also indicates that the growth is

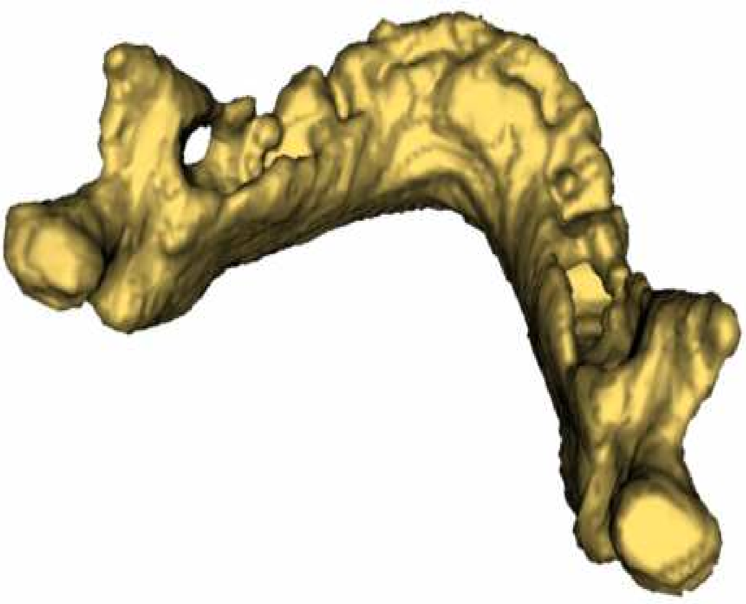

Figure 7.15: *The raw dataset of patient 3, scan #1 (1 month scanning). The mandibular bone and teeth have low density, therefore cavities and holes are introduced when segmented.*

modeled correct.

From a clinical point of view, it may not be that important to simulate the growth from a 3 month old child to 12 years old, but the exercise shows the strength of the growth model. Figures 7.23-7.24 are included to show how the errors decrease as successively older scans are used. Notice, how small the errors are when patient 4, scan #6 (11 years old) is used as the basis for the model. 12715 of the 14851 semi-landmarks (85.6%) have an error less than 3 mm. Figure 7.25 shows the histograms.

7.8 Conclusion

In the present paper, a linear 3D growth model has been developed by means of Procrustes analysis and principal component analysis. The model is capable of predicting the temporal shape change, as seen on the mandible, accurately. The shape *change*, predicted by the model, is independent of the actual patient (seen by subtracting $\mathbf{x}_i$ from Equation 7.12).

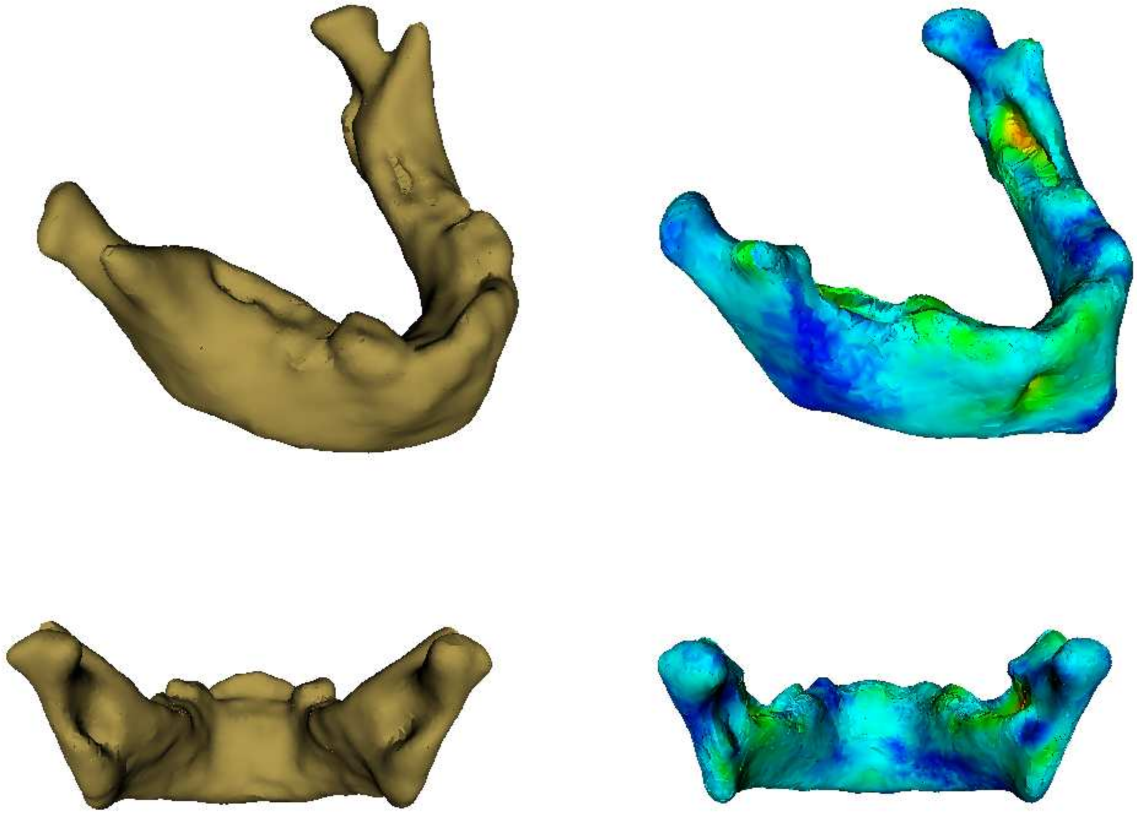

Figure 7.16: *Modeled last scan (scan #5) based on the first scan (scan #1) for patient 1. The large errors are located at the cavities as described in the text. The left images being the observed scan seen from two different viewpoints. The right images are the modeled mandible seen from the same two viewpoints. The surface is rainbow color coded from blue (0 mm) to red (10 mm) with the error, calculated as the Euclidian distance between the same semi-landmarks in the observed and modeled scan. The mean error is 2.4 mm.*

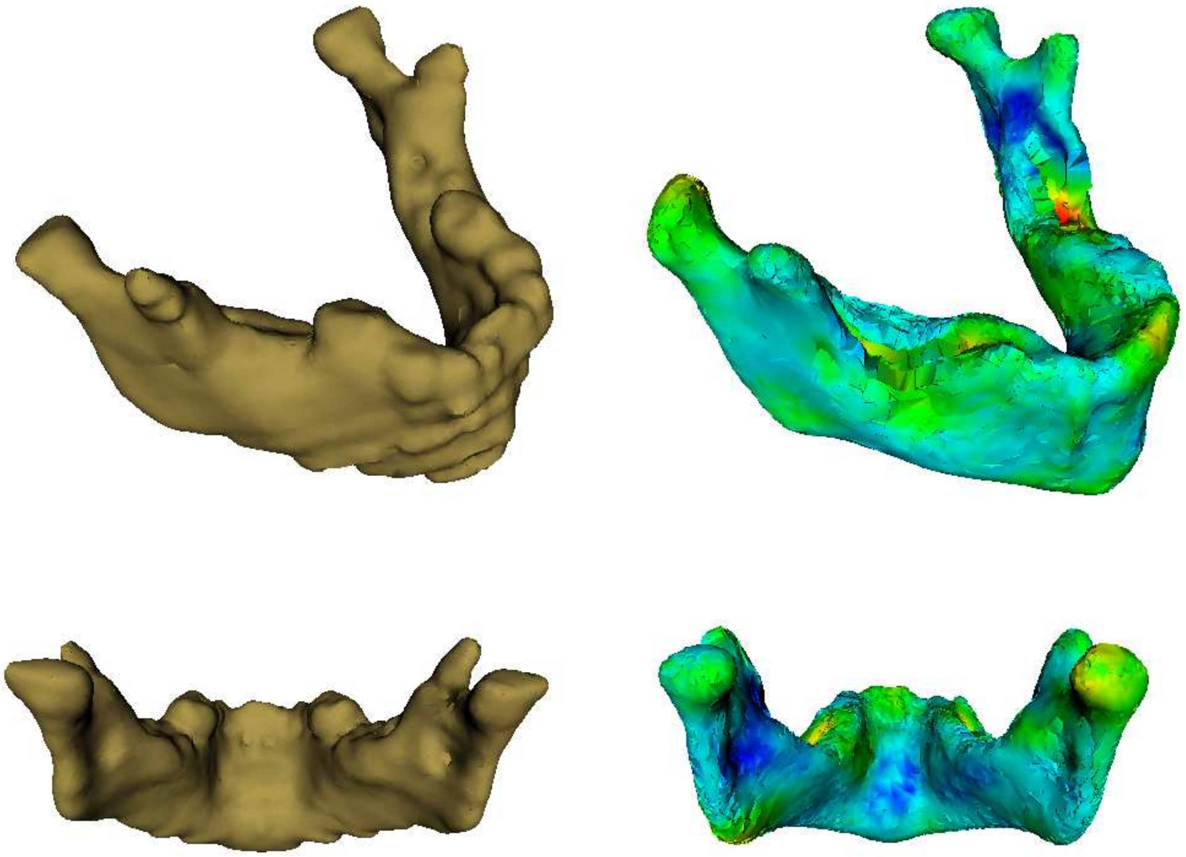

Figure 7.17: *Modeled last scan (scan #7) based on the first scan (scan #1) for patient 2. The large errors are located at the cavities introduced by the segmentation of the 1 month old scan. The mean error is 3.5 mm. The staircases on the observed scan #7 is due to errors in the original volume.*

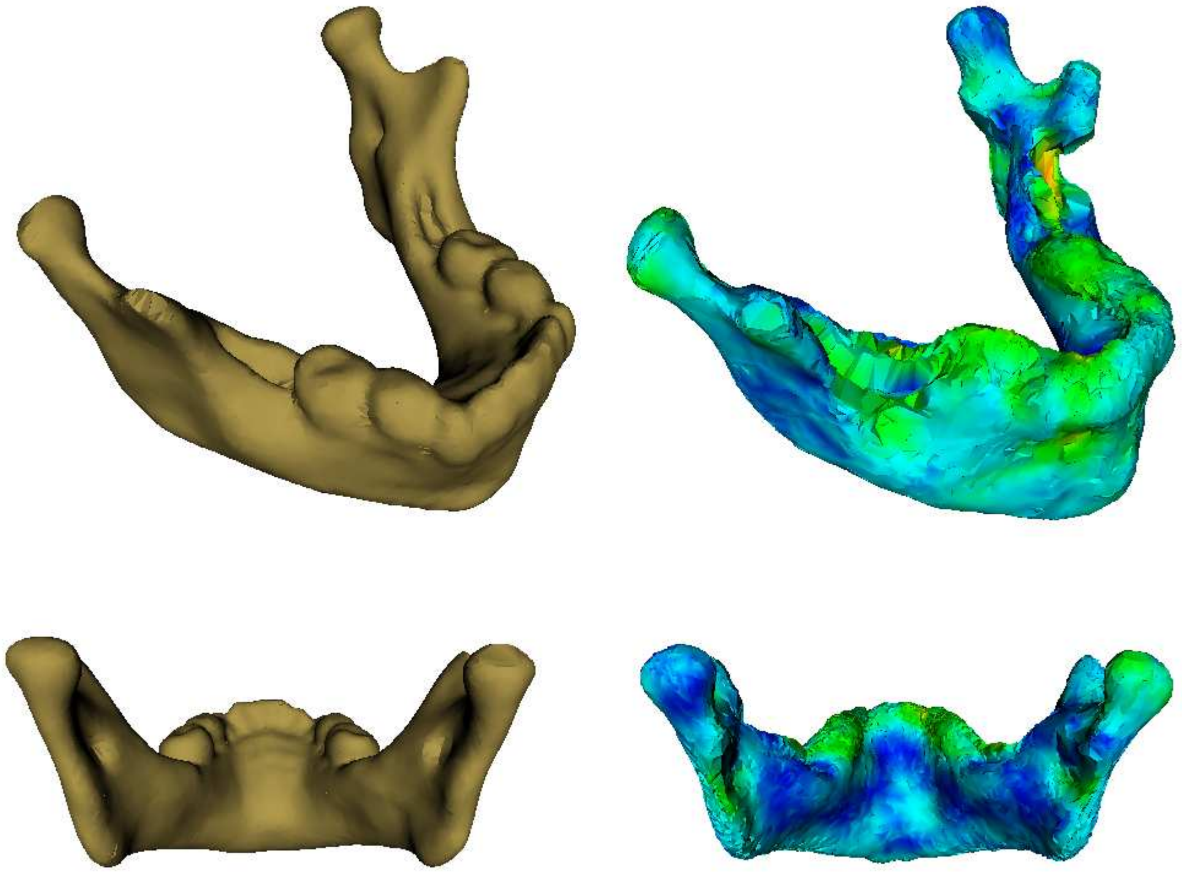

Figure 7.18: *Modeled last scan (scan #5) based on the first scan (scan #1) for patient 3. The mean error is 2.8 mm. By looking at the first scan (Figure 7.15) it is not surprising to find the large errors at the cavities. The notch in the side of the modeled mandible is related to the hole found at the same place on the first scan.*

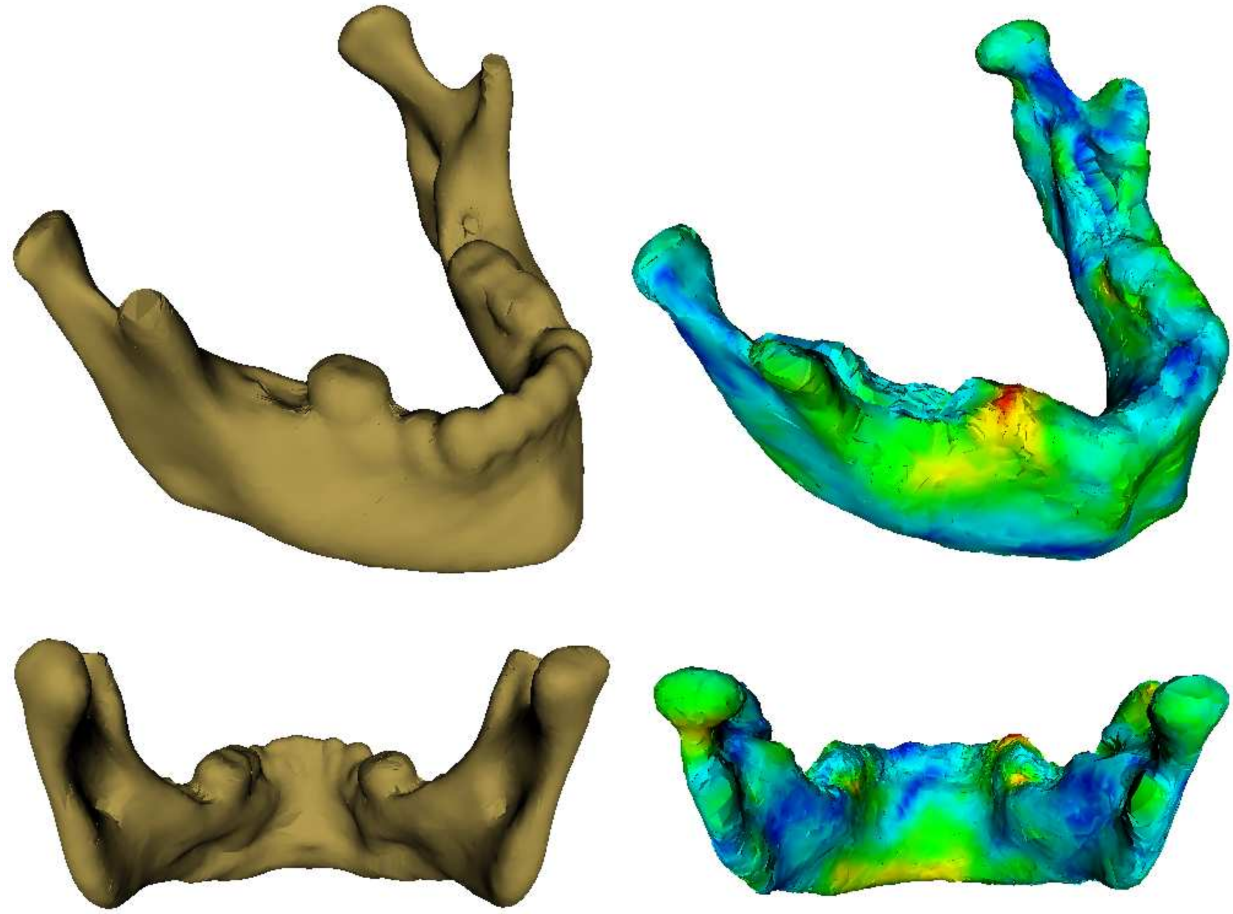

Figure 7.19: *Modeled last scan (scan #7) based on the first scan (scan #1) for patient 4. The mean error is 3.7 mm. The quality of the model is surprising. Non of the scans in the model is as old as scan #7 (12 years old). The oldest scan in the model is 7 years old (patient 6, scan #3). This indicates the stability of the growth. The red area shows a missing tooth, which has been extracted. The prominent chin is not modeled very well. Using older scans solves the problem (Figures 7.23 & 7.24).*

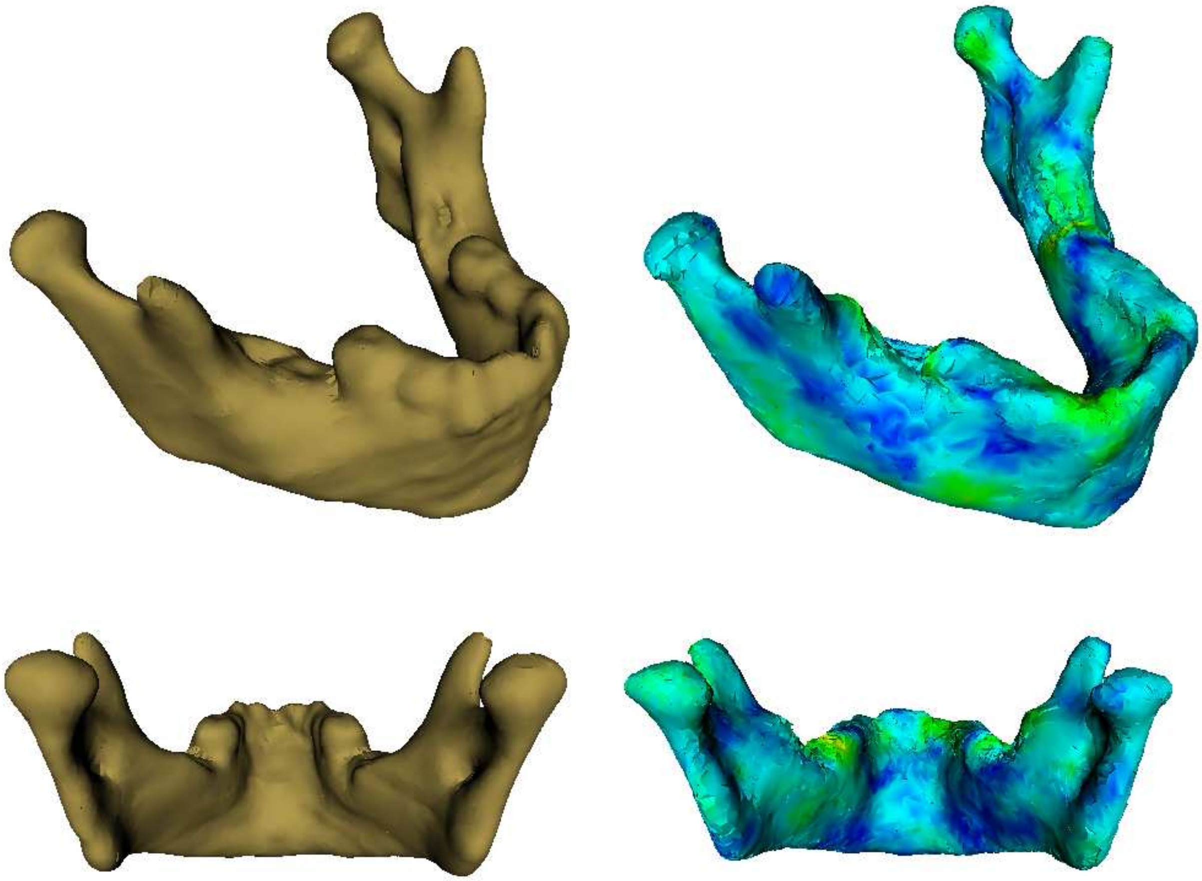

Figure 7.20: *Modeled last scan (scan #4) based on the first scan (scan #1) for patient 5. The mean error is 2.6 mm. An almost totally blue surface shows the high accuracy of the model.*

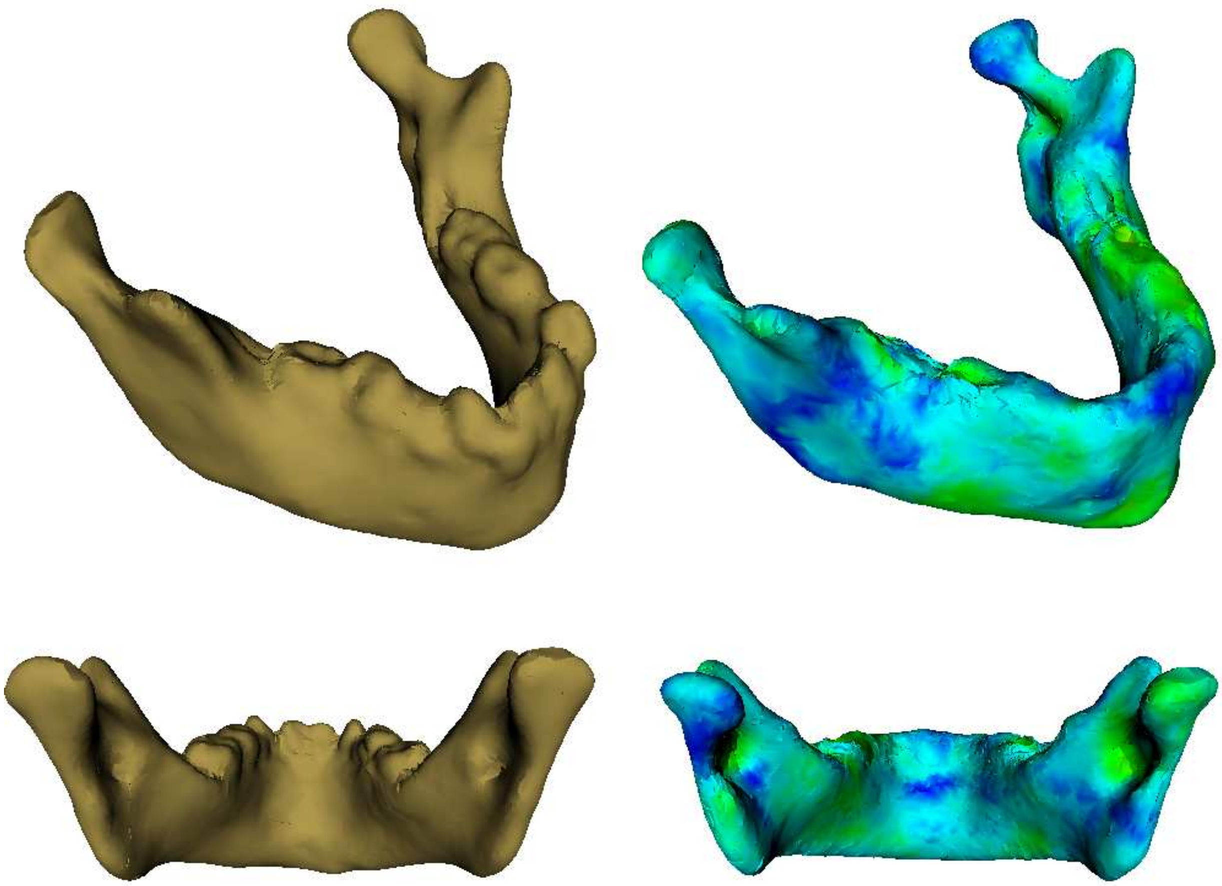

Figure 7.21: *Modeled last scan (scan #3) based on the first scan (scan #1) for patient 6. The mean error is 2.8 mm. The model is very accurate, only a slight twist of the condyles are seen.*

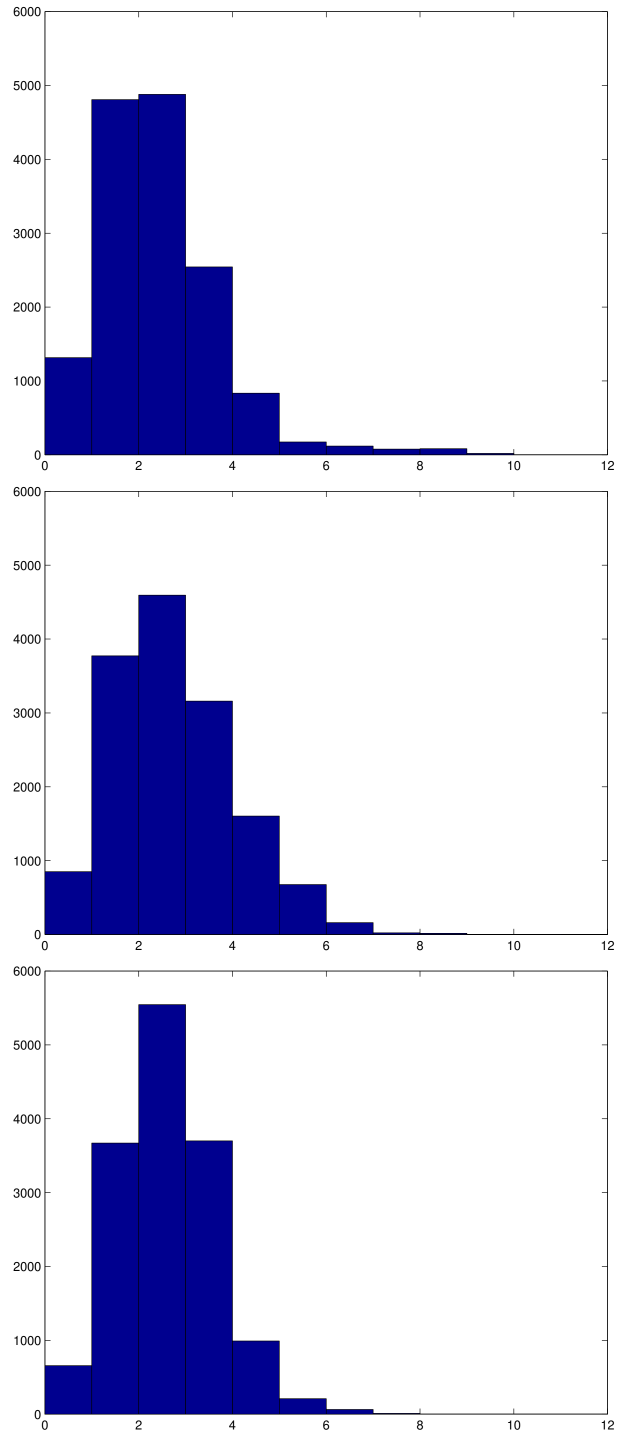

Figure 7.22: *Histogram of the prediction errors (Euclidian distance between the two same semi-landmarks in the observed and modeled scan) for the six predicted mandibles shown in Figures 7.16-7.21 (starting top left and ending bottom right). The larger error is mainly due to cavities coming from the segmentation of the very young scans (1-3 month) as seen in Figure 7.15. See Table 7.4 for mean and standard deviation. See also text for more details.*

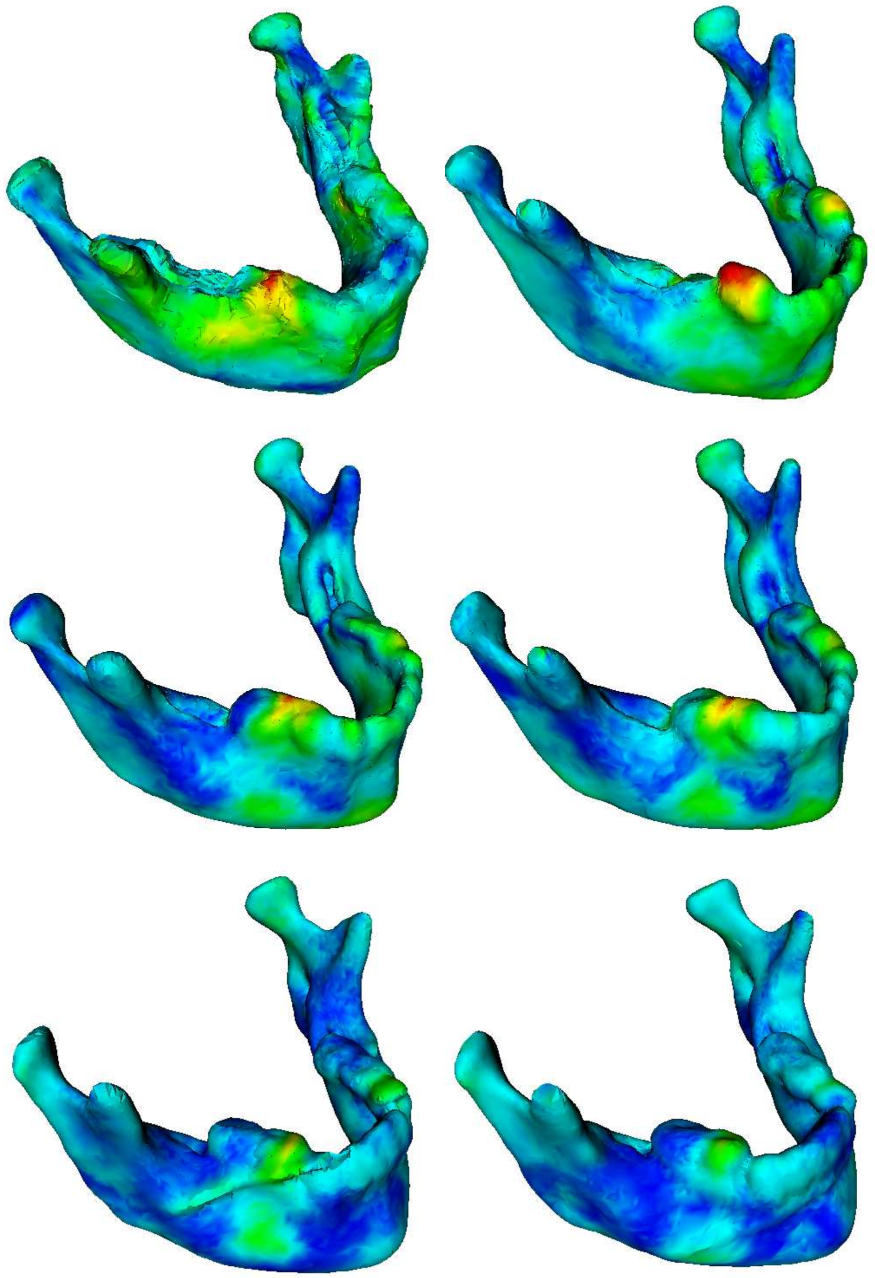

Figure 7.23: *This figure and the next (Figure 7.24) show the predicted shape of the most recent scan of patient 4 (scan #7) using successively more recent scans of the child. Starting at top left and ending at bottom right, scan #1 to #6 are used as the basis mandible for the model. It is seen that we do not have the same problems with the cavities when using scans older than the first. As expected, the modeled shapes becomes better and better as the basis mandible is increased in age. This is also reflected in the histograms seen in Figure 7.25. Notice, the model itself - the first eigenvector in Equation 7.12 - stays the same.*

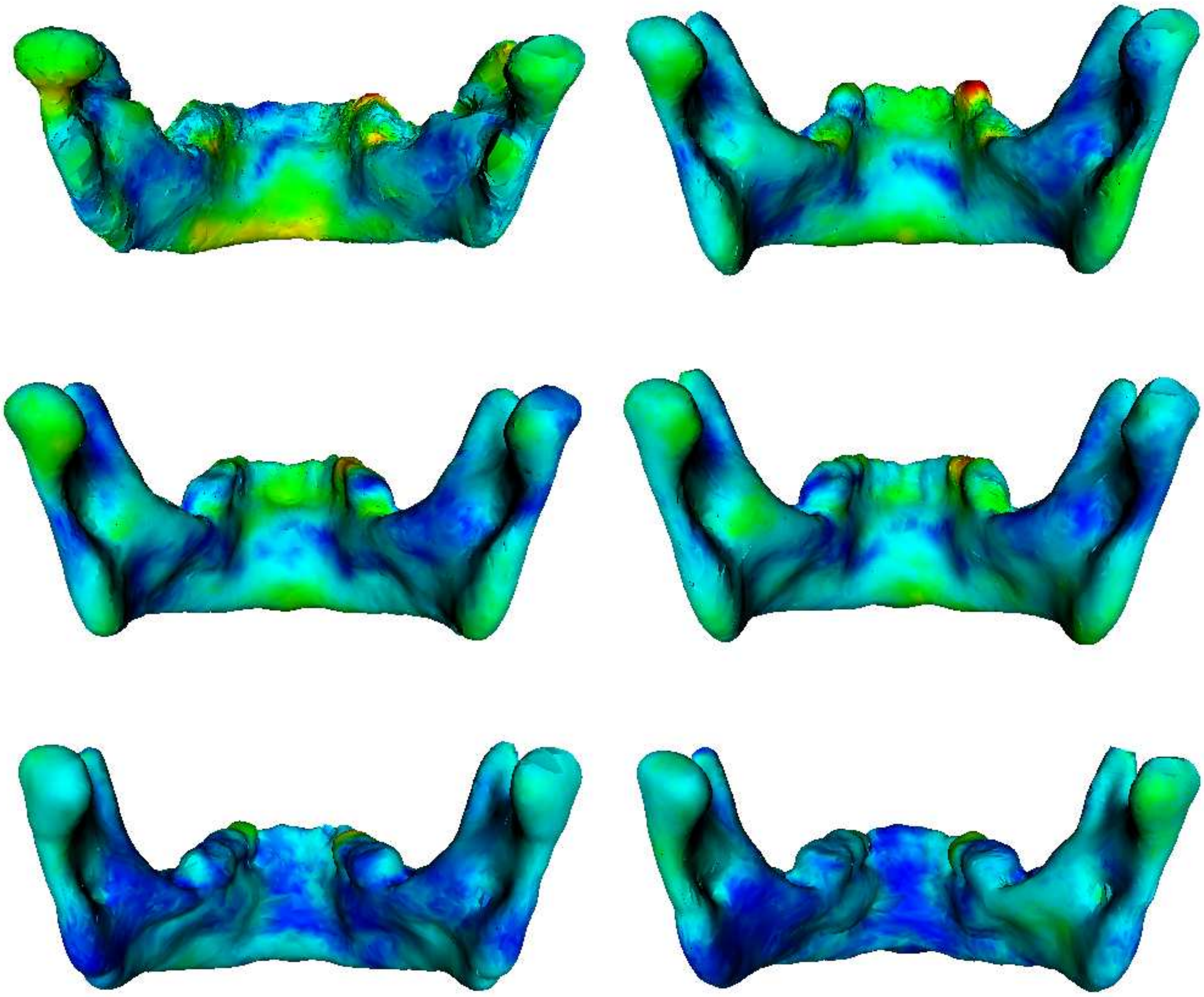

Figure 7.24: *The same mandibles as in Figure 7.23 but seen from a different viewpoint. See caption in Figure 7.23 for explanation.*

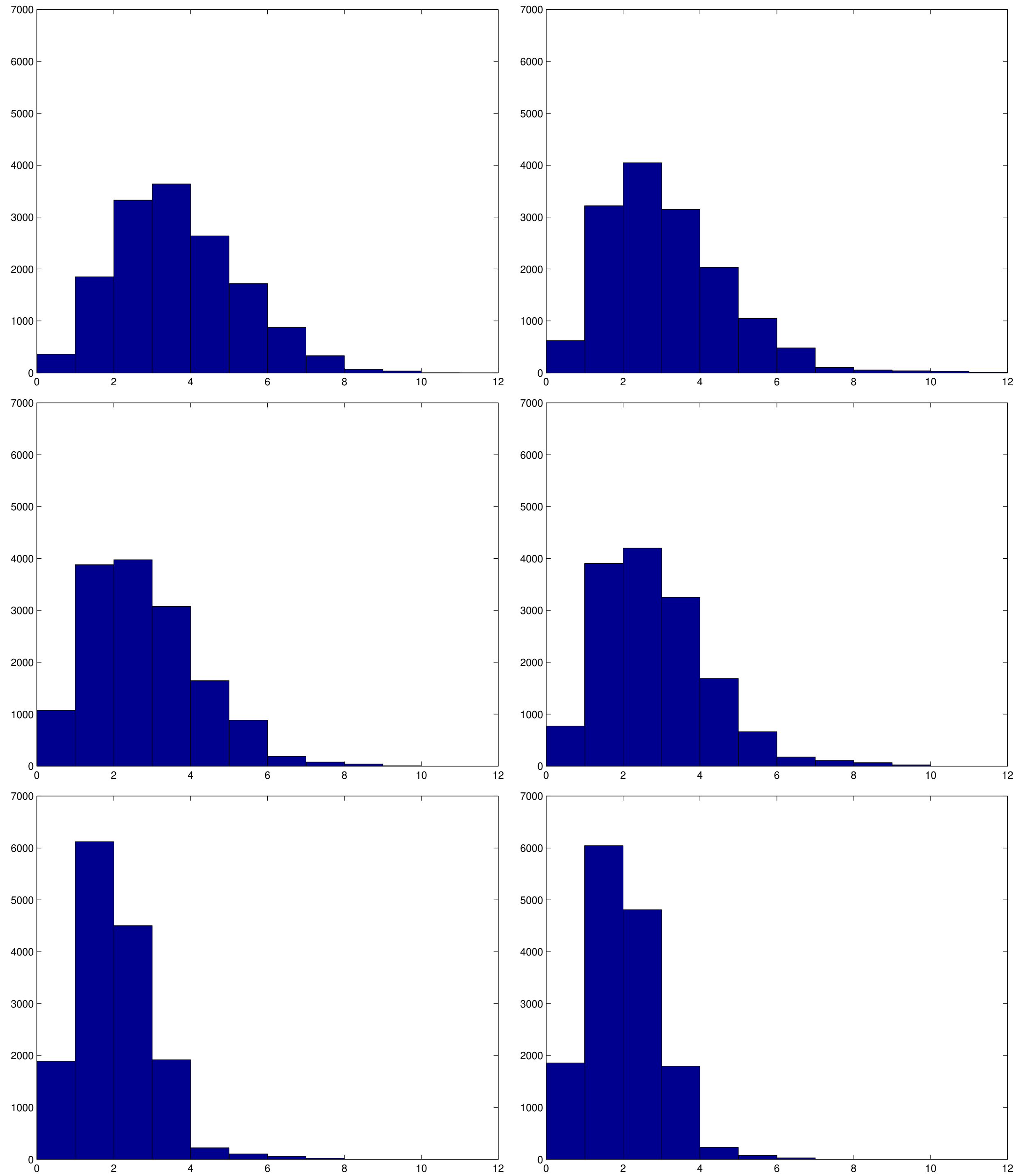

Figure 7.25: *The histograms of the prediction errors seen in Figures 7.23 & 7.24. The histograms are ordered the same way as the predicted shapes. It is evident from the histograms that the errors decrease by increasing the age of the mandible used for the prediction. See Table 7.4 for mean and standard deviation. See also caption in Figure 7.23 for further explanation.*

The huge increase of the percentage of the total variation in the first eigenvalue by applying the *geometry constrained diffusion* (Table 7.2) is surprising and should be investigated further. Also inclusion of 0D and 1D constrains would be interesting.

Other studies, like [BS83], show that the growth of the mandible is non-linear, when using a "biological coordinate system". The present study does not reject that hypothesis, but indicates that the growth is linear if modeled in Procrustes space. This also complies very well with the result of [DHBS99]. A combination of the two "frames" might be very fruitful. Procrustes space could be used for the growth modeling and the "biological space" for the visualization. Among other, this would allow for extraction of biological knowledge and simulation of the development in the craniofacial complex.

Figures 7.23-7.25 show the accurate model of the 12 years old mandible, based on a growth model where non of the patients were older than 7 years (Table 7.1). The ability to extrapolate the growth period by 5 years strengthens our hypothesis about linear growth.

The strong correlation between the shape feature (PC1) and age (Figure 7.12) or length of the mandible (Figure 7.14) indicate that it should be possible to make an accurate prediction of the mandible (size and shape) based on one scanning of the patient and a future age or length (of the mandible).

At present, we can only obtain the closely spaces CT scans that allow this kind of analysis from clinical cases with various types of craniofacial growth disturbances. As mentioned above, in Apert syndrome the mandible is not affected by the primary anomaly [KAC99]. Other craniofacial syndromes also show fairly normal mandibular development e.g. Crouzon syndrome and achondroplasia. It will be interesting, if these groups come up with the same mean growth trajectories.

7.9 Acknowledgments

Preparation of the contribution was supported by the Danish Technical Research Council, registration number 9600452 to Per Rønsholt Andresen and the John and Birthe Meyer Foundation. Thanks to Tron Darvann, 3D-Lab, Denmark, for bringing the data to Denmark. The authors are also grateful for the discussions with Mads Nielsen, IT-University, Denmark.

The Visualization Toolkit (http://www.kitware.com) was used for the 3D visualizations. Rendering was done by the Blue Moon Rendering Tools program *rendrib* (http://www.bmrt.org).

Bibliography

[AN99] P. R. Andresen and M. Nielsen. Non-rigid registration by geometry-constrained diffusion. In *Medical Image Computing and Computer-Assisted Intervention - MICCAI'99*, volume 1679 of *Lecture Notes in Computer Science*, pages 533–543, 1999.

[ANK98] P. R. Andresen, M. Nielsen, and S. Kreiborg. 4D shape-preserving modelling of bone growth. In *Medical Image Computing and Computer-Assisted Intervention - MICCAI'98*, volume 1496 of *Lecture Notes in Computer Science*, pages 710–719, 1998.

[BGK95] C. Brecbühler, G. Gerig, and O. Kübler. Parametrization of closed surfaces for 3-D shape description. *Computer vision, Graphics and Image Procession*, 61:154–170, 1995.

[BM92] P. J. Besl and N. D. McKay. A method for registration of 3-D shapes. *IEEE Transactions on Pattern Analysis and Machine Intelligence*, 14(2):239 – 255, 1992.

[BNGK97] M. Bro-Nielsen, C. Gramkow, and S. Kreiborg. Non-rigid image registration using bone growth model. In *CVRMed-MRCAS'97*, Lecture Notes in Computer Science, pages 3–12. Springer, 1997.

[Boo91] F. L. Bookstein. *Morphometric Tools for Landmark Data : Geometry and Biology.* Cambridge University Press, 1991.

[Boo96] F. L. Bookstein. Landmark methods for forms without landmarks: localizing group differences in outline shape. In *Proceedings of the IEEE Workshop on Mathematical Methods in Biomedical Image Analysis*, pages 279–289, 1996.

[Boo97] F. L. Bookstein. Shape and the information in medical images: a decade of the morphometric synthesis. *Computer Vision and Image Understanding*, 66(2):97–118, 1997.

[BS83] A. Björk and V. Skieller. Normal and abnormal growth of the mandible. A synthesis of longitudinal cephalometric implant studies over a period of 25 years. *European Journal of Orthodontics*, 5:1–46, 1983.

[CT99] T. F. Cootes and C. J. Taylor. Statistical models of appearance for computer vision. Electronic version: http://www.wiau.man.ac.uk/∼bim, 1999.

[dC76] M. P. do Carmo. *Differential Geometry of Curves and Surfaces.* Prentice-Hall, 1976.

[DHBS99] D. Dean, M. G. Hans, F. L. Bookstein, and K. Subramanyan. Three dimensional Bolton-Brush growth study landmark data: Ontogeny and sexual dimorphism of the bolton standards cohort. *Cleft Palate - Craniofacial Journal*, 1999. in press.

[FA96] J. Feldmar and N. Ayache. Rigid, affine and locally affine registration of free-form surfaces. *International Journal of Computer Vision*, 18(2):99–119, 1996.

[FL98] M. Fleute and S. Lavallée. Building a complete surface model from sparse data using statistical shape models: application to computer assisted knee surgery. In *Medical Image Computing and Computer-Assisted Intervention - MICCAI'98*, pages 879–887, 1998.

[GM98] U. Grenander and M. I. Miller. Computational anatomy: an emerging discipline. Technical report, Center for Image Science (CIS), 1998. Electronic version: http://cis.jhu.edu/wu_publications.

[Goo91] C. Goodall. Procrustes methods in the statistical analysis of shape. *Journal of the Royal Statistical Society B*, 53(2):285–339, 1991.

[Joh63] R. M. Johnson. On the theorem stated by Eckart and Young. *Psychometrika*, 28:259–263, 1963.

[Jos97] S. Joshi. *Large Deformation Diffeomorphisms and Gaussian Random Fields for Statistical Characterization of Brain Sub-Manifolds.* PhD thesis, Washington University, 1997.

[JZDJ98] A. K. Jain, Y. Zhong, and M.-P. Dubuisson-Jolly. Deformable template models: a review. *Signal Processing*, 71:109–129, 1998.

[KAC99] S. Kreiborg, H. Aduss, and M. M. Cohen Jr. Cephalometric study of the Apert syndrome in adolescence and adulthood. *Journal of Craniofacial Genetics Developmental Biology*, 19:1–11, 1999.

[Koe84] J. J. Koenderink. The structure of images. *Biological Cybernetics*, 50:363–370, 1984.

[KSG98] A. Kelemen, G. Székely, and G. Gerig. Three-dimensional model-based segmentation of brain MRI. In *Proc. Biomedical Image Analysis*, pages 4–13, 1998.

[LA99] H. Lester and S. R. Arridge. A survey of hierarchical non-linear medical image registration. *Pattern Recognition*, 32:129–149, 1999.

[MCL+96] L. F. Marcus, M. Corti, A. Loy, G. J. P. Naylor, and D. E. Slice, editors. *Advances in Morphometrics*, NATO Asi Series. Series A, Life Sciences, Vol 284. Plenum Press, 1996.

[MT96] T. McInerney and D. Terzopoulos. Deformable models in medical image analysis: a survey. *Medical Image Analysis*, 1(2):91–108, 1996.

[MV98] J. B. A. Maintz and M. A. Viergever. A survey of medical image registration. *Medical Image Analysis*, 2(1):1–36, 1998.

[NA98] M. Nielsen and P. R. Andresen. Feature displacement interpolation. In *IEEE 1998 International Conference on Image Processing (ICIP'98)*, pages 208–212, 1998.

[RMJH74] M. L. Riolo, R. E. Moyers, J. A. McNamara Jr., and W. S. Hunter. *An atlas of craniofacial growth*. Center for Human Growth and Development, The University of Michigan, 1974.

[Roh93] F. J. Rohlf. Relative warp analysis and an example of its application to mosquito wings. In L. Marcus et al., editor, *Contributions to Morphometrics*, pages 131–159, 1993.

[Roh98] K. Rohr. Image registration based on thin-plate splines and local estimation of anisotropic landmark uncertainties. In W. M. Wells, A. Colchester, and S. Delp, editors, *Medical Image Computing and Computer-Assisted Intervention - MICCAI'98*, volume 1496 of *Lecture Notes in Computer Science*, pages 1174–1183, 1998.

[SD96] L. H. Staib and J. S. Duncan. Model-based deformable surface finding for medical images. *IEEE Transactions on Medical Imaging*, 15(5):720–731, 1996.

[SL96] R. Szeliski and S. Lavallée. Matching 3-D anatomical surfaces with non-rigid deformations using octree-splines. *International Journal of Computer Vision*, 18(2):171–186, 1996.

[STA98] G. Subsol, J.-P. Thirion, and N. Ayache. A general scheme for automatically building 3D morphometric anatomical atlases: application to a skull atlas. *Medical Image Analysis*, 2(1):37–60, 1998.

[Sub95] G. Subsol. *Construction automatique d'atlas anatomiques morphométriques à partir d'images médicales tridimensionnelles.* PhD thesis, École Centrale Paris, 1995.

[Thi96] J.-P. Thirion. The extremal mesh and the understanding of 3D surfaces. *International Journal of Computer Vision*, 19(2):115–128, 1996.

[Zha94] Z. Zhang. Iterative point matching for registration of free-form curves and surfaces. *International Journal of Computer Vision*, 13(2):147–176, 1994.